TESI DI DOTTORATO

UNIVERSITA' DEGLI STUDI DI NAPOLI "FEDERICO II"

DIPARTIMENTO DI INGEGNERIA ELETTRONICA
E DELLE TELECOMUNICAZIONI

DOTTORATO DI RICERCA IN
INGEGNERIA ELETTRONICA E DELLE TELECOMUNICAZIONI

Advanced Differential Interferometric SAR techniques

ANTONIO PEPE

Il Coordinatore del Corso di Dottorato
Ch.mo Prof. Giovanni Poggi

Il Tutore
Ch.mo Prof. Ovidio M. Bucci

Anno accademico 2005–2006

To the people of my life

Index

Introduction

The Advanced SAR interferometry techniques and their matter of fact applications will be addressed in this work. Synthetic Aperture Radar (SAR) is a coherent active microwave remote sensing system, able to perform accurate distance measurements between the sensor platform and the target on the ground. Within the SAR technology an important improvement has been gained with the introduction of the interferometric SAR (InSAR) technique. It is based, in its basic form, on the exploitation of two different SAR images to extract the corresponding phase difference, which is related to the topography of the illuminated scene.

A further improvement has been realized when the differential SAR interferometry (D-InSAR) has been introduced. D-InSAR methodology provides to simulate the topography phase screen and to isolate the contribution due to the deformation of the scene occurred between the two flight of the radar sensor.

The advancing on the D-InSAR technology, with a particular emphasis on the phase unwrapping (PhU) problems, will be the key point of this work, which is organized as follows:

- Chapter I - After a brief introduction concerning the basic principles of the SAR image formation, the InSAR technologies for the estimation of the scene topography will be presented. Finally, the Differential InSAR technique and its main limitations are analyzed.
- Chapter II – The topic of this chapter will concern the extension of the D-InSAR methodology to analyze the temporal evolution of the deformation, which are evaluated by exploiting a whole set of multiple differential interferograms. These approaches require that complex processing chains are used. In this chapter, a complete overview of the involved procedures, emphasizing the role played by the different data inversion algorithms will be proposed.
- Chapter III - While the D-InSAR approach has been first applied to the analysis of single deformation episodes, now is a growing interest on extending this technique to the study of the temporal

evolution of the detected displacements via the generation of deformation time-series. To do this, the information available from each interferometric data pair must be properly related to those included in the other acquisitions via the generation, and a subsequent combination, of an appropriate sequence of D-InSAR interferograms. Thus, the profitably information is essentially associated to phase terms, only. Moreover, the measurable phase are restricted to the $[-\pi,\pi]$ interval, that is the integral number of phase cycles on each measurement is lost. We refer to the procedures recovering the full phase term as Phase Unwrapping (PhU). This chapter will be focused on the analysis of the PhU algorithms and, to adequately introduce it, a short overview of the basic theory concerning this issue will be firstly presented. After that, we will concentrate on the presentation of a novel PhU approach, developed within the doctoral studies, that represent an extension of the Minimum Cost Flow (MCF) algorithm, to the Temporal/Perpendicular baseline domain.

- Chapter IV - This chapter will concern the extension of the original multiple interferogram analysis to the case where the available SAR data are collected by different sensors. In particular, we will refer to the combination of the ERS1/2 SAR data with those acquired by the new European satellite ENVISAT.
- Chapter V - This chapter will finally address the application of the formerly presented D-InSAR approaches to real cases, stressing in particular the role played by the different interferometric distribution which can be considered, thus concentrating in particular on the application of the Extended Minimum Cost Flow (E-MCF) phase unwrapping algorithm (see chapter III) to a properly chosen, interferometric data distribution. For this purpose, several independent SAR data-set will be used and the achieved results will be investigated. A discussion concerning the achieved results and the future improvement of the presented D-InSAR techniques will be finally considered.

Chapter 1

SAR Interferometry

Synthetic Aperture Radar (SAR) is a coherent active microwave remote sensing system, whose capability to effectively map the scattering properties of the Earth's surface has been already intensively investigated.

A SAR sensor, which can be mounted on-board to an aircraft and/or a satellite, has a side-looking illumination direction and is able to perform accurate distance measurements between the moving platform and the surface. Both the acquisition geometry and the physical characteristics of the scene contribute to the formation of the received backscattered radar signal (echo) which, properly processed, leads to the reconstruction of a complex high resolution SAR image. Moreover, being an active imaging sensor, it does not need of an external energy source to work and, exploiting of the microwave region of the electromagnetic spectrum, can be effectively used to detect areas affected by a significant clouds' cover. As a consequence of its flexibility, SAR technology mostly improved during the last years and further techniques have been also developed, thus helping the scientific community on the interpretation of several geophysical phenomena.

One of the major applications of the SAR technology is represented by the SAR interferometry (InSAR) technique which exploits, in its basic form, the phase difference of (at least) two complex-valued SAR images (acquired from different orbit positions and at different times) to measure several quantities, such as topography, deformation, etc…

This work will be focused on the study of Advanced InSAR techniques and on their matter-of-fact applications. This chapter, in particular, will address the key topics of the SAR technology, with a particular emphasis on the InSAR applications.

1.1 SAR History

Since the 1950's when Carl Wiley [1] made his first observations about the "Doppler beam-sharpening" phenomenon, SAR designs and related applications have grown exponentially.

In 1974 an alliance between JPL (Jet Propulsion Laboratory) engineers with a group of international ocean scientists led the National Oceanic and

Atmospheric Administration (NOAA) to determine if an ocean application satellite, featuring a space-based SAR, could be achieved. Their efforts were directed to the realization of a satellite SAR system, which was launched in 1978 onboard to SEASAT [2].

SEASAT operated successfully from the late June to early October 1978 and, although explicitly designed to observe the ocean, was the first Earth observation satellite to provide SAR data suitable for interferometry. The interferometric effectiveness of the SEASAT SAR data for topographic mapping was, in fact, demonstrated eight years later by Zebker & Goldstein [3] and for detection and mapping of small elevation changes by Gabriel et al. [4]. It was followed by the Shuttle Imaging Radar-A (SIR-A) and SIR-B [5] flown in 1981 and 1984, respectively. Both radars were variations on the SEASAT radar, operating at L-band and HH polarization.

The 1990's witnessed a significant expansion of SAR missions with the launch of five Earth-oriented SAR satellites, as well as the pioneering interplanetary use of the Magellan SAR [6] to map Venus. The NASA continued with the Space Shuttle Imaging Radar SAR mission in 1994. The novel radar system was named SIR-C [7] and flown, in April and October, onboard to Endeavor. The SAR sensor, which operated simultaneously at three different frequencies (C-band, L-band and X-band) alternatively transmitting and receiving at both horizontal and vertical polarization, was developed by JPL, DLR (German Aerospace Center) and ASI (Italian Space Agency). Nevertheless, the real breakthrough in SAR interferometry has been achieved by the twin European ERS-1/2 (European Remote Sensing Satellite) sensors [8], launched in 1991 and 1995, respectively, which, with respect to the stability, calibration, etc., represent nowadays the best goal achieved with SAR in the interferometry area. Moreover, a TANDEM mission, during which the two sensors operated in parallel, with ERS-2 followed ERS-1 on the same orbit with only one day of delay, was accomplished. The generated TANDEM interferograms presented an excellent phase quality and, therefore, very precise topographic maps were produced.

Also Japan and Canada gained a SAR system in 1992 (JERS) and in 1995 (Radarsat), respectively, but asset problems limited the real exploitation of these sensors.

The C- and X-band portions of the SIR-C radar were again flown in 2002 for the Shuttle Radar Topography Mission (SRTM) [9]. During this flight, a second receiving antenna was placed at the end of a 60 m mast, extended perpendicular to the main radar antenna. The purpose of the mast antenna was to provide a second receiving point in space for each radar pulse. The slight variations in phase will be processed into a height measurement of the reflecting point on Earth's land surface. During the 10-

day flight, the space shuttle imaged the Earth between 60 degrees north and south latitude and a high quality, high resolution Digital Elevation Model (DEM) could be computed.

In practice, for more than a decade SAR images from space have been available on a reliable routine basis for scientific, public, and commercial users, independent of weather and daylight conditions. The most successful SAR workhorses have been ERS-1/2, JERS [10], Radarsat-1, and, since March 2002, ENVISAT [11]. Although the design of the ERS radars was guided by oceanographic questions, soon after the launch, interferometric (InSAR) applications took over. Generation of digital elevation models (DEMs), measurement of glacier flows, and mapping of earthquakes, volcanoes and subsidence are the most prominent fields of interest today. The majority of interferometric applications today uses data of ERS-1/2 and RADARSAT (both C-band SARs) while the only source of L-band data was the late Japanese JERS. Besides, a new generation of SAR satellites is now approaching: the German SARLupe and TerraSAR-X, the Canadian Radarsat-2, the Italian COSMO-Skymed and the Japanese Advanced Land Observing Satellite (ALOS) [12]. They embody a lot of novel features, such as higher resolution, polarimetry, splittable antennas, and spot-light imaging mode. In this context, a key role could be played in the future, in particular, by the ALOS-PALSAR system (launched in January, 24th 2006), which should complement existing satellites as well as permitting InSAR over vegetated or other rapidly-changing landscapes.

The more modern systems present a variety of imaging modes, which offer the possibility to expand the present-day interferometric data archive, by exploiting both high resolution and wide swath ScanSAR [13] modes. Clearly, the possibility of the ScanSAR interferometry to generate wide-swath products in a single shot is highly attractive.

1.2 SAR Principles

A radar self-illuminates an area on the ground by transmitting a series of electromagnetic pulses and, after an accurate measure of the time delay between the transmitted and the received echoes, is able to figure out the distance (called slant range) between the sensor position along its flight direction (azimuth) and the illuminated targets on the ground. A radar system is well-characterized by its attainable spatial resolution, which measures the ability to distinguish two properly-separated objects. More precisely, if the objects are sufficiently separated, each will be located in a different resolution cell and will be discernible but, if not, the radar return will be a complex combination of the reflected energy from the two objects.

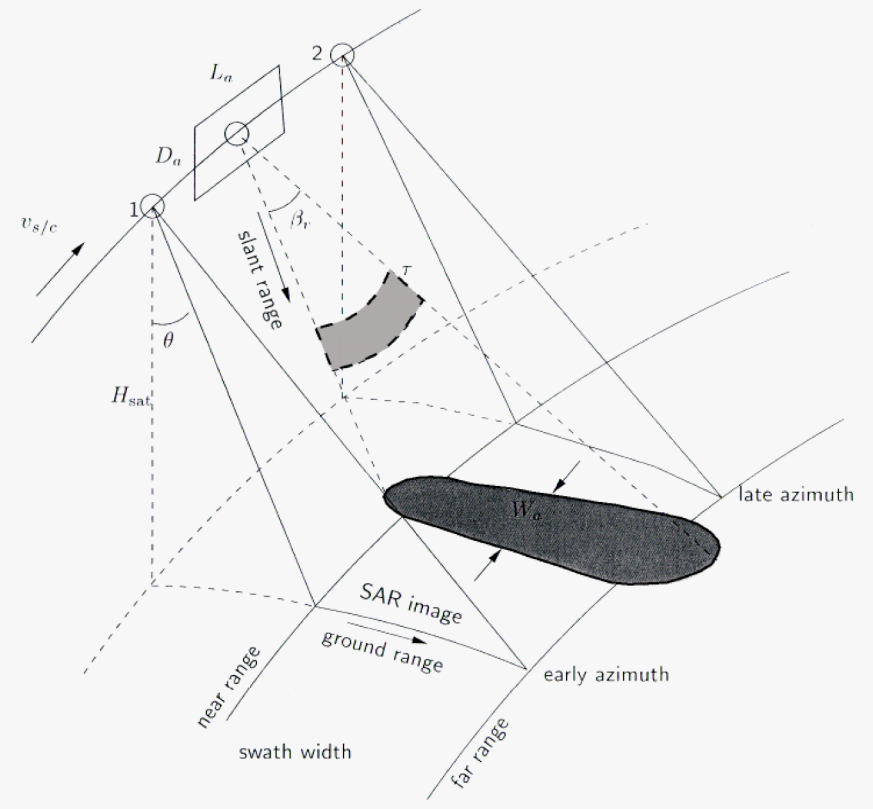

Figure 1. 1 The configuration of a side-looking Real Aperture Radar (RAR).

With regard to the range spatial resolution, we can observe that two objects δr-away can be effectively discriminated if the received pulses (of width τ), are completely separated, only. Since δr corresponds to a time difference $\Delta t = 2\delta r/c$ (where c is the speed of the light), the previous condition implies that

$$\delta r \geq \Delta r_{SR} = \frac{c\,\tau}{2} \tag{1}$$

wherein Δr_{SR} is the theoretical slant range resolution, which can be also expressed, in a more generalized way, as a function of the corresponding pulse bandwidth ($\Delta f \cong 1/\tau$)

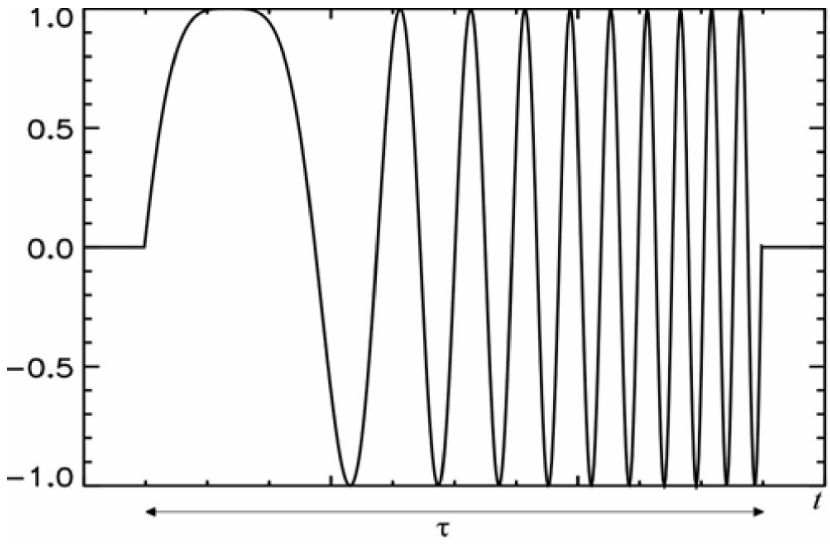

Figure 1. 2 Chirp waveform ($\alpha >> 0$).

$$\Delta r_{SR} \cong \frac{c}{2 \cdot \Delta f} \tag{2}$$

Moreover, it is usually preferred to refer to the ground range resolution, defined as the minimal distance on the ground that allows recognizing two distinct objects, which can be in turn obtained as the projection of the slant resolution (2) on the ground (see Figure 1.1)

$$\Delta r_{GR} \cong \frac{c}{2 \cdot \Delta f \cdot \sin(\theta)} \tag{3}$$

wherein θ is the radar look angle. To give an example, if the ERS-1/2 parameters collected in Table 1.1 were considered, a corresponding ground range resolution of about 25 m would be retrieved.

The equation (1) suggests that finer resolutions can be achieved by using very short duration pulses only, thus requiring high peak power for a prescribed mean power operation. To overcome this problem, modern radar systems (including SARs, also) transmit long linear frequency modulated pulses (called chirp, see Figure 1.2)

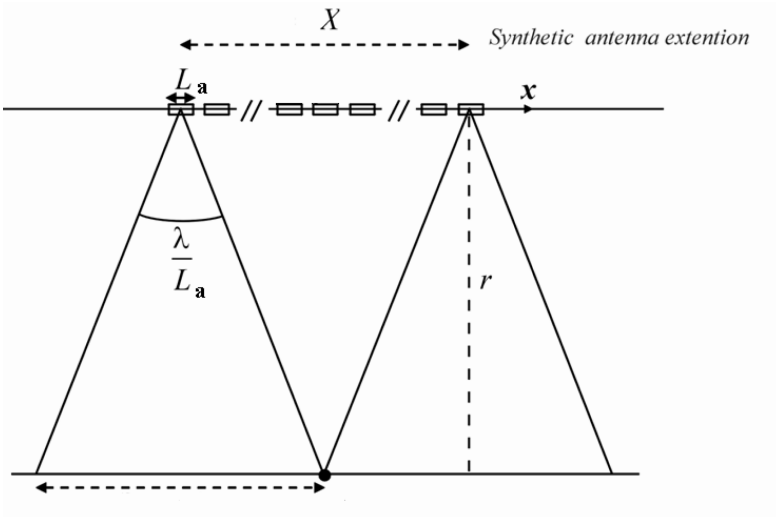

Figure 1. 3 Representation of the synthetic aperture formation: the radar sensor synthesizes a larger antenna via an alignment of short aperture ones.

$$p(t) = \cos\left(2\pi f_o t + \frac{\alpha}{2}t^2\right) rect\left(\frac{t}{\tau}\right) \tag{4}$$

where f_0 is the carrier frequency, α the so-called chirp rate and $rect(t/\tau)$ stands for a rectangular pulse of width τ; it can be easily shown that, for large values of $\alpha\tau^2$, we will have

$$\alpha\tau = 2\pi\Delta f \tag{5}$$

that, if substituted in equation (2), leads to the following slant range resolution expression

$$\Delta r_{SR} \cong \frac{c}{2\cdot\Delta f} \cong \frac{\pi c}{2\alpha\tau} \tag{6}$$

Therefore, the use of pulses with larger durations ($\tau = 10^{-6}\,\mathrm{sec}$), coupled with very large chirp rates ($\alpha = 10^{14}\,rad\cdot\mathrm{sec}^{-2}$), allows achieving slant resolutions of some meters (for example, by referring to the ERS case, we will have $\Delta r = 9.6\,m$).

In the direction orthogonal to the radar beam (azimuth), optical sensors and real aperture radars (RARs) obtain their resolution through the physical

dimensions of their aperture. They correspond to the antenna azimuth footprint X, related to the antenna beam width λ/L_a by means of this relation

$$\Delta x_{RAR} = X = r\frac{\lambda}{L_a} \tag{7}$$

where L_a is the (actual) antenna dimension along the azimuth direction. To give an idea of the achievable azimuth resolutions, let us apply equation (7) to the ERS sensor parameters collected in Table 1.1: the achievable azimuth resolution will be of the order of some kilometers that is, obviously, not acceptable for most applications. One way to obtain better azimuth resolutions is to reduce the operational wavelength and/or to increase the antenna dimension. Besides, the wavelength value is constrained by the system characteristics and the increase of the antenna dimension is not an easy task to be accomplished, unless we implement the synthetic antenna (or aperture): "a very large antenna is synthesized by moving along a reference path a real one of limited dimension" (see Figure 1.3). The synthesis is carried out by coherently combining the back-scattered echoes received and recorded along the flight path. The improvement on the achievable azimuth resolution can be explained by observing that the extension of the synthesized array of antennas is equal to the antenna azimuth footprint X, which will correspond, accounting of the round-trip path of the signal, to the equivalent antenna beam width $\lambda/2X$, so that the relevant azimuth resolution can be expressed as

$$\Delta x_{SAR} = r\frac{\lambda}{2X} = \frac{L_a}{2} \tag{8}$$

As a result, the azimuth resolution is independent of the target-to-sensor distance, and is a function of the (actual) antenna dimension along the azimuth direction (that is of the order of some meters), only.

1.2.1 SAR image formation

This sub-section will address the key aspects of the SAR imaging procedure that leads to generate a complex SAR image of the illuminated area. In particular, we will refer to the more generalized "squinted SAR acquisition geometry", depicted in Figure 1.4, characterized by the presence of an offset pointing angle ϕ (referred to as squint angle) from the radar antenna with respect to the direction perpendicular to the flight path.

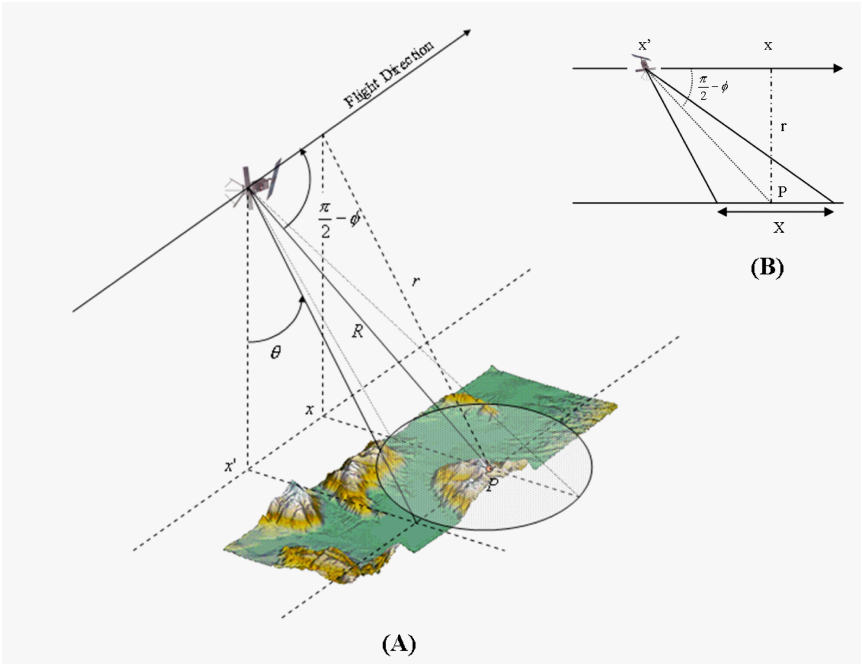

Figure 1. 4 Squinted SAR reference geometry. A) Three-Dimensional representation, B) the perspective view on the equi-range plane containing the flight path and the generic target P.

Let us consider a cylindrical reference system with the axis coincident to the flight direction and denote with:

- (x,r) the azimuth and (slant) range coordinates of the generic illuminated scattering point P, respectively;
- $\theta(x,r)$ the soil surface equation in cylindrical coordinates (that is to say look angle);
- R the target-to-antenna distance relevant to the generic antenna position.

Moreover, let us consider a radar system working with a single antenna in a synchronized transmit/receive mode and, for sake of simplicity, suppose it transmits and receives the same pulse at the same position (*stop and go approximation*).

First of all, to investigate the radar signal characteristics, let us refer to the recorded echo (raw data) corresponding to a generic target of SAR coordinates (x,r). Accordingly, we think of the SAR system as transmitting,

at the generic instant $t_n - \tau$, a chirp pulse (see equation (4)), which can be easily treated by introducing the following complex representation

$$s(t) = \exp\left[j\left(2\pi f_0 (t - t_n) + \frac{\alpha}{2}(t - t_n)^2 \right)\right] rect\left(\frac{t - t_n}{\tau} \right) \tag{9}$$

The relevant backscattered and onboard received signal, obtained by taking account of the transmitted/received signal time delay, will be hence expressed as follows

$$\begin{aligned} s_{received}(t) = \exp\left\{ j\left[2\pi f_0 \left(t - t_n - \frac{2R}{c} \right) + \frac{\alpha}{2}\left(t - t_n - \frac{2R}{c} \right)^2 \right]\right\} \cdot \\ \cdot rect\left(\frac{t - t_n - \frac{2R}{c}}{\tau} \right) \end{aligned} \tag{10}$$

and, neglecting the fast-varying $\exp(j2\pi f_0 t)$ term (because it is cancelled by the heterodyne receiver) and introducing the coordinate transformation $t' = t - t_n = 2r'/c$ to manage with spatial coordinates, only, we will have

$$\begin{aligned} s_{received}(x' - x, r' - r, r) = \gamma(x, r) \exp\left[j\left(-2\pi f_0 \frac{2R}{c} + \frac{\alpha}{2}\left(\frac{2r' - 2R}{c} \right)^2 \right)\right] \cdot \\ \cdot rect\left(\frac{\frac{2r' - 2R}{c}}{\tau} \right) w^2 \left(\frac{\frac{x' - x - r\tan\phi}{v_s}}{\frac{X}{v_s}} \right) \end{aligned} \tag{11}$$

where:

- $x' = v_s t_n$ represents the azimuth coordinate of the antenna phase center;
- $\gamma(x, r)$ is the reflectivity function of the target P, which is proportional to the ratio between the backscattered and the incident field;

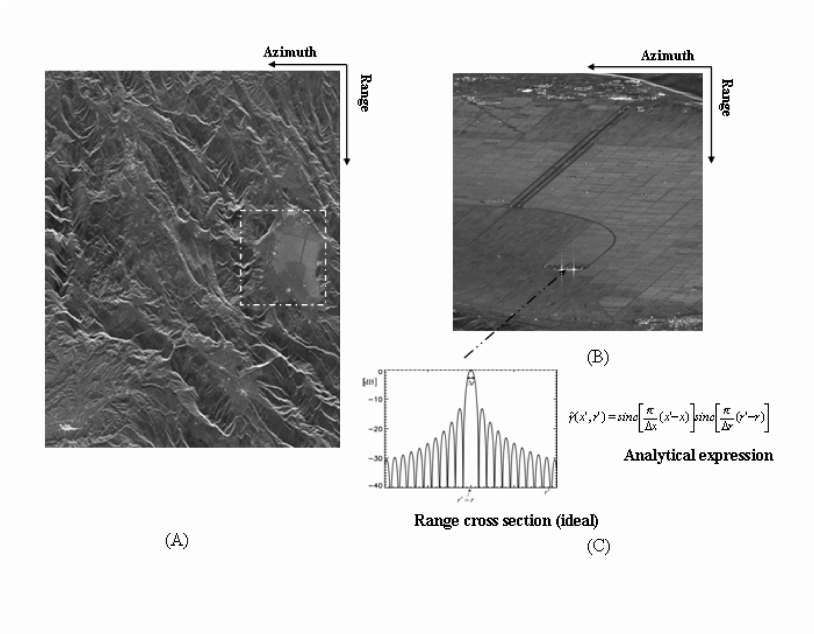

Figure 1. 5 A) The SAR amplitude image relevant to the Central Apennines region (Abruzzo, Italy). The dotted, highlighted rectangular area (B) refers, in particular, to the Piana-del-Fucino region, characterized by the presence of several cultivated plots of land. Moreover, the highly reflective targets here clearly visible are relevant to a ground station antennas system. Obviously, the focused radar returns associated to the antennas, being viewed as point-wise scatterers, is directly representative of the impulse response of the SAR system.

- $w^2(\cdot)$ is the antenna illumination function, related to the azimuth antenna footprint over the ground, properly squared to account that the same antenna operates both in receiving and transmitting mode;
- X is the antenna azimuth footprint, whose general expression, taking account of the squint angle (see Figure 1.4B) is now $X = \lambda r / L_a \cos^2 \phi$.

Although a comprehensive description of the overall SAR image processing step (usually referred to as focusing procedure) is outside the scope of this work, we will present its key aspects, by referring the reader back to [14-18] for a more detailed one.

We firstly observe that the target-to-antenna distance R can be expanded around the position $\overline{x} = x' - r \tan \phi$

$$R \cong \frac{r}{\cos\phi} - \sin\phi\left[x' - x + r\tan\phi\right] + \frac{\cos^3\phi}{2r}\left[x' - x + r\tan\phi\right]^2 \qquad (12)$$
$$R = r + \Delta R$$

In this manner, equation (11) will be expressed as follows

$$s_{received}\left(x' - x, r' - r, r\right) = \tilde{\gamma}\left(x, r\right) \cdot g\left(x' - x, r' - r, r\right) \qquad (13)$$

where:

- $\tilde{\gamma}\left(x,r\right) = \gamma\left(x,r\right) \cdot \exp\left[-j\frac{4\pi}{\lambda}r\right]$ is the product of the scene reflectivity function and the round-trip phase term (representing the core for the InSAR applications);
- $g\left(x' - x, r' - r, r\right) = e^{-j\frac{4\pi}{\lambda}\Delta R + j\frac{2\alpha}{c^2}\left(r' - r - \Delta R\right)^2} rect\left[\frac{r' - r - \Delta R}{\frac{c\tau}{2}}\right] w^2\left[\frac{x' - x + r\tan\phi}{X}\right]$ is the SAR raw-data impulse response.

Let us now move toward the SAR raw data collected in the presence of an extended scene. In the situation of a continuous distribution of scatterers, described by the reflectivity pattern $\gamma\left(x,r\right)$, the raw data can be obtained from equation (13) by superimposing all the elementary returns from the illuminated surface, hence

$$h\left(x', r'\right) = \iint \tilde{\gamma}\left(x', r'\right) g\left(x' - x, r' - r, r\right) dx dr \qquad (14)$$

The equation (14) represents the basic functional form of the SAR raw signal. It exhibits the relationship between the recorded signal $h(\cdot)$, the reflectivity pattern $\gamma(\cdot)$, and the SAR system impulse response $g(\cdot)$. It clearly shows that the SAR imaging problem can be managed via an appropriate filter operation, that recovers a high resolution estimation of the reflectivity pattern $\gamma(\cdot)$, starting from the received signal (i.e., the raw data $h(\cdot)$).

Finally, the focusing procedure, concisely described in the Appendix A for a simplified case, leads to the following SAR image expression

$$\hat{\gamma}\left(x', r'\right) = \iint \gamma\left(x, r\right) \exp\left(-j\frac{4\pi}{\lambda}r\right) \operatorname{sinc}\left[\frac{\pi}{\Delta r}\left(r' - r\right)\right] \cdot \operatorname{sinc}\left[\frac{\pi}{\Delta x}\left(x' - x\right)\right] \exp\left[j\xi_{dopp}\left(x' - x\right)\right] dx dr \qquad (15)$$

where:

- the *sinc*(·) function, whose role will be essential to estimate the achievable spatial resolution of a SAR system, is the so-defined one: $sinc(x)=\frac{\sin x}{x}$ and is characterized by a 3dB-main lobe aperture equal to $\Delta A_{3dB}=0.88\pi\equiv\pi$;
- ξ_{dopp} is the central angular frequency value, which, properly converted in Hz, leads to the expression of the so-defined doppler centroid frequency (see Appendix A);
- $\Delta x=\frac{L_a}{2}$ and $\Delta r=\frac{c}{2\Delta f}$ (as demonstrated in the following) are the achievable azimuth and range resolution expressions, respectively.

To verify the assertions concerning the achievable resolutions, we may observe that, if we refer to a scene characterized by a single scatterer located at the SAR coordinates (x_P,r_P), the scene reflectivity function can be expressed as $\gamma(x,r)=\gamma_P\delta(x'-x_P)\delta(r'-r_P)$ and, the estimated reflectivity value, with respect to the equation (15), will be

$$\hat{\gamma}(x',r')=\gamma_P e^{-j\frac{4\pi}{\lambda}r_P}\,\mathrm{sinc}\left[\frac{\pi}{\Delta r}(r'-r_P)\right]\mathrm{sinc}\left[\frac{\pi}{\Delta x}(x'-x_P)\right]e^{j\xi_{dopp}(x'-x_P)} \tag{16}$$

The information associated to the single scatterer is now spread around its true position over an area corresponding to the 3dB main-lobe aperture of each $\mathrm{sinc}(\cdot)$ function. Hence, the spatial resolutions can be estimated via the observation that two different targets are, in any case, discernible if their spatial separation is smaller than the spatial main lobe aperture of the relevant $\mathrm{sinc}(\cdot)$ function, that is

$$\begin{aligned}&\frac{\pi}{\Delta r}|r_1-r_2|\geq\pi\rightarrow|r_1-r_2|\geq\Delta r=\frac{c}{2\Delta f}\\&\frac{\pi}{\Delta x}|x_1-x_2|\geq\pi\rightarrow|x_1-x_2|\geq\Delta x=\frac{L_a}{2}\end{aligned} \tag{17}$$

which are congruent with those obtained in the previous section in application of the SAR basic principles, only (see equations (2) and (8)).

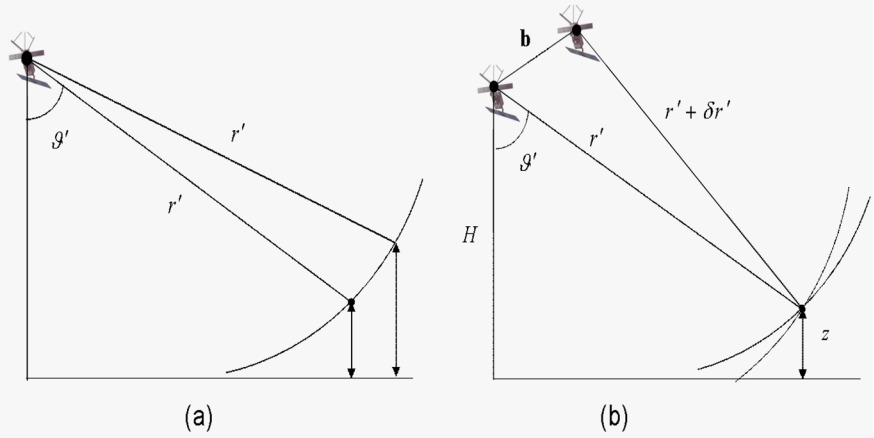

Figure 1. 6 Geometry in the plane orthogonal to the flight direction with a single sensor (a) and in the stereometric (b) case.

Finally, a focused SAR image can be expressed via the equation (4) and managed as a complex-valued matrix, and each resolution cell corresponds to a pixel on the SAR image.

Therefore, as suggested by the Nyquist condition, the pixel dimensions will be, generally, greater than the theoretical resolutions and they will account for the range sampling frequency (f_{samp}) and the Pulse Repetition Frequency (PRF), respectively, that is

$$\begin{aligned} \Delta r &= \frac{c}{2\Delta f} \geq \frac{c}{2 f_{samp}} = \Delta r_{PIXEL} \\ \Delta x &= \frac{L_a}{2} = \frac{v_s}{\Delta B_{azimuth}} \geq \frac{v_s}{PRF} = \Delta x_{PIXEL} \end{aligned} \tag{18}$$

where $\Delta B_{azimuth} = 2v_s / L_a$ is the azimuth bandwidth (see Appendix A). For example, if we refer to the ERS parameters collected in Table 1.1, we have $\Delta r_{PIXEL} = 7.91m$ (which corresponds to a ground pixel spacing of about 20 m) and $\Delta x_{PIXEL} = 4.22m$, respectively.

We finally stress that each single SAR image can be also effectively analyzed via the inspection of the relevant amplitude and phase component, respectively. The amplitude is related to the backscattering coefficient of the ground, while the phase contains information about the travel distance of the emitted signal.

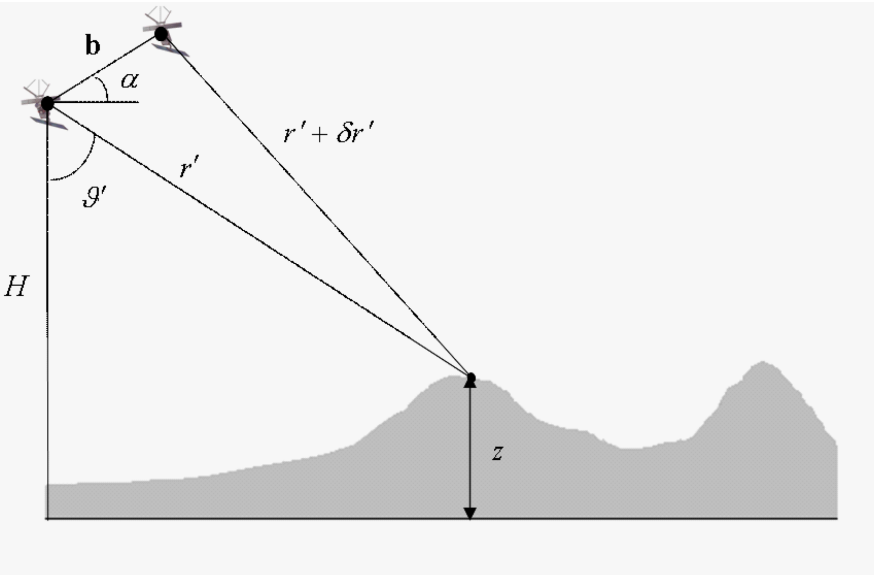

Figure 1. 7 Repeat-Pass acquisition geometry used within stereometric/interferometric applications. SAR sensor observes the same scene from slightly different orbital positions thus leading to the reconstruction of the topography of the scene.

1.3 Determination of the Ground Topography

In this section, we will focus on the exploitation of the SAR images to reconstruct digital elevation model (DEM) of the observed area and, in the following, we will introduce the main topics about the Interferometric Synthetic Aperture Radar (InSAR) techniques [19].

As explained in the previous section, a SAR is able to measure, with a certain resolution, the azimuth and range coordinates of the illuminated targets but, obviously, this is not sufficient to unambiguously locate them, thus estimating its height with respect to a reference plane (or, in general, with respect to a "*reference surface*"). Therefore, with regard to the generic position of the sensor along its flight path, all targets within the range beam located along an equidistance curve will be imaged at the same range position (see Figure 1.6a). This problem can be circumvented if, at least, two different images of the same area, made from separate, known flight tracks are considered. Therefore, the elevation of an object that appears in both images can be determined via the stereometry [20].

The two SAR images can be either collected by means of a single-pass imaging system (characterized by the presence of two distinct antennas: the former operating in a receive/transmit mode and the latter in the receive

mode, only), or with two repeat-passes of a single imaging sensor over the same area.

1.3.1 Stereometry

Let us suppose the first flight track is flown at height H, and the second one at a distance b (usually referred to as *baseline*) from the first one, with an elevation angle (the angle between the vector connecting the first sensor to the second one and the horizontal direction) equal to α (see Figure 1.7). A method (stereometry) to uniquely locate imaged targets and therefore to determine their heights above the reference plane is easily derived. Therefore, if the same object can be identified in both images, then its slant range distances $R_1 = r'$ and $R_2 = r'+\delta r'$ from the first and the second flight track can be estimated, respectively. In this manner, the unknown height respect to the reference plane z can be unambiguously determined, in application of the cosines' law, by searching for the solution of the following two equations in the (z, ϑ') unknowns (see Figure 1.7)

$$R_2^2 = (r'+\delta r')^2 = r'^2 + b^2 - 2r'b\sin(\vartheta'-\alpha) \tag{19}$$

$$z = H - r'\cos\vartheta' \tag{20}$$

where $\delta r'$ is the measured slant range difference between the two sensor tracks.

Unfortunately, this method is very sensitive to errors in the knowledge of the range difference. Actually, the two range distances are measured via the inspection of the two images but, also neglecting possible orbital parameters inaccuracies, the measurement precision is however limited by the error involved in the knowledge of the path difference $\delta r'$, which essentially depends on the range system resolutions. Therefore, these errors will be magnified, if we refer to the height accuracy.

To demonstrate the validity of this statement, we use the chain rule for the derivative calculations, thus obtaining

$$\frac{\partial z}{\partial(\delta r')} = \frac{\partial z}{\partial \vartheta'} \cdot \frac{\partial \vartheta'}{\partial(\delta r')} = r'\sin\vartheta' \cdot \frac{\partial \vartheta'}{\partial(\delta r')} \tag{21}$$

By differentiating the equation (19), we will also have

$$2(r'+\delta r')\partial(\delta r') = -2br'\cos(\vartheta'-\alpha)\partial\vartheta' \tag{22}$$

hence

$$\frac{\partial \vartheta'}{\partial(\delta r')} = -\frac{r'+\delta r'}{br'\cos(\vartheta'-\alpha)} \tag{23}$$

that, properly substituted in equation (21), gives the measure of the sensitivity of z with respect to the accuracy of the $\delta r'$ estimation

$$\sigma_z = \frac{\partial z}{\partial(\delta r')}\sigma_{\delta r'} = \frac{\partial z}{\partial \vartheta'}\cdot\frac{\partial \vartheta'}{\partial(\delta r')}\sigma_{\delta r'} = -\frac{(r'+\delta r')\sin\vartheta'}{b\cos(\vartheta'-\alpha)}\sigma_{\delta r'} \approx -\frac{r'}{b}\sigma_{\delta r'} \tag{24}$$

Obviously, $\sigma_{\delta r'}$ will vary according to the spatial range resolution of the two SAR images so that, if we suppose to be able to discriminate reasonable range displacements of $1/16^{th}$ of the pixel spacing, which is equal to $c/(2f_{samp})$, we will have $\sigma_{\delta r'} = 0.5m$. In turn, for satellite-borne SAR systems, the ratio r'/b is very large; for example, if we consider the ERS parameters (see Table 1.1), for a typical slant range distance of about 800 Km, $\vartheta' \approx 23°$ and a baseline length of 100 m, the achievable height accuracy will be of about 4 Km, which is clearly unacceptable.

The stereometric accuracy can be improved by increasing the baseline value; however, in this case, the backscattered field from a resolution cell may have large variations when this is imaged from two very different viewing angles, thus having an impact on the identification of the corresponding pixels in the two images. This is the reason for which many SAR systems use instead an interferometric method to estimate $\delta r'$.

1.3.2 Interferometry

Interferometric technique [19] exploits the phase difference of two complex SAR images, acquired from different orbit positions and/or at different times, to estimate the position on the ground of the illuminated targets. In principle, different antenna distributions define different interferometer configurations. In particular, the InSAR configurations involve two antennas observing the investigated scene:

- at the same time and from different positions, spaced in the across-track direction (across-track interferometry);
- at different times and from the same position (along-track interferometry);

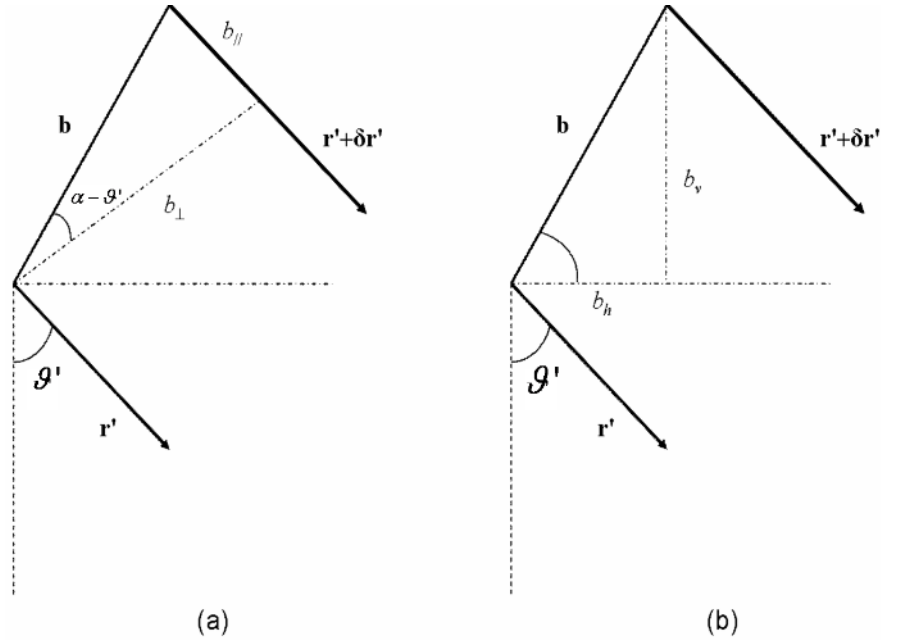

Figure 1. 8 Interferometric baseline geometry. The baseline vector can be effectively decomposed in the perpendicular/parallel components (a) and in the horizontal/vertical components (b), respectively.

- at different times and from different positions (repeat-pass across-track and along-track interferometry).

In the thesis framework, we will focus, in particular, on the across track repeat-pass interferometry, suitable for space-borne applications, with emphasis on the ERS interferometric system, whose general configuration in the plane orthogonal to the azimuth direction is the same used within the stereometric analysis (see Figure 1.7). In this plane, the two SAR antennas are separated by a baseline vector **b** which can be decomposed into either parallel/perpendicular $(b_{//}, b_\perp)$ components or horizontal/vertical ones (b_h, b_v), respectively. It is easy to calculate them through the inspection of Figure 1.8, thus obtaining

$$\begin{cases} b_\perp = b\cos(\vartheta' - \alpha) = b_h \cos\vartheta' + b_v \sin\vartheta' \\ b_{//} = -b\sin(\vartheta' - \alpha) = b_h \sin\vartheta' - b_v \cos\vartheta' \\ b_h = b\cos\alpha = b_\perp \cos\vartheta' + b_{//} \sin\vartheta' \\ b_v = b\sin\alpha = b_\perp \sin\vartheta' - b_{//} \cos\vartheta' \end{cases} \tag{25}$$

where ϑ' is the side-looking angle and α is the elevation angle. The two focused SAR images may be represented (see equation 15) via the following expressions (being $\gamma_1(\cdot)$ and $\gamma_2(\cdot)$ the two distinctive reflectivity function of the illuminated area at the two different acquisition times)

$$\begin{aligned}\hat{\gamma}_1(x',r') &= \iint \gamma_1(x,r)\exp\left(-j\frac{4\pi}{\lambda}r\right)\operatorname{sinc}\left[\frac{\pi}{\Delta r}(r'-r)\right]\cdot \\ &\cdot\operatorname{sinc}\left[\frac{\pi}{\Delta x}(x'-x)\right]\exp[j\xi_{d1}(x'-x)]dxdr \\ \hat{\gamma}_2(x',r') &= \iint \gamma_2(x,r)\exp\left(-j\frac{4\pi}{\lambda}(r+\delta r)\right)\operatorname{sinc}\left[\frac{\pi}{\Delta r}(r'-r-\delta r)\right]\cdot \\ &\cdot\operatorname{sinc}\left[\frac{\pi}{\Delta x}(x'-x)\right]\exp[j\xi_{d2}(x'-x)]dxdr\end{aligned} \tag{26}$$

For the time, let us assume the $\operatorname{sinc}(\cdot)$ functions could be represented as Dirac ones (in other words, we will first refer to the non-realistic case characterized by an infinite bandwidth, corresponding to a zero-valued spatial resolution). In this way, the measured reflectivity returns associated to the two SAR images (regardless to the pixel of SAR coordinates (x',r'))can be expressed as follows

$$\begin{aligned}\hat{\gamma}_1(x',r') &= \gamma_1(x',r')\exp\left(-j\frac{4\pi}{\lambda}r'\right) \\ \hat{\gamma}_2(x',r') &= \gamma_2(x',r'-\delta r)\exp\left(-j\frac{4\pi}{\lambda}r'\right)\end{aligned} \tag{27}$$

The misalignment of the second image (usually referred to as *slave* image) with respect to the first one (*master* image), is clearly due to the path difference between the two radar signals. For this reason, it is needed to properly register the images each other, thus working with the same reference geometry

$$\hat{\gamma}_2(x',r') \to \hat{\gamma}_2(x',r'+\delta r') = \gamma_2(x',r')\exp\left[-j\frac{4\pi}{\lambda}(r'+\delta r')\right] \tag{28}$$

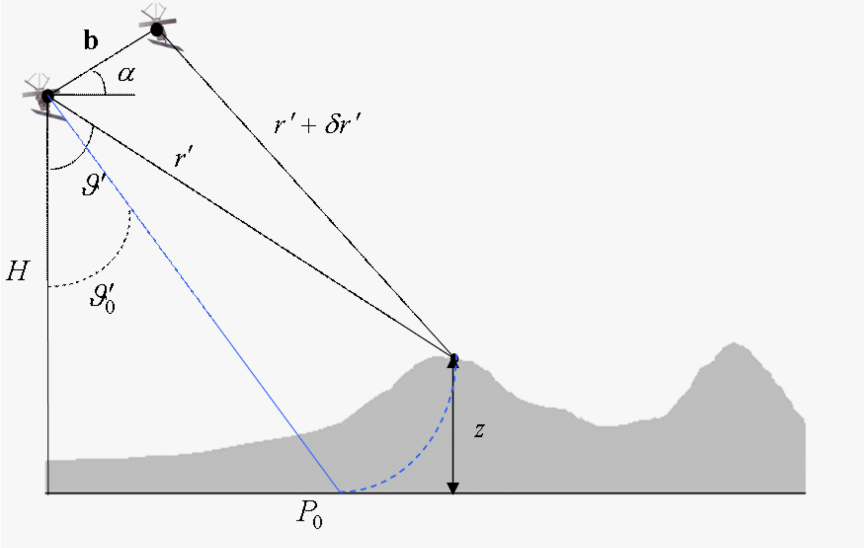

Figure 1. 9 Repeat-Pass interferometric geometry. The position of the imaged target in absence of the topographic pattern has been labeled to as P_0.

From the equations (27) and (28), we generate the complex interferogram, so-defined

$$\hat{\gamma}_1(x',r')\hat{\gamma}_2^*(x',r') = \left|\hat{\gamma}_1(x',r')\right| \cdot \left|\hat{\gamma}_2(x',r')\right| e^{j\frac{4\pi}{\lambda}\delta r' + j\angle\gamma_1(x',r') - j\angle\gamma_2(x',r')} \tag{29}$$

where the (*) operator denotes the complex conjugate operation, while $\angle(\cdot)$ refers to the full phase (i.e., the phase value is not restricted to the $]-\pi,\pi]$ interval) extraction operation. Assuming that the scattering mechanism on the ground has not changed between the two passages of the sensor over the illuminated area (this requirement could be directly accomplished if a single-pass configuration was considered), the measured phase difference (being $\angle\gamma_1(x',r') = \angle\gamma_2(x',r')$) will depend on the imaging geometry, only

$$C(x',r') = \left|\gamma_1^2(x',r')\right|^2 \exp\left[j\frac{4\pi}{\lambda}\delta r'\right] \tag{30}$$

whose full phase term is

$$\Delta\Phi = \frac{4\pi}{\lambda}\delta r' \tag{31}$$

By taking account of the acquisition geometry depicted in Figure 1.7 (as already done for the stereometric case), in application of the cosine rule (see equation 19), we get

$$r' + \delta r' = \sqrt{b^2 + r'^2 - 2br'\sin(\vartheta' - \alpha)} \approx r' - b\sin(\vartheta' - \alpha) \tag{32}$$

where the parallel ray approximation introduced by Zebker and Goldstein [3] has been applied. Hence, the interferometric phase can be written as follows

$$\Delta\Phi = \frac{4\pi}{\lambda}\delta r' \cong -\frac{4\pi}{\lambda}b\sin(\vartheta' - \alpha) = \frac{4\pi}{\lambda}b_{//} \tag{33}$$

This equation effectively solves the problem to locate the single scatterer P on the scene, since it allows measuring the look angle relevant to the selected point, also.

At this stage, our problem concerns the estimation of the topographic measurement accuracy. To achieve this task, first of all, let us recover the relation that connects the interferometric phase and the height profile of the scene (with respect to the reference surface $z = 0$). To do this, by referring to the geometry depicted in Figure 1.9, we expand the equation (33) around the position $\vartheta' = \vartheta'_0$

$$\Delta\Phi \approx -\frac{4\pi}{\lambda}b\left[\sin(\vartheta'_0 - \alpha) + \cos(\vartheta'_0 - \alpha)(\vartheta' - \vartheta'_0)\right] \tag{34}$$

where ϑ'_0 represents the look angle that we should have in presence of the reference surface, only. The height of the target is related to the look angle and the height of the sensor via the equation (20), so that

$$\frac{\partial z}{\partial \vartheta'} = r'\sin\vartheta' \rightarrow \frac{\partial \vartheta'}{\partial z} = \frac{1}{r'\sin\vartheta'} \rightarrow \vartheta' - \vartheta'_0 \approx \frac{z}{r'\sin\vartheta'_0} \tag{35}$$

and, finally

$$\Delta\Phi \approx -\frac{4\pi}{\lambda}b\sin(\vartheta'_0 - \alpha) - \frac{4\pi}{\lambda}b\cos(\vartheta'_0 - \alpha)\frac{z}{r'\sin\vartheta'_0} \tag{36}$$

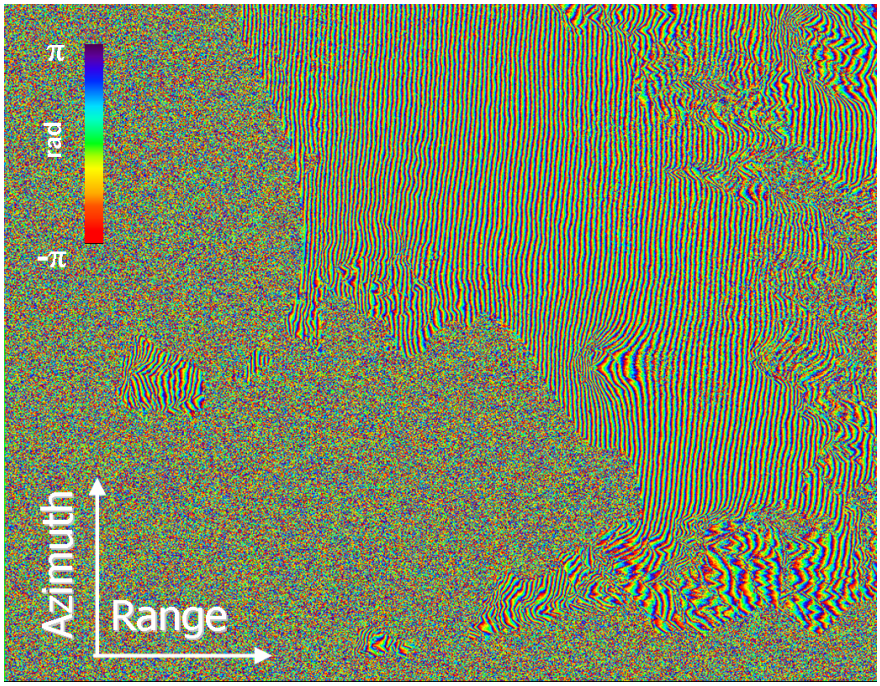

Figure 1. 10 The tandem interferogram computed from the ascending ERS data pair acquired on August 1, 1995 and August 2, 1995. The flat-Earth term is responsible for the fast-varying fringe pattern along the range direction, modulated by the topographic components, itself.

The first term of the equation (36) accounts for the *flat-Earth* contribution and the second one for the topographic profile, respectively. To give an example, in Figure 1.10 a tandem interferogram (whose time delay is equal to one day) is shown. Since the phase difference can be measured only in the interval $[-\pi,\pi[$, it clearly exhibits several fringes, corresponding to the 2π–phase jumps. The *flat-Earth* contribution, in particular, is responsible for the rapid phase change which increases in the range direction (here clearly visible). To clarify the relation that connects the *flat-Earth* term and the range coordinate of the image, let us refer to the more generalized configuration of Figure 1.11, wherein the *Earth-curvature* has been also considered.

The phase difference depends on the parallel component of the baseline and its derivative with respect to the range is

$$\frac{\partial(\Delta\Phi)}{\partial r'}=\frac{\partial}{\partial r'}\left[-\frac{4\pi}{\lambda}b\sin(\vartheta'-\alpha)\right]=-\frac{4\pi}{\lambda}b\cos(\vartheta'-\alpha)\frac{\partial\vartheta'}{\partial r'} \tag{37}$$

We remark that the perpendicular baseline slightly varies with the look angle across a typical SAR image. The change in the look angle usually increases with range; however, when the local terrain slope exceeds the look angle value, an increase in look angle does not produce a corresponding increase in range (this is the so-called *layover phenomenon*).

First of all, we compute the normal phase gradient due to the local curvature of the Earth, by excluding the presence of a height profile, in order to show the dependence of the *Earth-curvature* component with respect to the range. If we refer to Figure 1.11(a) we may apply the cosine rule to the triangle whose vertices are the sensor position, the target position and the Earth center, respectively, thus obtaining

$$R_E^2=\left(R_E+H\right)^2+r'^2-2r'\left(R_E+H\right)\cos\vartheta'_0 \tag{38}$$

where ϑ_0' is the look angle corresponding to the case where the Earth-topography is neglected (indicated to as ϑ' in the Figure 1.11a) Hence, we derive the following formula, which is obviously the generalization of the formula (see equation 20) already obtained by using the *Flat-Earth* approximation

$$\eta=\cos\vartheta_0'=\frac{\left(R_E+H\right)^2+r'^2-R_E^2}{2r'\left(R_E+H\right)} \tag{39}$$

Therefore, since the first derivative of the look angle with respect to the range coordinate can be re-arranged as follows

$$\begin{aligned}\frac{\partial\vartheta'}{\partial r'}&=\frac{\partial\vartheta'}{\partial(\cos\vartheta'_0)}\cdot\frac{\partial(\cos\vartheta'_0)}{\partial r'}=-\frac{1}{\sin\vartheta'_0}\frac{\partial\eta}{\partial r'}\\&=\frac{1}{r'\sin\vartheta'_0}\left(\cos\vartheta'_0-\frac{r'}{R_E+H}\right)\end{aligned} \tag{40}$$

the corresponding phase rate (see equation 37) will be

$$\frac{\partial(\Delta\Phi)}{\partial r'}=\frac{\partial}{\partial r'}\left[\frac{4\pi}{\lambda}b_{//}\right]=-\frac{4\pi}{\lambda}\frac{b\cos(\vartheta_0'-\alpha)}{r'\sin\vartheta_0'}\left(\cos\vartheta_0'-\frac{r'}{R_E+H}\right) \tag{41}$$

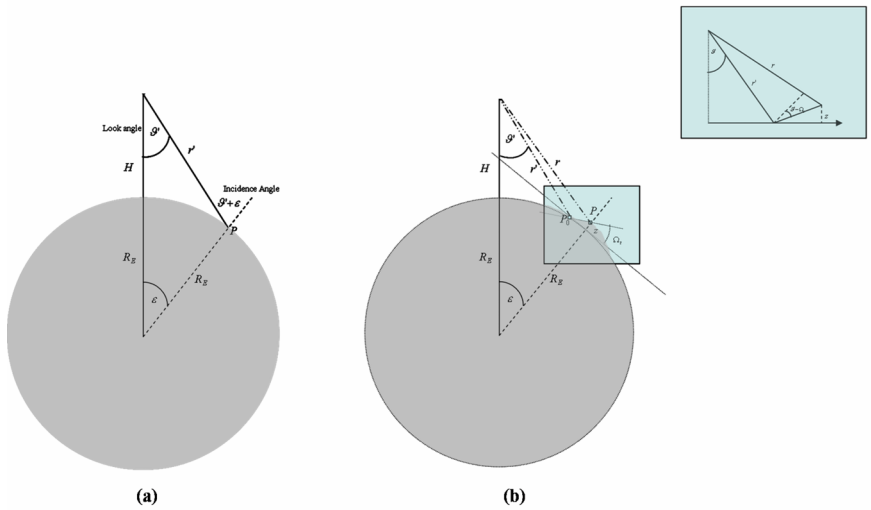

Figure 1. 11 Viewing geometry of a radar sensor used to compute the *Earth-curvature* terms in the interferometric fringes both in (a) a simplified case (where the Earth-topography is neglected) and (b) in the real case.

and, if we apply again the *flat-Earth* approximation (that is equivalent to impose that $r'/(R_E+h)<<1$), we will have a different expression for the *flat-Earth* component (with respect to the expression written in equation (36)), which easily shows how it varies with respect to the range coordinate.

More precisely, if we impose the interferometric phase is equal to zero in a given pixel of SAR coordinates (x'_0, r'_0), the *flat-Earth* term can be now re-arranged as follows

$$\Delta\Phi^{flat}(x',r') = -\frac{4\pi b_\perp}{\lambda r' \tan \vartheta'_0}(r'-r'_0) \tag{42}$$

and, accordingly, the equation (35) can be also expressed as follows

$$\Delta\Phi(x',r') \approx \Delta\Phi^{flat}(x',r') - \frac{4\pi}{\lambda}\frac{b_\perp}{r' \sin \vartheta'} z \tag{43}$$

wherein, for the topographic term expression, the approximation $\vartheta' \cong \vartheta_0'$ has been used. The derivative operation (41) can be profitably generalized

by considering there is also a local topographic slope Ω_t, thus retrieving the local fringe frequency in the range direction, representing, as explained in the following sub-section, a key parameter in interferometry. In particular, the generalized expression of the mentioned equation will be obtained as a trivial extension of the original one, by exploiting the geometry depicted in Figure 1.11b

$$\frac{\partial(\Delta\Phi)}{\partial r'} = -\frac{4\pi}{\lambda}\frac{b_\perp}{r'\sin\vartheta'_{inc}}\left(\cos\vartheta'_{inc} - \frac{r'}{R_E+H} + \frac{R_E+z}{R_E+H}\frac{\sin\Omega_t}{\sin(\vartheta'_{inc}-\Omega_t)}\right) \tag{44}$$

wherein $\vartheta'_{inc} = \vartheta' + \varepsilon$ is the incidence angle (which differs from the side-looking one if the Earth-curvature is considered). Obviously, it can be properly particularized for the *flat-Earth* case, as follows

$$\left.\frac{\partial(\Delta\phi)}{\partial r'}\right|_{Flat-Earth} = -\frac{4\pi}{\lambda}\cdot\frac{b_\perp}{r'\sin\vartheta'}\cdot\left[\cos\vartheta' + \frac{\sin\Omega_t}{\sin(\vartheta'-\Omega_t)}\right] \tag{45}$$

being, in this case, $\vartheta'_{inc} = \vartheta'$. It is easy to demonstrate that

$$\cos\vartheta' + \frac{\sin\Omega_t}{\sin(\vartheta'-\Omega_t)} = \sin\vartheta'\frac{\cos(\vartheta'-\Omega_t)}{\sin(\vartheta'-\Omega_t)} \tag{46}$$

and hence

$$\left.\frac{\partial(\Delta\phi)}{\partial r'}\right|_{Flat-Earth} = -\frac{4\pi}{\lambda}\cdot\frac{b_\perp}{r'\tan(\vartheta'-\Omega_t)} \tag{47}$$

thus finally leading to the following local fringe range frequency expression

$$f_{\Delta\Phi} = \frac{1}{2\pi}\frac{\partial(\Delta\Phi)}{\partial r'} = -\frac{2b_\perp}{\lambda r'\tan(\vartheta'-\bar{\Omega})} \tag{48}$$

where $\bar{\Omega}$ is the mean local slope of the ground. In the following, some considerations about the achievable measurement accuracy will be in order.

For this purpose, we may observe that, according to the equation (43), the height resolution is a function of the phase term accuracy

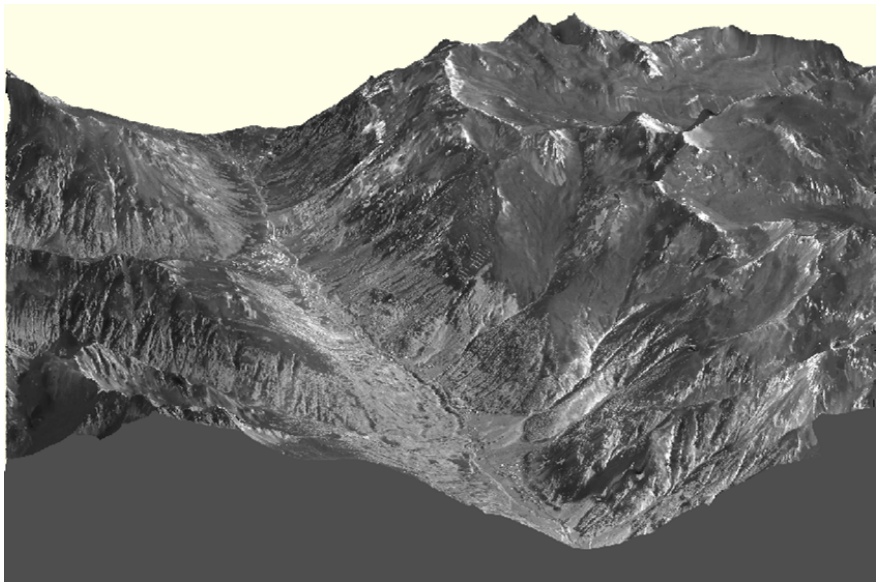

Figure 1. 12 Three-Dimensional representation of a DEM of the Galtuer (Austria) area with superimposed a SAR image of the same area. The DEM were generated by processing the radar returns collected by a SAR sensor, working at the X-band (9.6 GHz) and mounted on-board to an aircraft system. Its height accuracy is approximately equal to 1-2 m (courtesy of the Aerosensing Gmbh).

$$\sigma_z \approx -\frac{\lambda r' \sin \vartheta'_0}{4\pi b_\perp} \sigma_{\Delta\Phi} \tag{49}$$

Hence, to improve our height accuracy, a solution could be represented by the choice of large perpendicular baseline values. Unfortunately, an enlargement of the perpendicular baseline increases, as we are going to clarify in the following, the noise affecting the interferograms, thus magnifying the corresponding phase deviation. For this reason, it is needed a compromise that allows us to establish a criterion to search for an optimal baseline separation value between the two orbits.

To give an example of the achievable accuracy, a typical ERS1-2 configuration, with $r' = 800Km$, $b = 100m$, $\vartheta' = 23°$, $\alpha = 45°$, $\lambda = 5.56cm$, $\sigma_{\Delta\Phi} = 20°$, gives an uncertainty on the height measurement of about $300m$. Accuracy can be also estimated with respect to the whole set of parameters that are present in equation (43) and, for example, to the components of the baseline vector. To do this, we observe that, neglecting the *flat-Earth* term and according to the equations (33) and (43), the topography can be also expressed as a function of the parallel component of the baseline

$$z \simeq \left(\frac{r \sin \vartheta'}{b_\perp} \right) b_{//} = \frac{r' \sin^2 \vartheta'}{b_\perp} b_h - \frac{r' \sin \vartheta' \cos \vartheta'}{b_\perp} b_v \tag{50}$$

so that the height resolution σ_z will depend on the deviation of the baseline components uncertainties, via the following two relations

$$\begin{aligned} \sigma_z &\approx \frac{r' \sin^2 \vartheta'}{b_\perp} \sigma_{b_h} \\ \sigma_z &\approx \frac{r' \sin(2\vartheta')}{2b_\perp} \sigma_{b_v} \end{aligned} \tag{51}$$

As an example, if typical ERS parameters are considered, deviations on each single baseline components equal to $0.01m$ will correspond to a height resolution of approximately $20m$ (with respect to the horizontal component of the baseline) and $35m$ (with respect to the vertical component), respectively. Note also that the presence of the r' term on the expressions (49) leads to a measure, which is highly dependent on the error of the baseline. These effects can be strongly limited by choosing interferometric configuration with larger baseline but, however, small enough to think acceptable the decorrelation effects. The explanation of this effect can be done by observing (see Figure 1.6(b)) that, as the baseline increase the angle with whose the arcs intersects one other increases accordingly, thus diminishing the sensibility to the baseline errors.

Another frequently used measure of interferometric performance is the height ambiguity that represents the amount of height change leading to a 2π change in interferometric phase, and which can be easily achieved by inserting $\sigma_{\Delta\Phi} = 2\pi$ in the equation (49)

$$z_{2\pi} = \left| -\frac{\lambda r' \sin \vartheta'_0}{2b_\perp} \right| \tag{52}$$

Finally, an example of a reconstructed topography scene is shown in Figure 1.12.

1.3.3 Interferometric Phase Statistics

In the following, in order to establish which values of the phase standard deviation could be considered, we will discuss how the noise on the SAR image affects the phase measurements.

First of all, we address the effects of the thermal noise and, accordingly, we add to the SAR image expressions (see equations (26) and (27)) the noise components which are supposed to be mutually incoherent

$$\begin{aligned} I_1(x',r') &= \gamma(x',r')e^{-j\frac{4\pi}{\lambda}r'} + n_1(x',r') \\ I_2(x',r') &= \gamma(x',r')e^{-j\frac{4\pi}{\lambda}(r'+\delta r')} + n_2(x',r') \end{aligned} \tag{53}$$

To introduce a measure about the phase quality, its is useful to refer to the cross-correlation factor, defined as follows

$$\chi = \frac{E\left[I_1 \cdot I_2^*\right]}{\sqrt{E\left[\left|I_1\right|^2\right] \cdot E\left[\left|I_2\right|^2\right]}} = \left|\chi\right| \exp\left(\Phi_{\text{int}}\right) \tag{54}$$

wherein the $E[\cdot]$ symbol stands for the expectation operator. Moreover, these operations are in practice replaced by spatial averages ones and the choice of the optimal averaged boxes is obtained taking account of the original asymmetry between the azimuth and ground range image resolutions.

Therefore, there is a ratio of about $1/4^{\text{th}}$ between the two spatial resolutions, so that a profitably choice would require an averaged spatial box with $N_{az} = 20$ azimuth lines and $N_{rg} = 4$ range samples, leading to an averaged resolution cell, which is approximately squared with a side of about $100m$.

The average procedure, usually referred to as multi-look operation, leads to an improvement of the interferometric phase standard deviation, as outlined in the following. With regard to the multi-looked phases, we also want to stress that, if we want to estimate the phase from N independent interferogram samples, the maximum-likelihood estimator (MLE), which provides the averaged phase difference for distributed, homogenous targets, will be

$$\Phi_{N-look} = \arctan\left[\frac{\mathrm{Im}\left(\sum_{j=1}^{N} I_1(P_j)^* I_2(P_j)\right)}{\mathrm{Re}\left(\sum_{j=1}^{N} I_1(P_j)^* I_2(P_j)\right)}\right] \tag{55}$$

wherein P_j is the j-th SAR pixel within the averaged box and the operators $\mathrm{Im}[\cdot]$ and $\mathrm{Re}[\cdot]$ stand for the extraction operations of the imaginary and the real part of a complex variable, respectively. The basic procedure is pictorially outlined in Figure 1.13 where both a single look and a $N = N_{az} \times N_{rg}$-multi-looked phase interferogram have been shown. Although the evaluation of the statistics of the multi-looked SAR images is outside the scope of this work and can be found in [21-23], the statistics relevant to the interferometric phase pattern will be presented in the following.

We may observe that the cross-correlation factor can be decomposed in an amplitude and a corresponding phase term, respectively. The amplitude, known as *coherence*, ranges between [0,1] and accounts for the similarity of the two images, while the phase corresponds to the multi-looked interferometric phase, directly. A zero coherence stands for a completely uncorrelated scene, whereas a coherence close to 1 corresponds to a noise-free interferogram. In the simplified case of the equation (53) it is particularly easy to express the coherence as a function of the signal to noise ratio (SNR) [15]

$$\chi = \frac{SNR}{SNR+1} \tag{56}$$

Being interested to the estimation of the standard deviation of the interferometric phase, we could relate it to the evaluated coherence value. To this end, it is needed to start by the knowledge of the interferometric probability density function, which can be expressed, for a single-look interferogram, as follows

$$pdf_{Single-Look}(\varphi) = \frac{1-k^2}{2\pi}\frac{1}{1-k^2\cos(\varphi-\varphi_0)}\cdot \cdot\left\{1+\frac{k\cos(\varphi-\varphi_0)\arccos(-k\cos(\varphi-\varphi_0))}{\sqrt{1-k^2\cos^2(\varphi-\varphi_0)}}\right\} \tag{57}$$

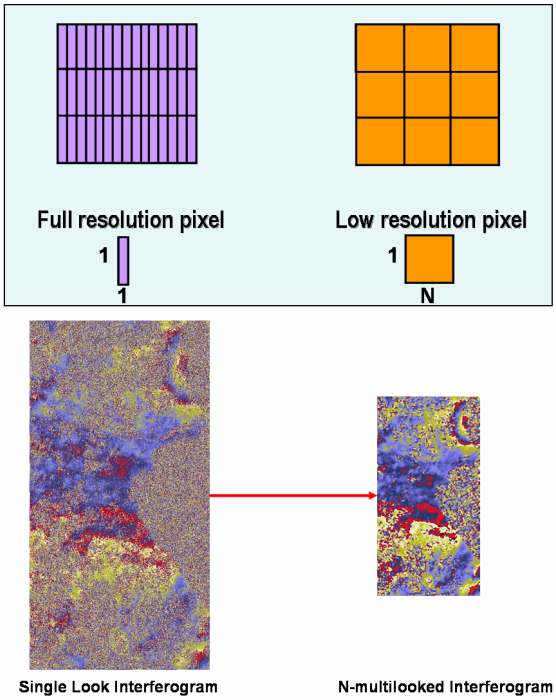

Figure 1. 13 A pictorially representation of the N-multilook operation. The presented interferograms are relevant to the Napoli (Italy) bay area and have been generated from two ERS descending acquisitions (note that they are differential interferograms thus the fringes are related to the deformation of the considered area).

where φ_0 is the actual (noise-free) phase and k is the coherence value (see Figure 1.14(a)). From the observation of its shape, we note that the phase distribution is less dispersed when the coherence approaches to 1. It is clear that the higher are the coherence, the more concentrated around its expectation value is the phase distribution, thus suggesting lower value of the standard deviation. The latter can be also analytically expressed (unless only for the single-look case) as follows [24]

$$\sigma_{\phi_{\text{int}}} = \sqrt{\frac{\pi^2}{3} - \pi \arcsin(k) + \arcsin^2(k) - \frac{Li_2(k^2)}{2}} \tag{58}$$

where Li_2 is the Euler's dilogarithm.

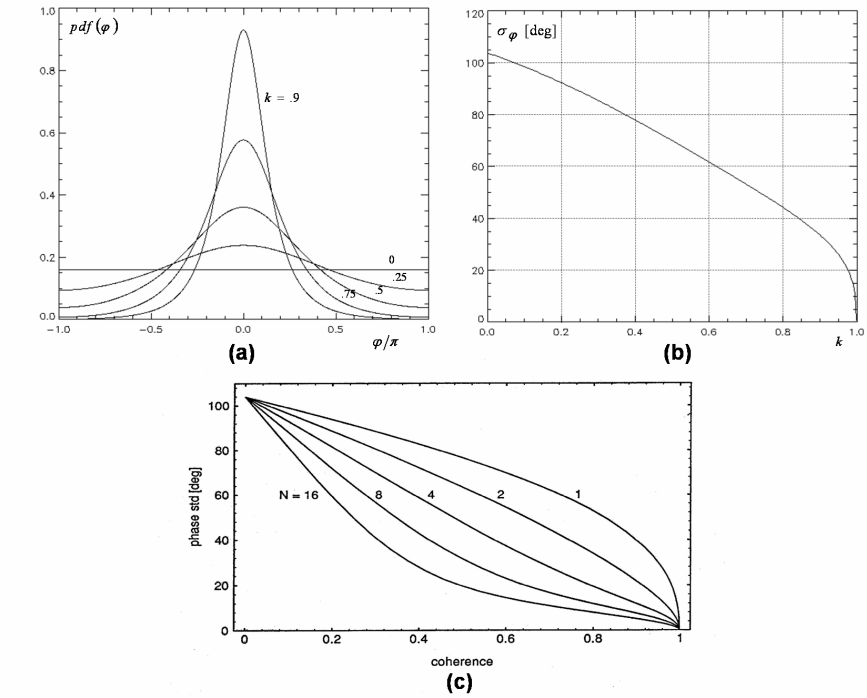

Figure 1. 14 (a) The pdf of a single look phase interferogram as a function of the spatial coherence. (b) The single look phase standard deviation vs. the coherence, which varies as the sample number increase.

In the case of N-multi looked interferograms, the corresponding pdf will be analytically estimated from Montecarlo simulations or calculated by [25-26]

$$pdf_{N-look}(\varphi)=\frac{\Gamma\left(N+\frac{1}{2}\right)\left(1-k^2\right)^N k\cos(\varphi-\varphi_0)}{2\sqrt{\pi}\Gamma(N)\left(1-k^2\cos^2(\varphi-\varphi_0)\right)^{N+\frac{1}{2}}}+ \\ +\frac{\left(1-k^2\right)^N}{2\pi}{}_2F_1\left(N,1;\frac{1}{2};k^2\cos^2(\varphi-\varphi_0)\right) \tag{59}$$

where ${}_2F_1$ is the hypergeometric function.

The important (and expected) result is that the pdf becomes narrower at the increase of the used number of looks. Unfortunately, an exact, analytical

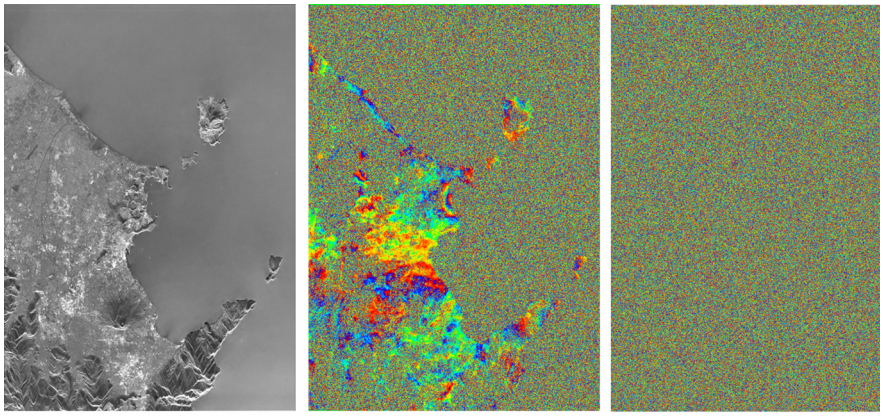

Figure 1. 15 (left side) A multilook SAR image of the Napoli (Italy) bay area, (center) A spatially correlated differential interferogram and (right side) a decorrelated one.

expression for the phase standard deviation, in this case, is not available, unless for the Cramer-Rao bound case (whose validation is nevertheless limited to the high coherence region)

$$\sigma_{\Phi-Nlook} = \frac{1-k^2}{\sqrt{2N}} \tag{60}$$

An empirical relation between the phase standard deviation and the coherence value (for different number of looks) can be however obtained numerically as shown in Figure 1.14 [15]. This kind of representation may be effectively used to estimate the achievable measurement accuracy; indeed, for typical values of coherence of about 0.3 the corresponding single-look phase standard deviation will be of about $\pi/2$ which, properly substituted in the equation (49) and for typical ERS values $b = 100m$, $r' = 800Km$, $\lambda = 5.56cm$ and $\vartheta' = 23°$, will correspond to a topographic height accuracy of about $22m$.

1.3.4 Decorrelation Effects

At this stage, we can address the origin for the coherence decrease. Basically, the cross-correlation factor will depend on the different noise sources and can be profitably factorized as the product of the cross-correlation factors relevant to each single noise source [21], as follows

$$\chi = \chi_{thermal} \cdot \chi_{temporal} \cdot \chi_{spatial} \cdot \chi_{doppler} \cdot \chi_{misregistration} \cdot \chi_{volumetric} \cdot e^{j\frac{4\pi}{\lambda}\delta r'} \quad (61)$$

We will focus on each single factor, thus exploring the SAR parameters that are responsible for them.

First of all, we have to refer to the general expression of a SAR image (see equation 26) in order to investigate on the origin of the decorrelation sources and, for sake of simplicity, let us now neglect both the effect of the different reflectivity functions (responsible for the temporal decorrelation effect) and the thermal noise contributions, respectively. Hence, as demonstrated in [15], we search for the expression of the cross-correlation factor (see Appendix B) that, if no mis-registrations have occurred, can be expressed as

$$\chi = e^{j\frac{4\pi}{\lambda}\delta r'} \cdot \left\{ \Delta r \cdot \Lambda\left[\frac{2\Delta r}{\lambda} \frac{b_{\perp}}{r \tan\left(\vartheta' - \overline{\Omega}_t\right)} \right] \right\} \cdot \left\{ \Delta x \cdot \Lambda\left[\frac{\xi_{d1} - \xi_{d2}}{4\pi} L_a \right] \right\} \quad (62)$$

wherein the $\Lambda\left(\frac{t}{\tau}\right)$ function stands for a triangle pulse of width τ, which is clearly factorizable in two distinct contributions. The former is responsible for the spatial decorrelation effect, that is due to the fact that the same ground resolution cell is imaged from two slightly different looking directions. The change of the incidence angle leads to a shift between the range spectra of the two SAR images that is identical to the local fringe frequency in range (see equation 47). For this reason, if the perpendicular baseline increase, the corresponding spectral shift could be responsible for a complete non overlap between the two range spectra, thus leading to the complete decorrelation case. Mathematically, it happens when

$$\frac{c}{2} \cdot \frac{2b_{\perp c}}{\lambda r' \tan\left(\vartheta' - \overline{\Omega}_t\right)} = \Delta f = \frac{c}{2\Delta r} \rightarrow b_{\perp c} = \frac{\lambda}{2\Delta r} r' \tan\left(\vartheta' - \overline{\Omega}_t\right) \quad (63)$$

which perfectly corresponds to the value obtained by imposing that the relevant contribution on the expression of the cross-correlation factor (see equation (61)) is equal to zero. A solution to avoid this problem, which provides to use two distinct SAR systems with a variable slightly different carrier frequencies, has been also proposed. These systems are usually referred to as Δk-radars (wherein k stands for the angular frequencies) rather than interferometers [27-28]. For the ERS satellites the critical baseline is of

about 1200m for a flat terrain, although baselines greater than 600 m are very difficult to be used. As an example, in Figure 1.15 a direct comparison between an uncorrelated differential interferograms (where the fringes are related to the deformation, as explained in the following) and a correlated one has been also presented, in order to show the impact of the data pair spatial baseline on the subsequent decorrelation phenomena, here clearly visible. The latter term accounts for the doppler decorrelation effects. It is due to the presence of a difference in the two doppler centroids which is equivalent to a resulting azimuth spectral shift between the two SAR images. No spectral overlap is present when:

$$\left|\xi_{d1} - \xi_{d2}\right| > \frac{4\pi}{L_a} \tag{64}$$

Finally, the two explored noise sources can be effectively treated in the Fourier transform domain, being both responsible for a corresponding spectral shift, as pictorially represented in Figure 1.16.

Finally, we have to analyze the effects of a change in the reflectivity

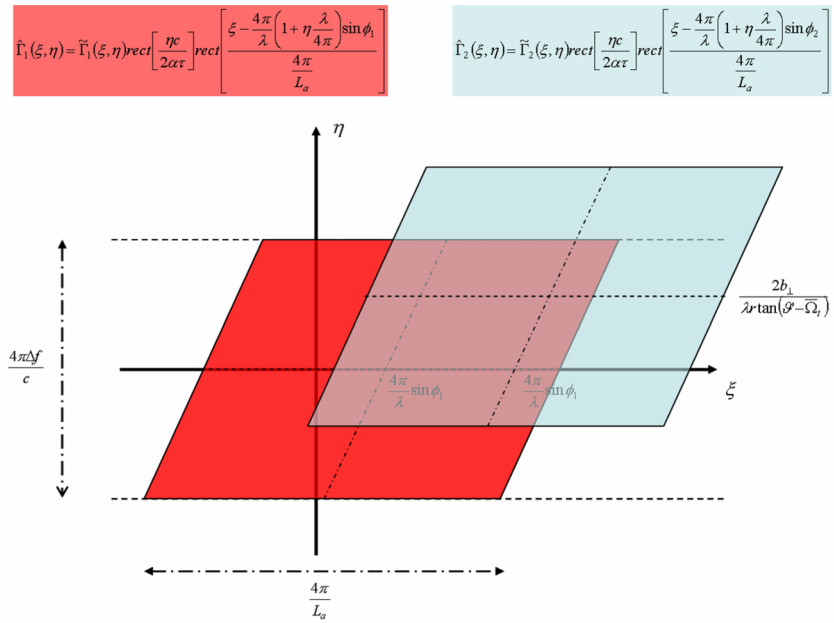

Figure 1. 16 Representation of the two-dimensional spectra of the two generic SAR images involved in the interferometric data-pair.

function between the two passages of the sensor over the illuminated area. The corresponding decorrelation effect, known to as temporal decorrelation, is very difficult to be statistically modeled and is usually associated to weather changes that modify the electromagnetic response of the ground. It can be also due to the human activities (we refer to rural areas, for example) and is strongly dependent on the used wavelength. This dependence is particularly important if vegetated areas are considered, where the use of lower frequencies are preferred. On the other hand, urban zones preserve coherence along time even with very large temporal baselines. Coherence maps (see Figure 1.17) are useful to get one estimate of this type of decorrelation and are often used to generate thematic mps, for instance, vegetation coverage and lava flow characterization in volcanic areas.

1.4 Surface Deformation Mapping

Interferometry can be also effectively used to investigate on the surface changes occurring between the two passages of the radar sensor [29-30].

These techniques allow to estimate the time evolution of an investigated zone on the Earth surface by exploiting the phase difference between two images relative to observations carried out at different times. This technique would require, in principle, that the sensor illuminates the investigated area from the same spatial position, but at the two different times. Obviously, this simplified condition is highly improbable to be verified but, to clarify the basic concepts, let us first refer to it. Therefore, we introduce a deformation component on the measured phase difference and firstly suppose that the $\mathrm{sinc}(\cdot)$ functions could be substituted with the corresponding Dirac ones. By referring to the geometry depicted in Figure 1.18, we will be able to compute the phase difference

$$\Delta\Phi^{def} = \frac{4\pi}{\lambda}(r_2 - r_1) \approx \frac{4\pi}{\lambda} d_{LOS} = \frac{4\pi}{\lambda} d \sin(\vartheta' - \alpha_D) \tag{65}$$

In this way, the equation (65) will allow measuring the displacement component that is parallel to the look angle direction (usually referred to as Line Of Sight (LOS) displacement). In this ideal configuration, the D-InSAR technique gets an unambiguously measurement of the LOS displacement of the order of fractions of wavelength: indeed, a differential phase change of 2π is now associated to a LOS displacement of $\lambda/2$. As an example, because for coherent differential interferograms the error on the estimate is

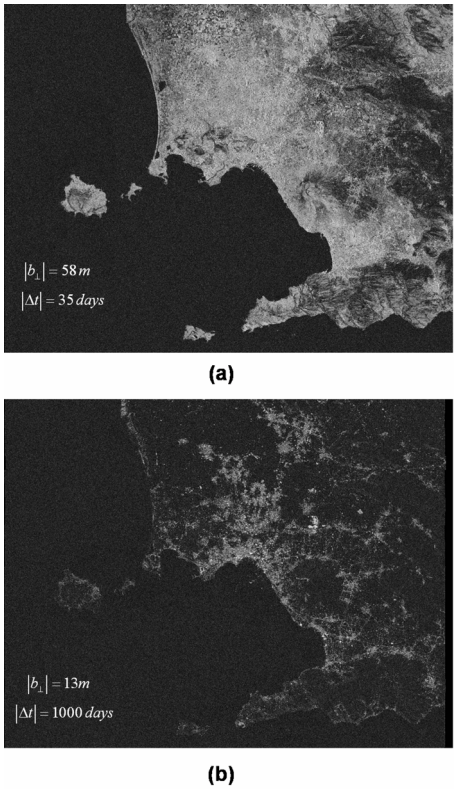

Figure 1. 17 Coherence maps relevant to two distinctive data pairs involving ERS images acquired by ascending orbits, where (a) refers to a small baseline and a small temporal separation and (b) refers to a large interval span interferogram (that is now temporal decorrelated, in spite of a very small spatial baseline separation) .

of a fraction of π and the wavelength is of the order of some centimeters (for the ERS-1/2 case 5.6 cm), we will have

$$\sigma_{\Delta\Phi^{def}} \approx \frac{\pi}{6} \Rightarrow \sigma_{d\_LOS} \approx \frac{\lambda}{4\pi}\frac{\pi}{6} = \frac{\lambda}{24} \tag{66}$$

Hence, it is clear that a displacement in line of sight of the order of some millimeters can be well appreciated.

When a no zero perpendicular baseline between the orbits are considered, additional topographic fringes occurs. In this case, by referring to Figure 1.19, the phase difference will be

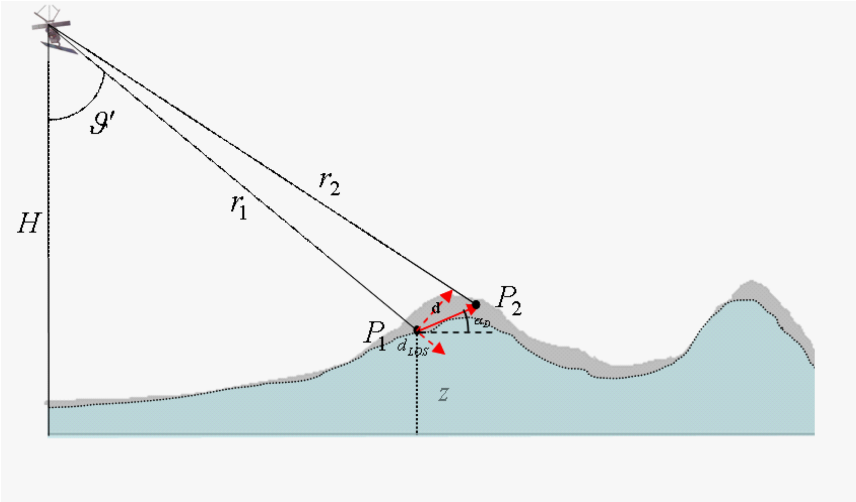

Figure 1. 18 The simplified interferometric geometry where the master and slave orbital positions are considered to be identical, thus allowing immediately individuating the deformation component. P_1 represents the position of the given target on the ground viewed prior the deformation has occurred, while P_2 refers to the position of the same target after the deformation episode (the magnitude of the deformation has been intentionally exaggerated to better show the geometry of the system).

$$\Delta\Phi = \frac{4\pi}{\lambda}(r_2 - r_1) = \frac{4\pi}{\lambda}(\tilde{r} - r_1) + \frac{4\pi}{\lambda}(r_2 - \tilde{r}) = \\ = \Delta\Phi^{flat} + \Delta\Phi^{tpg} + \Delta\Phi^{def} \tag{67}$$

The topographic phase term is not of interest with regard to the surface displacement mapping. For this reason, in order to limit its influence, equation (67) would suggest the use of small perpendicular baselines, only. The discrimination between the topographic and the displacement phase terms, respectively, must be carried out. There are several approaches to measure the topographic components, yielding a differential interferogram in which the signature of surface deformation can be seen. Such an interferogram contains only the fringe patterns caused by deformation and possible decorrelation source. A possible solution, usually referred to a three-pass method, is to consider a second interferogram, generated with two images taken over a time interval during which no significant deformation

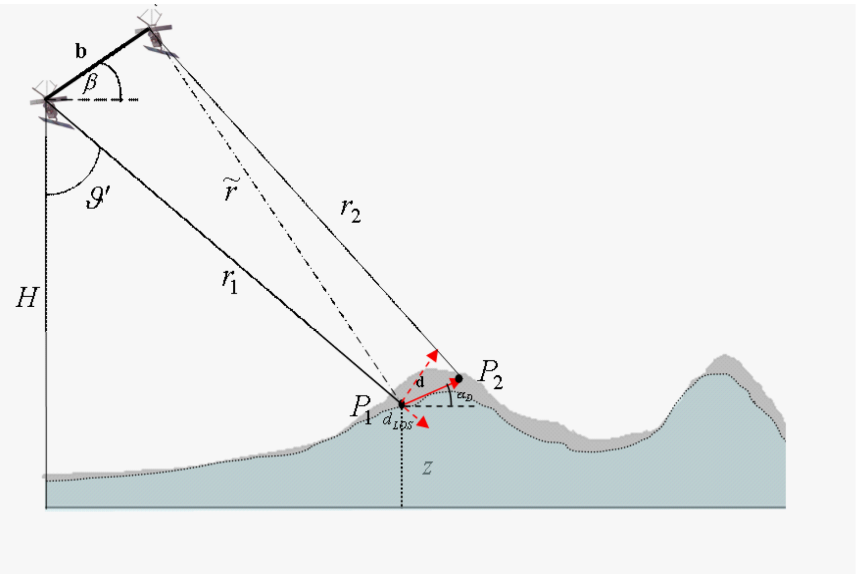

Figure 1. 19 The interferometric geometry where the slant range distances responsible for the topographic and the deformation signal, respectively are represented.

had occurred (tandem) from the one of interest. Moreover, let us suppose the pairs have the same master image, so that no resampling is necessary.

Since the two interferograms can be expressed as follows

$$\begin{aligned}\Delta\Phi_f &= \Delta\Phi_f^{flat}\left(b_{\perp f}\right)+\Delta\Phi^{def}-\frac{4\pi}{\lambda}\frac{b_{\perp f}}{r'\sin\vartheta'}z \\ \Delta\Phi_{TPG} &= \Delta\Phi_{TPG}^{flat}\left(b_{\perp TPG}\right)-\frac{4\pi}{\lambda}\frac{b_{\perp TPG}}{r'\sin\vartheta'}z\end{aligned} \tag{68}$$

it is trivial to verify that

$$\Delta\Phi^{defo}=\left[\Delta\Phi_f-\Delta\Phi_f^{flat}\left(b_{\perp f}\right)\right]-p\left[\Delta\Phi_{tpg}-\Delta\Phi_{tpg}^{flat}\left(b_{\perp topo}\right)\right] \tag{69}$$

where $p=b_{\perp f}/b_{\perp TPG}$ and the quantities with the "TPG" pedix are relevant to the topography-related interferogram while the remainders are relevant to the topography-deformation one. Hence, the differential interferogram depends on the baseline of both pairs and, because the baselines change a little through the image, the phase may change too.

The topographic contribution in the equation (67) can be otherwise calculated through an external, conventional DEM (two-pass differential interferometry). To do this, the DEM has to be transformed in the azimuth-range geometry, scaled with respect to the baseline of the interferogram and the resulting topographic pattern have to be finally converted from length to phase units (see chapter two for a more detailed discussion on this topic).

Whatever method has been applied, the differential interferogram will contain the deformation component only, but inaccuracies on the knowledge of the actual topographic pattern and/or of the orbital parameters arrange for the interferogram to be affected by residual phase terms that may corrupt the deformation measurement accuracy.

1.4.1 Main Limitations of the D-InSAR technique

This sub-section will address the principal limits of the investigated technique. Firstly, we will deal the effects on the deformation measurement of inaccuracies on the knowledge of the orbital parameters and of the scene topography.

To discriminate the two effects, singularly, let us refer to the D-InSAR geometry depicted in Figure 1.19 and firstly suppose the topographic term has been perfectly removed from the original interferograms, but there are uncertainties in the knowledge of the actual perpendicular baseline value. Equation (42) suggests that the resulting differential interferogram will be affected by a residual orbit plane

$$\delta\phi_{residual} = \frac{4\pi}{\lambda}\frac{r' - r_0}{r'\tan\vartheta'}db_{\perp} \tag{70}$$

where, for sake of simplicity, the local slope of the terrain has been considered negligible. Thus

$$\Delta\phi_{D-InSAR} = \Delta\phi_{def} + \delta\phi_{residual} \tag{71}$$

If both orbital inaccuracies and deficiencies on the knowledge of the real topography occurs, the D-InSAR interferogram will contains other spurious terms. To emphasize their contribution, let us suppose the actual perpendicular baseline value is $b_{\perp}$ and the synthesized one is $b_{\perp} + \Delta b_{\perp}$ and there is also a difference between the real height above the reference surface (z) and the corresponding value ($z + \Delta z$) estimated starting from the available DEM. In this manner, the real topographic phase contribution (neglecting the previously analyzed *flat Earth* inaccuracies) will be

$$\Delta\phi_{real}^{tpg} = -\frac{4\pi}{\lambda}\frac{b_{\perp}}{r'\sin\vartheta'}z \tag{72}$$

while the reference one will be

$$\Delta\phi_{synthesized}^{tpg} = -\frac{4\pi}{\lambda}\frac{\left(b_{\perp}+\Delta b_{\perp}\right)}{r'\sin\vartheta'}\left(z+\Delta z\right) \tag{73}$$

so that the residual topographic phase term will be

$$\Delta\phi_{residual}^{D-InSAR} \cong \frac{4\pi}{\lambda}\frac{b_{\perp}}{r'\sin\vartheta'}\Delta z + \frac{4\pi}{\lambda}\frac{z}{r'\sin\vartheta'}\Delta b_{\perp} \tag{74}$$

where the higher order term $4\pi\Delta b_{\perp}\Delta z/\lambda r'\sin\vartheta'$ has been neglected. By taking account of both the previously analyzed effects, a more accurate expression of a differential interferogram is

$$\begin{aligned}\Delta\phi_{D-InSAR(two-pass)} \cong \frac{4\pi}{\lambda}\left(\frac{\left(r'-r_0\right)}{r'\tan\vartheta'}\Delta b_{\perp} + \frac{z}{r'\sin\vartheta'}\Delta b_{\perp} + \frac{b_{\perp}}{r'\sin\vartheta'}\Delta z\right) + \\ + \Delta\phi^{def} + n\end{aligned} \tag{75}$$

Similar considerations could be also made to analyze the 3-pass method (see equation 69), thus retrieving

$$\begin{aligned}\Delta\phi_{D-InSAR(three-pass)} \cong \frac{4\pi}{\lambda}\left(\frac{r'-r_0}{r'\tan\vartheta'} + \frac{z}{r'\sin\vartheta'}\right)\left(\Delta b_{\perp} - p\Delta b_{\perp topo}\right) + \\ + \Delta\phi^{def} + n\end{aligned} \tag{76}$$

Moreover, the deformation term here presented could be corrupted also by atmospheric artifacts. Therefore, if the two passages of the radar sensor over the illuminated area, the weather condition is changed, the time delays of the corresponding radar echoes will also depend on the different electromagnetic propagation velocities.

It means, for example, that if we refer to the configuration depicted in Figure 1.20, the interferometric phase difference (see equation (67)) would be

$$\Delta\Phi = \frac{4\pi}{\lambda_0}\left(\tilde{r}-r_1\right) + \frac{4\pi}{\lambda_0}\left(r_2-\tilde{r}\right) \tag{77}$$

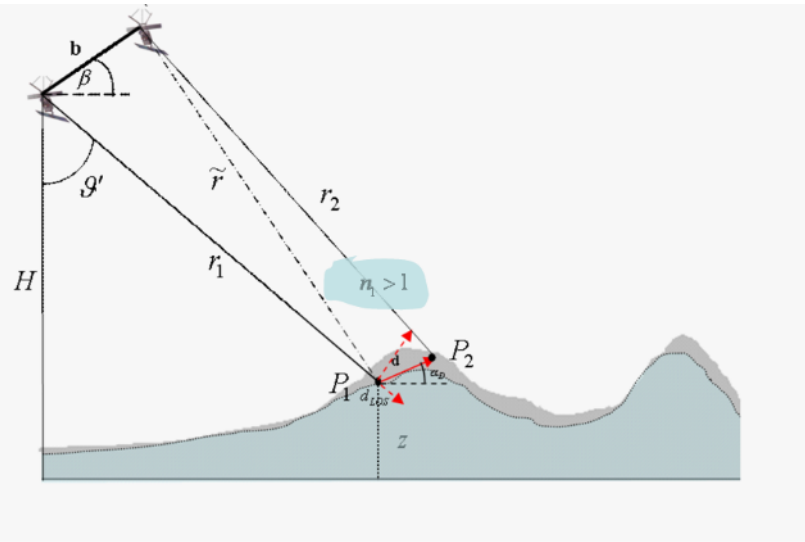

Figure 1. 20 The used interferometric geometry (the same of figure 1.19) where has been also introduced the effect of a possible inhomogeneities of the atmospheric index refraction, responsible of an incorrect estimation of the deformation signal.

thus implying the phase difference expression will be

$$\Delta\Phi_{D-InSAR} = \Delta\Phi^{res\_orbit} + \Delta\Phi^{res\_tpg} + \Delta\Phi^{deform} + \Delta\Phi^{atm} + n \tag{78}$$

where $\Delta\Phi^{atm}(\cdot)$ accounts for the mentioned artifacts. The atmospheric influence (i.e. delay) depends not only on the weather conditions, but it also considerably depends on the range, i.e. on the look angle. Indeed, for an increasing look angle, the path of the ray through the atmosphere gets longer. Also, the atmospheric delay depends strongly on topography, which should be significant in mountain areas. Moreover, as explained in chapter two, the atmospheric phase screen (APS) can be properly filtered out using a convenient spatial-temporal procedure.

By summarizing, if we refer to the twp-pass method, a differential interferogram contains the following signals

- Orbit errors residual fringes $\Delta\Phi^{res\_orbit} \cong \frac{4\pi}{\lambda}\left(\frac{r'-r_0}{r'\tan\vartheta'}\Delta b_\perp + \frac{z}{r'\sin\vartheta'}\Delta b_\perp\right)$ due to an inaccurate

knowledge of the orbital positions of the sensors along the analyzed area;

- Residual topographic signal $\Delta\Phi^{res\_tpg} \cong \frac{4\pi}{\lambda}\left(\frac{b_{\perp}}{r'\sin\vartheta'}\Delta z\right)$ due to the error in the knowledge of the scene topography and/or to an incorrect resampling of the used DEM in the SAR coordinates;
- Deformation signal $\Delta\Phi^{deform}(\cdot)$ corresponding to the displacement occurred between the two flights;
- Atmospheric disturbances $\Delta\Phi^{atm}(\cdot)$ corresponding to a time delay of the radar echoes caused by a different refraction index of the atmosphere itself;
- Additive noise contributions.

Another source of mis-interpretation about the deformation is intrinsic to the technique itself and it is due to the fact that the useful information are present in phase terms, which are known only on the restricted $[-\pi,\pi[$ interval. For this reason, a fundamental non linear operation, allowing us to reconstruct the full phase differences, is requested. This operation, usually referred to as *Phase Unwrapping (PhU)*, represents a crucial point in this context.

Obviously, phase unwrapping errors are integer multiples of 2π but it can propagate within the process of the data inversion and to significantly affect the deformation measurements.

The chapter three will deal on this task by also introducing a novel approach.

1.5 Summary

In this chapter, the basic theory of the SAR system and their interferometric applications have been introduced. In particular, we focused on the application of the SAR technology to the monitoring of the surface displacements, thus emphasizing the role played by possible artifacts, due to several and independent mechanisms, on the achievable measure of the occurred deformation.

APPENDIX A : SAR FOCUSING OUTLINE

In this appendix the evaluation of equation (15) will be addressed.

$$\hat{\gamma}(x',r') = \iint \gamma(x,r)\exp\left(-j\frac{4\pi}{\lambda}r\right)\operatorname{sinc}\left[\frac{\pi}{\Delta r}(r'-r)\right]\cdot \\ \cdot\operatorname{sinc}\left[\frac{\pi}{\Delta x}(x'-x)\right]\exp\left[j\xi_{dopp}(x'-x)\right]dxdr \tag{A1}$$

As stated before, the focusing procedure requires a proper filtering operation on the received raw data, which can be easily performed in the spatial frequency domain.

For this purpose, the SAR transfer function must be firstly evaluated

$$G(\xi,\eta,r) = \iint g(x'-x,r'-r,r)\exp\left[-j\xi(x'-x)-j\eta(r'-r)\right]dx'\,dr' \tag{A2}$$

where (ξ,η) are the corresponding transformed variables, accounting for the azimuth and range angular frequencies, respectively, and

$$g(x'\,x,r'-r,r) = \exp\left[-j\frac{4\pi}{\lambda}\Delta R + j\frac{2\alpha}{c^2}(r'-r-\Delta R)^2\right]\cdot \\ \cdot rect\left[\frac{r'-r-\Delta R}{\frac{c\tau}{2}}\right]w^2\left[\frac{x'-x+r\tan\phi}{X}\right] \tag{A3}$$

is the SAR impulse response.

Letting

$$q = \frac{r'-r-\Delta R}{c\tau/2};$$

$$p = \frac{x'-x}{X}$$

the integral expression (A2) can be rearranged as follows

$$G(\xi,\eta,r)=\left[\int rect(q)e^{j\frac{\alpha\tau^2}{2}q^2-j\eta q\frac{c\tau}{2}}dq\right]\cdot \left[\int w^2\left(p+\frac{r\tan\phi}{X}\right)e^{-j\frac{4\pi}{\lambda}\Delta R(p)-j\xi Xp-j\eta\Delta R(p)}dp\right] \tag{A4}$$

Solution of the first integral

$$\int rect[q]\exp\left[j\left(\frac{\alpha\tau^2}{2}q^2-\eta\frac{c\tau}{2}q\right)\right]dq \tag{A5}$$

is now addressed. We start from the analysis of the integral phase argument

$$\frac{\alpha\tau^2}{2}q^2\approx\pi\Delta f\tau q^2 \tag{A6}$$

and we observe that, in all SAR system, we have $\Delta f\tau=\alpha\tau^2/2\pi>>1$ (for ERS sensors, the parameters of which are collected in Table 1.1, we have $\Delta f\tau\approx 570$). The demonstrated inequality guarantees us for the presence of a fast-varying phase term in (A6) and allows applying, for the integral evaluation, the stationary phase method [31]. In particular, it is easy to verify that the stationary phase point, whose corresponds to a zero value of the first derivative of the phase term, is given by

$$q_s=\frac{\eta c}{2\alpha\tau} \tag{A7}$$

Accordingly, except for a nonessential, additional amplitude term, equation (A5) can be asymptotically evaluated as follows

$$\int rect[q]\exp\left[j\left(\frac{\alpha\tau^2}{2}q^2-\eta q\frac{c\tau}{2}\right)\right]dq\approx rect[q_s]e^{j\left(\frac{\alpha\tau^2}{2}q_s^2-\eta q_s\frac{c\tau}{2}\right)}= =rect\left[\frac{\eta c}{2\alpha\tau}\right]\exp\left[-j\frac{\eta^2c^2}{8\alpha}\right] \tag{A8}$$

Solution of the second integral

$$\int w^2\left[p+\frac{r\tan\phi}{X}\right]\exp\left[-j\Delta R(p)\left(\frac{4\pi}{\lambda}+\eta\right)-j\xi pX\right]dp \tag{A9}$$

is subsequently addressed. Also in this case, we firstly refer to the corresponding phase term, which has the following expression

$$\Psi(p)=-\Delta R(p)\frac{4\pi}{\lambda}\left(1+\eta\frac{\lambda}{4\pi}\right)-\xi pX \tag{A10}$$

Moreover, according to the equation (A8), only a limited range of values for η must be considered, hence:

$$\left|\frac{\eta\lambda}{4\pi}\right|\le\frac{\lambda}{4\pi}\eta_{MAX}=\frac{\lambda}{4\pi}\frac{\alpha\tau}{c}=\frac{\Delta f}{2f}<<1 \tag{A11}$$

where the last inequality holds for all SAR systems. Accordingly, the equation (A10) can be expressed as follows

$$\Psi(p)\approx\frac{4\pi}{\lambda}\frac{1}{2r}X^2p^2=2\pi\frac{X}{L_a\cos^2\phi}p^2 \tag{A12}$$

and, because in all SAR systems we have $2X/L_a>>1$,. we may also apply for the evaluation of the integral the stationary phase method. Hence, we evaluate the first derivative of the phase term (A10)

$$\frac{d}{dp}\left(-\Delta R(p)\left(\frac{4\pi}{\lambda}+\eta\right)-X\xi p\right)=-\xi X-\left(\frac{4\pi}{\lambda}+\eta\right)\frac{d}{dp}\Delta R(p) \tag{A13}$$

thus obtaining as result the following stationary phase point expression

$$p_s=\frac{rX}{\cos^3\phi}\left[\sin\phi-\frac{\xi}{\eta+\frac{4\pi}{\lambda}}\right]-\frac{r\tan\phi}{X} \tag{A14}$$

After trivial calculations, substituting (A14) in (A9), we will finally retrieve the required solution of the integral

$$\int w^2\left[p+\frac{r\tan\phi}{X}\right]\exp\left[j\Psi(p)\right]dp \cong rect\left[p_s+\frac{r\tan\phi}{X}\right]\exp\left[j\Psi(p_s)\right]\cong$$
$$= rect\left[\frac{\xi-\xi_{dopp}}{\frac{4\pi}{L_a}}\right]\exp\left[j\chi\right] \tag{A15}$$

where:

- $\xi_{dopp}=\frac{4\pi}{\lambda}\left(1+\eta\frac{\lambda}{4\pi}\right)\sin\phi\approx\frac{4\pi}{\lambda}\sin\phi$ is the azimuth center angular frequency value, which, properly converted in azimuth frequency (Hz) leads to the expression of the so-called Doppler centroid frequency $f_{dopp}\approx\frac{2v}{\lambda}\sin\phi$;
- the azimuth antenna pattern $w^2(\cdot)$ has been substituted with a $rect(\cdot)$ function, thus referring to a simplified uniform illumination case;
- $\chi=\xi r\tan\phi-\frac{1-\cos\phi}{\cos\phi}\left(\eta+\frac{4\pi}{\lambda}\right)r+\frac{\left(\xi-\xi_{dopp}\right)^2}{2\cos^3\phi\left(\eta+\frac{4\pi}{\lambda}\right)}$ is the azimuth counterpart of the SAR transfer function, which must be subsequently compensated in order to retrieve the focused SAR image.

Therefore, the overall expression of the SAR transfer function will be

$$G(\xi,\eta,r)\cong rect\left[\frac{\eta c}{2\alpha\tau}\right]rect\left[\frac{\xi-\xi_{dopp}}{\frac{4\pi}{L_a}}\right]\exp\left[j\left(\chi-\frac{\eta^2c^2}{8\alpha}\right)\right] \tag{A16}$$

Some considerations on the SAR transfer function are now in order.

First of all, we observe that $G(\cdot)$ is a band limited function, where $\Omega_{range}=2\alpha\tau/c$ and $\Omega_{azimuth}=4\pi/L_a$ are the range and the azimuth spatial bandwidth (rad/m), respectively. However, it would be preferable to refer to the corresponding temporal bandwidth [Hz] expression, which can be obtained through suitable conversions. In particular, the azimuth bandwidth

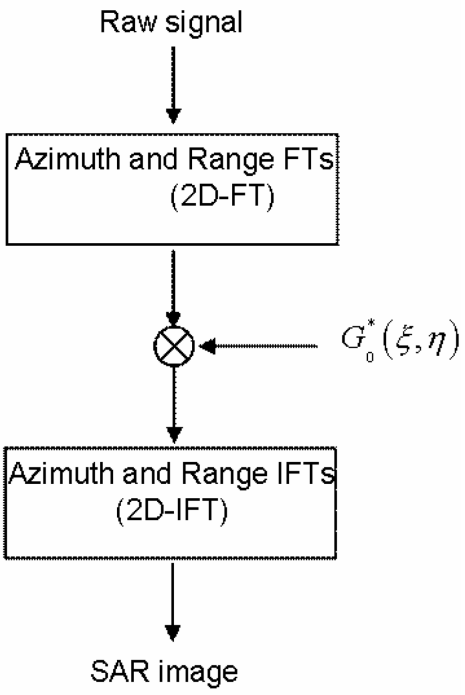

Figure A. 1 Narrow focus SAR processing block diagram.

is obtained via the multiplication of the $\Omega_{azimuth}$ term by the converting factor $v_s/2\pi$ (v_s being the sensor velocity) thus obtaining $2v_s/L_a$, often interpreted as Doppler bandwidth. In turn, the range spatial bandwidth will be converted in Hz via the multiplication by the converting factor $c/4\pi$ thus obviously leading to the chirp bandwidth expression.

At this stage the raw-data spectrum may be calculated

$$\begin{aligned} H(\xi,\eta) &= \iint\left[\iint \tilde{\gamma}(x,r)\, g(x'-x,r'-r,r)\, dxdr\right] e^{-j(\xi x'+\eta r')} dx'dr' = \\ &= \iint \tilde{\gamma}(x',r')\, G(\xi,\eta,r) \exp\left[-j(\xi x'+\eta r')\right] dx'dr' \end{aligned} \tag{A17}$$

Since the SAR transfer function has been previously evaluated, we can address the problem to compensate its phase terms, thus leading to the focused image expression. The simplest and most efficient processing scheme is based on the utilization of the following approximation

$$G(\xi,\eta,r) \approx G(\xi,\eta,r_0) = G_0(\xi,\eta) \tag{A18}$$

where r_0 is the range coordinate of the scene center. This condition allows us to obtain the following, approximated expression of the raw data spectrum

$$H(\xi,\eta) = \tilde{\Gamma}(\xi,\eta) \cdot G_0(\xi,\eta) \tag{A19}$$

thus suggesting to implement the following space invariant filtering operation

$$\hat{\Gamma}(\xi,\eta) = H(\xi,\eta) \cdot G_0^*(\xi,\eta) = \tilde{\Gamma}(\xi,\eta) rect\left[\frac{\eta c}{2\alpha\tau}\right] rect\left[\frac{\xi - \xi_{dopp}}{\frac{4\pi}{L_a}}\right] \tag{A20}$$

carried out in the two dimensional Fourier Domain. The spectral multiplication of the equation (A20) allows an efficient focusing of the SAR image following the scheme depicted in Figure A1. Note that the operation implemented by such a processing scheme can be carried out directly in the time domain, since it is equivalent to a deconvolution step applied to $h(x',r')$. However, the system impulse response generally extends for several hundreds points in both azimuth and range directions; typical dimensions of the raw data set are very large too (thousands complex samples for each direction). Hence, it is convenient to carry out the deconvolution operation in the Fourier Domain due to the availability of Fast Fourier Transform (FFT) codes. The key point of such a procedure is represented by the knowledge of the transfer function obtained in each section (see eq (A18)) by assuming r=r0. For this reason this processing procedure is known as narrow focus code, because only the central part of the scene, r=r0, is perfectly focused.

Finally, the expression representing a SAR focused SAR image, can be obtained by evaluating the inverse Fourier Transform of the equation (A20), that is

$$\begin{aligned} \hat{\gamma}(x',r') &= \iint \tilde{\Gamma}(\xi,\eta) rect\left[\frac{\eta c}{2\alpha\tau}\right] rect\left[\frac{\xi - \xi_{dopp}}{\frac{4\pi}{L}}\right] e^{j(\xi r' + \eta r')} d\xi d\eta = \\ &= \tilde{\gamma}(x',r') \otimes \left[\operatorname{sinc}\left(\frac{\pi}{\Delta r} r'\right) \operatorname{sinc}\left(\frac{\pi}{\Delta x} x'\right) \exp\left(j\xi_{dopp} x'\right)\right] \end{aligned} \tag{A21}$$

where $\Delta r = c/2\Delta f$ and $\Delta x = L_a/2$ are the theoretical range and azimuth resolutions, respectively.

We finally stress that the achieved focused SAR image has been represented in the output zero-doppler geometry (i.e., we imposed the squinted output geometry to be the same of the corresponding non squinted case) and, for this reason, it is usually referred to as the zero-doppler focused SAR image expression. Should the two linear phase terms in ξ and η, respectively, presented in equation (A16) be non compensated, we would lead to the following non zero-doppler focused SAR image expression:

$$\hat{\gamma}(x',r') = \tilde{\gamma}(x',r') \otimes$$
$$\otimes\left[\operatorname{sinc}\left[\frac{\pi}{\Delta \mathrm{r}}\left(r' - \frac{r}{\cos\phi}\right)\right]\operatorname{sinc}\left[\frac{\pi}{\Delta \mathrm{x}}\left(x' + r\tan\phi\right)\right]\exp\left[j\xi_{dopp}\left(x' + r\tan\phi\right)\right]\right] \quad \text{(A22)}$$

APPENDIX B : COHERENCE CALCULATION

We proceed from the expression of the two SAR image

$$\hat{\gamma}_1(x',r') = \iint \gamma_1(x,r)\exp\left(-j\frac{4\pi}{\lambda}r\right)\operatorname{sinc}\left[\frac{\pi}{\Delta r}(r'-r)\right]\cdot$$
$$\cdot\operatorname{sinc}\left[\frac{\pi}{\Delta x}(x'-x)\right]\exp\left[j\xi_{d1}(x'-x)\right]dxdr$$

$$\hat{\gamma}_2(x'+u'_x, r'+u'_r) = \iint \gamma_2(x,r)\exp\left(-j\frac{4\pi}{\lambda}(r+\delta r)\right)\cdot \tag{B1}$$
$$\cdot\operatorname{sinc}\left[\frac{\pi}{\Delta r}(r'-r+u'_r-\delta r)\right]\cdot\operatorname{sinc}\left[\frac{\pi}{\Delta x}(x'-x+u'_x-\delta x')\right]\cdot$$
$$\cdot\exp\left[j\xi_{d2}(x'-x)\right]dxdr$$

and let us evaluate the complex interferogram expected value, by supposing the reflectivity pattern is represented by a homogeneous, uncorrelated process.

Hence

$$E\left[\gamma(x_1,y_1)\gamma^*(x_2,y_2)\right] = |\gamma|^2\,\delta(x_1-x_2)\,\delta(y_1-y_2) \tag{B2}$$

The cross-correlation factor is essentially a normalized mutual correlation between the two complex SAR images, represented by the relations (B1), and can be written as

$$\chi = \frac{E\left[\gamma_1\gamma_2^*\right]}{\sqrt{E\left[|\gamma_1|^2\right]E\left[|\gamma_2|^2\right]}} \tag{B3}$$

The calculation of the numerator is now in order. For this purpose, we rewrite the expression (B1) by introducing the variable changes

$$p = x'-x$$
$$q = r'-r$$

Hence, we have

$$\hat{\gamma}_1(x',r') = \exp\left(-j\frac{4\pi}{\lambda}r'\right)\iint \gamma_1(x'-p,r'-q)\cdot$$
$$\cdot\exp\left(j\frac{4\pi}{\lambda}q\right)\operatorname{sinc}\left[\frac{\pi}{\Delta r}q\right]\operatorname{sinc}\left[\frac{\pi}{\Delta x}p\right]\exp\left[j\xi_{d1}p\right]dpdq$$

$$\hat{\gamma}_2(x',r') = \exp\left(-j\frac{4\pi}{\lambda}(r'+\delta r')\right)\iint \gamma_2(x'-p,r'-q)\cdot \tag{B4}$$
$$\cdot\exp\left(j\frac{4\pi}{\lambda}(q-\delta r+\delta r')\right)\exp\left(j\frac{4\pi}{\lambda}(q-\delta r+\delta r')\right)\cdot$$
$$\cdot\operatorname{sinc}\left[\frac{\pi}{\Delta r}(q+u'_r-\delta r)\right]\operatorname{sinc}\left[\frac{\pi}{\Delta x}(p+u'_x-\delta x')\right]\exp\left[j\xi_{d2}p\right]dpdq$$

and, consequently

$$E\left[\gamma_1\gamma_2^*\right] = \exp\left(j\frac{4\pi}{\lambda}\delta r'\right)\iint dpdq\exp\left(j\frac{4\pi}{\lambda}(\delta r-\delta r')+(\xi_{d1}-\xi_{d2})p\right)\cdot \tag{B5}$$
$$\cdot\operatorname{sinc}\left[\frac{\pi}{\Delta x}p\right]\operatorname{sin}c\left[\frac{\pi}{\Delta x}(p+u'_x-\delta x')\right]\operatorname{sin}c\left[\frac{\pi}{\Delta r}q\right]\operatorname{sin}c\left[\frac{\pi}{\Delta r}(q+u'_r-\delta r)\right]$$

Equation (47) allows us to express the slant range difference between the cell center and its value within the resolution cell as a function of the local slope of the surface, that is

$$\delta r'-\delta r \approx -\frac{b_\perp}{r'}(r'-r)\frac{1}{\tan(\vartheta'-\bar{\Omega}_t)} = -q\frac{b_\perp}{r'\tan(\vartheta'-\bar{\Omega}_t)} \tag{B6}$$

The previous condition and the assertion that the variation on the slant range affects the phase term, but is not relevant for the integrating amplitude term, lead to rearrange the previous expression in this novel form

$$E\left[\gamma_1\gamma_2^*\right] = \exp\left(j\frac{4\pi}{\lambda}\delta r'\right)\int dq\exp\left(-j\frac{4\pi}{\lambda}\frac{b_\perp}{r'\tan(\vartheta'-\bar{\Omega}_t)}q\right)\operatorname{sinc}^2\left(\frac{\pi}{\Delta r}q\right)\cdot \tag{B7}$$
$$\cdot\int dp\exp(j\Delta\xi_d p)\operatorname{sin}c^2\left(\frac{\pi}{\Delta x}p\right)$$

where the possible mis-registration effects have been neglected. At this stage we can observe that, for example, the second integral can be viewed as the

Fourier transform of the $sinc^2(\cdot)$ function that is equal to the convolution of two rectangular spectra pulse (which is equal to a triangle pulse)

$$\int dp \exp\left(j\Delta\xi_d p\right)\mathrm{sinc}^2\left(\frac{\pi}{\Delta x}p\right) \propto \Lambda\left(\frac{\Delta\xi}{4\pi}L_a\right) \tag{B8}$$

$$\int dq \exp\left(-j\frac{2\pi}{\Delta r}\frac{b_\perp}{b_{\perp c}}q\right)\mathrm{sinc}^2\left(\frac{\pi}{\Delta r}q\right) \propto \Lambda\left(\frac{2\pi}{\Delta r}\frac{b_\perp}{b_{\perp c}}\frac{\Delta r}{2\pi}\right) = \Lambda\left(\frac{b_\perp}{b_{\perp c}}\right) \tag{B9}$$

TABLE 1.1 ERS Parameters

Parameters	**ERS/1-2**
Carrier wavelength (λ)	5.67 cm (C-band)
Transmitted Bandwidth (Δf)	15.5 MHz
pulse duration (τ)	37.1 μs
chirp rate (α)	2.62×10^{12} rad/s^2
PRF	1.678 KHz
antenna dimensions (azimuth/range)	10m x 1m
altitude	785 km
azimuth footprint (X)	100 km

Chapter 2

Multi-temporal D-InSAR Techniques

Differential Interferometry is a relatively new technique for the detection of the Earth surface deformation and its basic principles have been discussed in the previous chapter.

The D-InSAR methodology has been firstly applied to investigate single deformation events [29,32,33]. However, more recently, these approaches have been also used to analyze the temporal evolution of the detected displacements through the generation of proper deformation time series, which have been obtained starting from a set of multiple differential interferograms. The interest on the development of these methodologies is testified by several algorithms, which have been already presented or that are under development [34-38]. These approaches requires that complex processing chains, with a given computational cost, are considered. In the following, we will give an overview of the involved procedures, thus emphasizing the role played by the different data inversion algorithms up to now proposed, with a particular interest on the Small Baseline Subset (SBAS) approach [39].

2.1 Processing Chain

With regard to a set of N+1 complex-valued SAR images relevant to the same illuminated area, a multi-temporal D-InSAR processing chain can be properly decomposed, as shown in Figure 2.1, as follows

1. Evaluation of the orbital parameters associated to each SAR acquisition, subsequently used within the estimation of the orbital spatial separation (i.e. the spatial baseline value);
2. Generation of a set of single-look SAR images from the available raw data files;
3. Selection of the optimal interferometric data pair distribution;
4. Co-registration of each SAR image with respect to a properly identified "*reference master image*" (with respect to which the baseline values are evaluated);

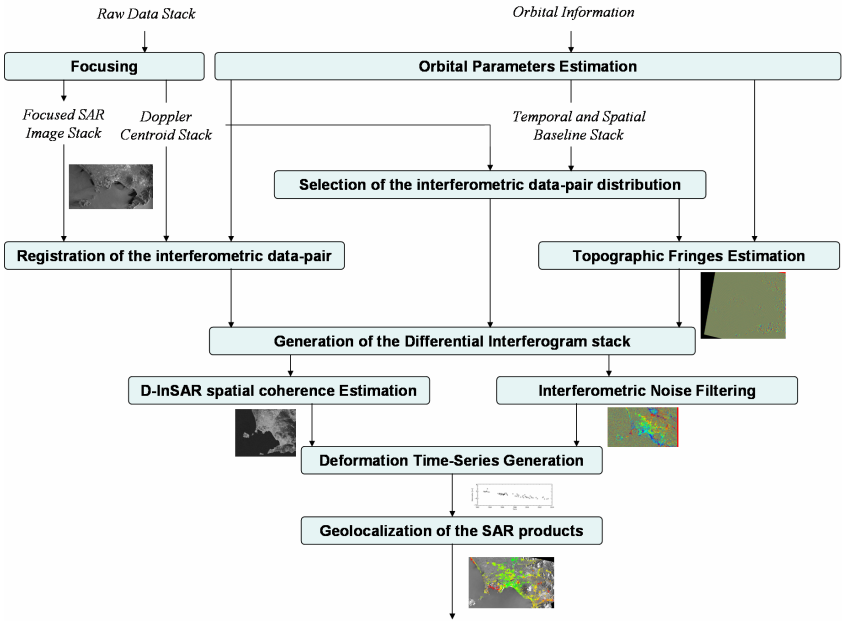

Figure 2. 1 Deformation time-series generation processing chain.

5. Generation, for each single interferometric data pair, of a set of synthetic fringes, accounting of the phase difference due to the scene topography, only;
6. Generation of the corresponding differential interferograms, obtained via the subtraction of the previously computed synthetic fringes from the *"master-slave"* phase difference of each interferometric pair;
7. Noise-filtering of the generated D-InSAR fringes;
8. Generation, interferogram by interferogram, of the spatial coherence maps, representing an estimate of the noise level affecting the computed D-InSAR interferograms;
9. Inversion of the sequence of D-InSAR interferograms, leading to the reconstruction of the surface deformation evolution affecting the investigated area. At the same time, an estimate of the possible residual topographic components and the atmospheric contributions is also accomplished;
10. Geolocalization of the image points and projection onto a universal cartographic grid.

2.2 Orbital Parameters Estimation and SAR Focusing Step

Although the focusing procedure has been already analyzed in the previous chapter, it is important to clarify how different focused SAR images can be effectively used within the deformation time-series procedure. In this context, a perfect knowledge of the true position of the SAR sensor (that is of the orbital parameters) along its flight path is necessary. This task is accomplished via the representation of the generic orbit through a set of state vectors (expressed via polynomial functions), typically supplied in conjunction with each raw data file (for example, this is the case for the ERS data). Nevertheless (at least for the ERS1/2 radar sensors), precise satellite orbit state vectors are available at a global scale and are typically collected into data-bases (this is, for example, the case for the precise orbits provided by the University of Delft) [40]. Obviously, the state vector errors will correspond to an inaccurate estimation of the actual spatial position of the radar sensor, thus implying a subsequent wrong estimation of the synthetic fringes and/or the presence of uncompensated *flat-Earth* terms on the generated differential interferograms (see chapter one). With regard to the general characteristics of the orbits relevant to the ERS sensors, in particular, we stress that the radar sensor flight at an altitude of about 780 Km with an inclination angle of about 98°, an orbital period of 100 minutes and a repetition cycle of about 35 days. Radar sensor, while moves in the approximately South-North direction, observes the same portion of the Earth twice (corresponding to the ascending and descending orbits, respectively, as represented in Figure 2.2) thus helping us on the resolution of the layover problem and, above all, allowing us to discriminate (as clarified in section 2.9) the vertical and the East-West deformation components, respectively.

By exploiting the orbital information, the baseline vectors (evaluated with respect to the "*reference master image*") can be firstly estimated. Obviously, different azimuth lines will have different baseline values, although (at this stage) the variation rate along the whole scene can be considered irrelevant. The baseline vector is a three-dimensional one, so that it can be projected onto a properly selected reference system. Besides, as underlined in the chapter one, it is convenient to look at its projection along the plane orthogonal to the azimuth line (which must be in turn projected along the slant range direction and the direction orthogonal to the range and azimuth direction, at the same time).

The achievable D-InSAR results are above all dependent on the perpendicular baseline vector values (see chapter one), so that each SAR image can be profitably represented in the Time/Perpendicular Baseline plane (see Figure 2.3) through a set of corresponding points. Moreover, each

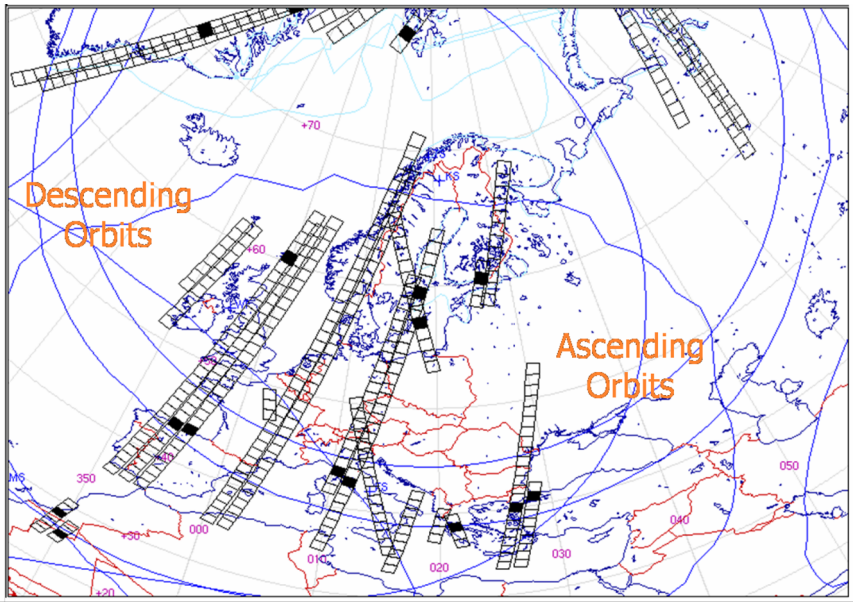

Figure 2. 2 An example of the European acquisition plan of the ERS1/2 sensors .

focused SAR image can be also characterized by the estimated doppler centroid value (see chapter one) which represents the central frequency of the azimuth spectrum (that is particularly important to argue on the decorrelation effects affecting the used interferograms). As explained in the previous chapter, the azimuth central frequency is related to the squint angle via the following relation

$$f_{dopp} = \frac{2v_s}{\lambda} \sin \varphi_s \tag{1}$$

wherein v_s is the platform velocity, λ is the operational wavelength and φ_s is the squint angle. In presence of significant sensor stability problems (as the case for the ERS2 sensor after 2000 [41]), the squint angle can be higher than one expect with reference to the Pulse Repetition Frequency (PRF), thus implying an ambiguity on the evaluation of the actual doppler centroid value. As matter of fact, the azimuth signal is automatically sampled at the PRF frequency, so that the azimuth spectrum is composed by several replica. Therefore, the evaluation of the amplitude peak spectrum does not automatically corresponds to the effective doppler centroid value but the correct replica index must be also known. In literature, several approaches to solve this problem have been formerly proposed [42-43]. In this context, it is

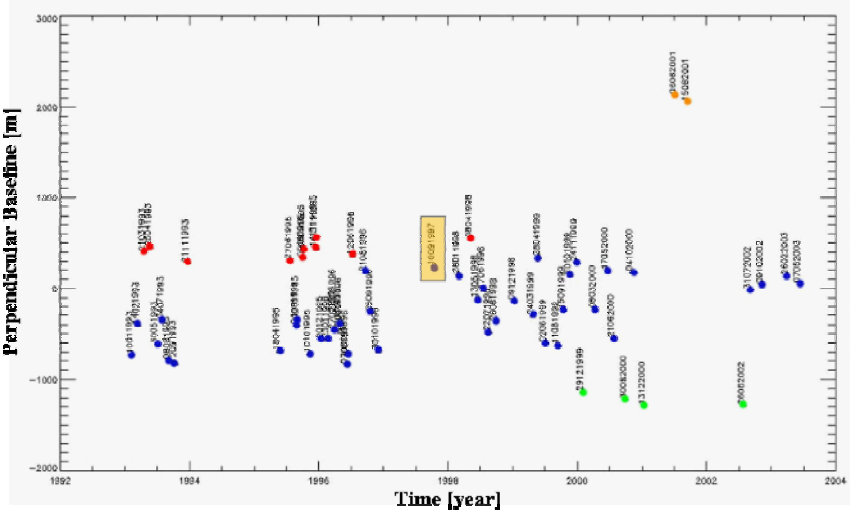

Figure 2. 3 An example of the SAR images distribution onto the Temporal/Perpendicular baseline plane. The representation in different colors help us to directly individuate the images belong to the same interferometric subset (the point corresponding to the reference master image has been highlighted with an orange-box).

sufficient to remark that an incorrect estimation of the replica index of a SAR image could also suggest us to generate highly uncorrelated differential interferograms (because in these cases the azimuth separation would be greater than the bandwidth itself).

Basically, the evaluation process of the optimal D-InSAR data-pair distribution is guided to the constraint that the expectable decorrelation effects are as limited as possible: this task will be easily achieved by imposing that both the baseline separation of the SAR acquisitions and the differences on their doppler centroid values are small enough. For this reason, it could be convenient to represent each SAR image in a three dimensional space, whose axis are the temporal baseline, the spatial baseline and the doppler centroid frequency, respectively. On the other hand, we can observe that ERS SAR images with replica indexes not equal to zero are essentially related to the time period after the gyroscope problems of the 2002 and, for this reason, large variations on the doppler centroid are essentially limited to this period.

These observations suggest us that the SAR images can be effectively represented onto the projected Temporal/Perpendicular baseline plane.

The representation of the SAR acquisitions on the Temporal/Perpendicular baseline plane allows us to argue on the selection

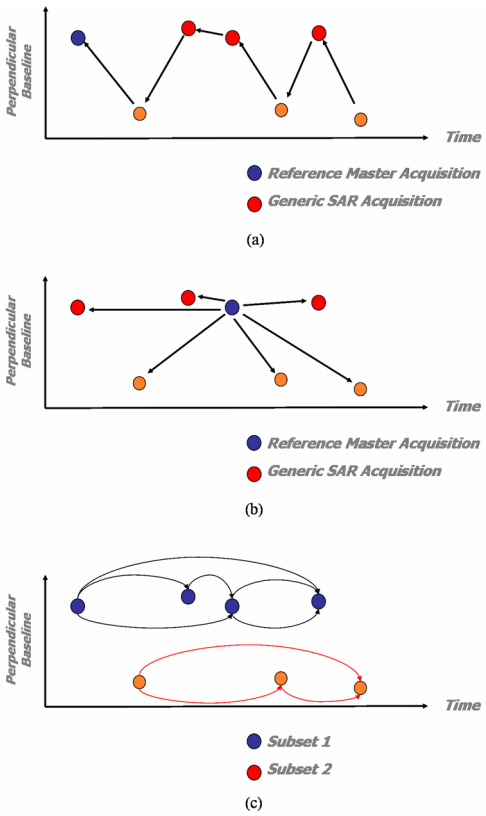

Figure 2. 4 Pictorial representation of the possible interferometric distribution: (a) represents the case where a set of consecutive interferometric pairs is considered, characterized by a single subset; (b) represents the case relevant to the choice of interferograms pair with the same master image (we have, also in this case, a single subset); (c) is related to the case where the interferometric distribution is chosen so as several subset of data are present and this happens, for example, when only a set of low-decorrelated interferograms is considered.

criterion of the "*reference master*" image. In fact, especially for the registration requirements, it is useful to select as reference a SAR acquisition with respect to which the evaluated baseline values are smaller as possible. This task can be easily achieved by referring, for example, to the SAR acquisition located in correspondence to the baricentrical position of the whole distribution onto the Temporal/Perpendicular baseline plane, as represented in Figure 2.3.

2.3 Interferometric Strategies

In order to introduce the key ideas of the available inversion algorithms, it can be convenient to look at the SAR data acquisition distribution in the Temporal/Perpendicular baseline plane, again. Basically, the whole set of possible algorithms is based on the proper selection of the interferometric data pair distribution, which in this plane corresponds to a set of arcs connecting the points associated to the different SAR acquisitions. It is known (see chapter one) that the larger are the perpendicular and/or temporal baselines value, the more significant will be the decorrelation phenomena. Hence, depending on the choice of the optimal interferometric distribution, the different algorithms will be able to extract different and/or additional information.

The easiest of the possible choice would require to generate a set of interferograms between the N consecutives data acquisitions, thus implying a subsequent search for the solution of a determined NxN system (see Figure 2.4) but, consequently, high decorrelated interferograms should be considered, too. Another possibility could require to generate a set of interferograms between each single SAR image and the "*reference master"* one (see Figure 2.4b). Nevertheless, in this case, we can observe that, even if some of the considered interferograms may have a perpendicular baseline value greater than the critical one (and, for this reason, strongly affected by the decorrelation noise), if we would refer to a set of properly chosen point-wise scatterers, the useful information could be also retrieved. This is the key idea of the Permanent Scatterers (PS) technique [35]. The high dispersion of the baseline values and the limited accuracy of the available DEM make impossible the usage of a coherence criterion to select the pixels with good phase quality, since for the largest baselines the topographic components has to be accurately removed from the interferometric phase prior to the coherence computation. Within the PS technique, pixels are selected from the study of its amplitude stability along the whole set of images, which requires a minimum of 30 images and its proper radiometric calibration for a reliable selection, so that the maximum resolution of the SAR images is preserved. With regard to the data inversion approach, a linear model is adjusted to the data, pixel by pixel, to estimate the deformation linear velocity and the DEM error. Finally, for each image, the non linear component of the movement and the atmospheric phase screen (APS) is computed with a combined spatial-temporal filtering [35,44,45]. Another possible solution is represented by the choice of a set of Small Baseline interferograms, only (see Figure 2.4(c)). This approach permits mitigating the noise effects on the interferograms, minimizing the spatial and temporal separation between the orbits. The counterpart of this choice is

represented by the presence of more than one independent subset of acquisitions which have to be subsequently linked each other. This issue represents the core of the SBAS algorithm [39], which will fully described in the following (see section 2.7.4). Basically, the selection of the optimal data pair distribution can be effectively obtained by imposing that each data-pair satisfies the following constraints

$$\begin{aligned} &\left|b_{\perp}\right| < \left|b_{\perp \max}\right| \\ &\left|\Delta t\right| < \left|\Delta t_{\max}\right| \\ &\left|\Delta f_{dopp}\right| < h\frac{PRF}{2} \end{aligned} \tag{2}$$

where h is a selected fraction of the azimuth spectra and, generally, the maxima values are selected depending on the noise level that is considered acceptable. Obviously, in order to limit the computational cost of our solution, it is convenient to select, and subsequently generate, a subset of the whole interferometric data pair distribution that satisfies these constraints, only. To this end, we can impose, for example, that each SAR image is involved in a given, maximum number of differential interferograms.

A different criterion to select the interferometric distribution, aimed to the limitation of the Phase Unwrapping errors, will be also described in chapter three.

2.4 Registration of the SAR images

Once a proper set of interferometric data pairs have been selected, for each pair one might register the relevant master image with respect to the slave one. This procedure, as outlined before, is fundamental to subsequently extract the phase difference relevant to corresponding pixels on the different images.

By referring to a single data pair, the registration procedure [15,46] concerns the compensation of the azimuth and range pixel displacements. In fact, for a generic point in the master image, the SAR coordinates of the same point in the slave image will be given by

$$\begin{aligned} x'_s &= x'_m + \delta x'\left(x', r'\right) \\ r'_s &= r'_m + \delta r'\left(x', r'\right) \end{aligned} \tag{3}$$

wherein (x'_m, r'_m) and (x'_s, r'_s) are the coordinates of the point P in the master and slave geometry, respectively and $(\delta x', \delta r')$ are representative of the difference in the SAR coordinates to be applied to the master ones (with respect to the selected point $P(x', r')$ in a given reference plane) to retrieve the corresponding slave coordinates. The registration process can be therefore defined as the problem of computing the geometric image transformation functions and, subsequently, the problem of re-sampling the second image with respect to the master one, in such a way that each ground point is located at the same position in the two different images. Accuracies of the order of $1/8^{th}$ of the image pixel dimension are usually considered acceptable, although values of about $1/120^{th}$ can be also accomplished. To this end, an estimate of the local rigid patch translation must be, first of all, implemented by moving a selected patch of the slave image with respect to the corresponding master one and by using the following strategies

- The maximization of the image cross-correlation factor, relevant to a patch located at the center of the image;
- The maximization of the spectral extent of the patched complex interferogram.

Basically, in order to improve the registration performances, it can be useful to register the images via a two-step procedure. Therefore, as said before, a common reference master geometry must be chosen and consequently, apart from the registration of each slave image with respect to the master one, it is also needed to register each master data pair with respect to the reference one. Accordingly, even if the absence of mis-registration errors would make irrelevant a second registration step, the overall procedure may be effectively divided in two different steps. For example, the former should provide to register each single SAR image with respect to the reference geometry and the latter to accommodate the remaining, less significant, registration errors, thus improving the global precision and assuring an accuracy at the order of the sub-pixel level.

We finally note that this two-steps procedure can be simplified by also exploiting the viewing geometries relevant to the two SAR acquisitions and these techniques are usually referred to as geometric registration approaches [47].

2.5 Evaluation of the Synthetic Fringes

Once the basic ideas about the differential interferometry have been introduced, we may underline there are several possibilities to extract the

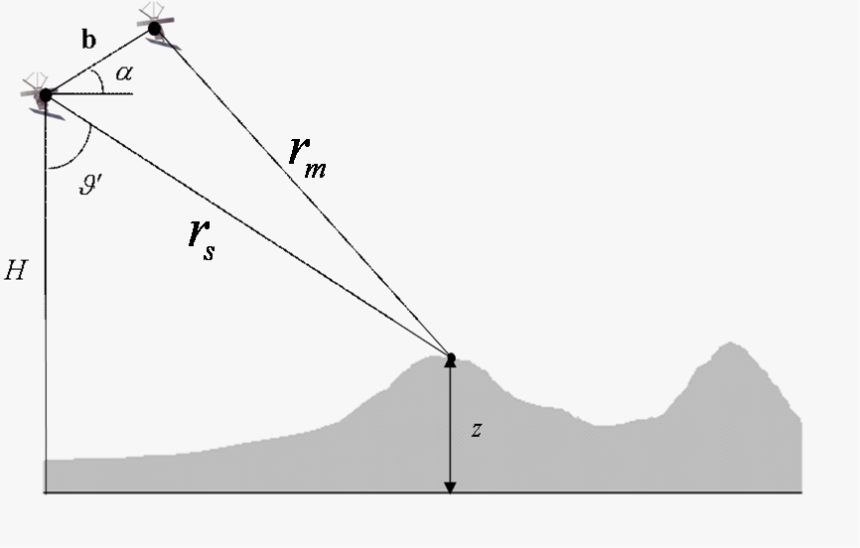

Figure 2. 5 Repeat-Pass acquisition geometry used within stereometric/interferometric applications. SAR sensor observes the same scene from slightly different orbital positions thus leading to the reconstruction of the topography of the scene.

topographic phase components, which have to be subsequently subtracted to the interferometric phase to retrieve the deformation phase pattern.

In this section, in particular, we will refer to the two-pass method which exploits of an external digital elevation model (DEM) of the area to reconstruct the topographic fringes and, the proposed experiments, have been carried out by using the Shuttle Topography Mapping (SRTM) DEMs [48].

This section will address the key steps to synthesize the topographic phase component. The strategy we follow is based on the observation that (see equation 31, chapter 1) the phase associated to the scene topography can be estimated, for each pixel of the registered SAR images, via the measure of the master-slave slant range differences (see Figure 2.5), as follows expressed (see equation 43, chapter 1)

$$\Delta\varphi_{synth} = \frac{4\pi}{\lambda}\left(r_s - r_m\right) \cong \Delta\Phi^{flat} - \frac{4\pi}{\lambda}\frac{b_\perp}{\bar{r}\sin\vartheta'}z \tag{4}$$

wherein $b_\perp$ is the data-pair perpendicular baseline, ϑ' is the look-angle, $\bar{r}$ is the mean slant range distance relevant to the *"reference master"* geometry and $\Delta\Phi^{flat}$ is the corresponding *flat-Earth* term.

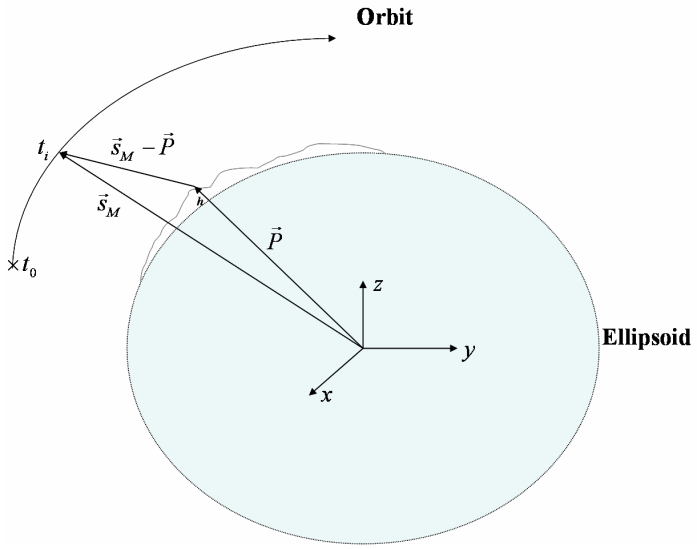

Figure 2. 6 Acquisition geometry of the "reference master" image, represented with respect to a cartesian reference system, where the target of height h (known in reference to a chosen, ellipsoidical surface), illuminated by the radar sensor at the time t_i , is represented by the vector **P**.

Let us firstly estimate the range distances with respect to the targets on the scene and associated to each SAR image. Our information are related to the elevation of the overall points in the available scene DEM, eventually projected onto a conventional cartographic reference system, with respect to a reference ellipsoid.

Basically, the synthesized fringes estimation procedure can be viewed as the cascade of the following steps:

1) Evaluation of the position of the DEM points onto the master SAR geometry, corresponding to a classical inverse-geocoding problem;
2) Estimation, acquisition by acquisition, of the SAR sensor positions along their orbits;
3) Evaluation of the slant range differences, pixel by pixel, for each SAR image;
4) Estimation of the topographic phase term.

The first step is accomplished by using the orbital parameters of the *"reference master"* image, which allows individuating the actual sensor position along its flight path. The procedure starts from the conversion of the available DEM points (typically known onto a cartographic reference

system) in an ellipsoidical, cartesian reference system. In this way, each DEM point will be transformed in a corresponding point $P(x_e, y_e, z_e)$ in the cartesian reference system, which must be associated to a pixel of coordinates $Q \equiv (i, j)$ onto the reference master image geometry. For this purpose, we observe (see Figure 2.6) that the slant range coordinate represents the sensor-to-target distance, as one can estimate by referring to a cartesian reference system, and that the SAR images have been focused at the zero-doppler position (see chapter one).

These observations can be analytically represented by the following system of equations

$$\begin{aligned} &\left|\vec{P} - \vec{s}_M(t_i)\right| = r_M \\ &\vec{s}_M(t_i) \cdot \left[\vec{P} - \vec{s}_M(t_i)\right] = 0 \end{aligned} \tag{5}$$

in the (t_i, r_M) unknowns, wherein $\vec{P}$ is the position vector of the generic target on the local ellipsoid, illuminated by the radar sensor at the instant t_i, while $\vec{s}_M(t_i)$ is the radar position vector. The sensor position, depending on the time acquisition t_i can be, in turn, expressed in the same reference system by using the orbital parameters associated to the reference master image itself, as follows

$$\vec{s}_M = \begin{cases} x_{s_M} = a_0 + a_1(t_i - t_0) + a_2(t_i - t_0)^2 + a_3(t_i - t_0)^3 \\ y_{s_M} = b_0 + b_1(t_i - t_0) + b_2(t_i - t_0)^2 + b_3(t_i - t_0)^3 \\ z_{s_M} = c_0 + c_1(t_i - t_0) + c_2(t_i - t_0)^2 + c_3(t_i - t_0)^3 \end{cases} \tag{6}$$

where the coefficients are related to the orbital parameters and t_0 is the origin of the temporal reference on the orbit. Once the unknowns have been evaluated, the SAR image coordinates of the given DEM point can be estimated by solving these equations

$$\begin{aligned} t_i &= t_0 + \frac{i}{PRF} \\ r_M &= r_0 + \frac{c}{2 f_{samp}} j \end{aligned} \tag{7}$$

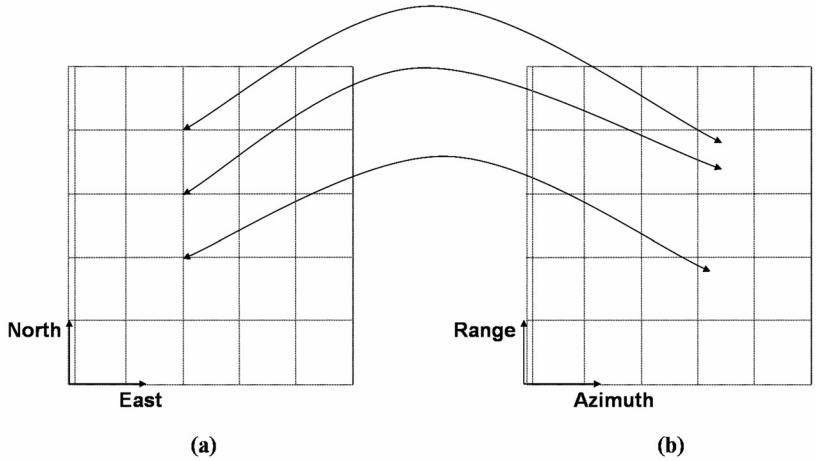

Figure 2. 7 A pictorially representation of the conversion operation of each DEM point (a) onto the SAR reference master image geometry (b). As shown in this figure, the converted points are not necessarily spaced on a regular grid, so that a regridding operation is generally required.

with respect to the (i,j) unknowns, wherein r_0 is the near range distance, c is the speed of the light, PRF the pulse repetition frequency and f_{samp} the range sampling frequency, respectively. In this manner, for each pixel of the available DEM, we must obtain the corresponding position onto the reference SAR geometry. We can farther use these coordinate conversions operations to express each ellipsoidical coordinate of the generic DEM point P onto the SAR reference system. Obviously, the regular cartographic grid (see Figure 2.7) will be deformed in an irregular SAR output grid and, for this reason, a proper regriddind operation onto the converted pixels will be necessary. The regridding operation could be also performed for each different orbital positions but, since a reference geometry has been chosen, it can be more efficient to make one single operation to limit possible errors. In this manner, if we refer to the conversion of the cartesian coordinates of the DEM point, we will have

$$\begin{cases} x_{e\ (i,j)} \\ y_e \\ z_e \end{cases} \rightarrow \begin{cases} X_e(i,j)_{regr} \\ Y_e(i,j) \\ Z_e(i,j) \end{cases} \rightarrow \begin{cases} \tilde{X}_e(i,j) \\ \tilde{Y}_e(i,j) \\ \tilde{Z}_e(i,j) \end{cases} \tag{8}$$

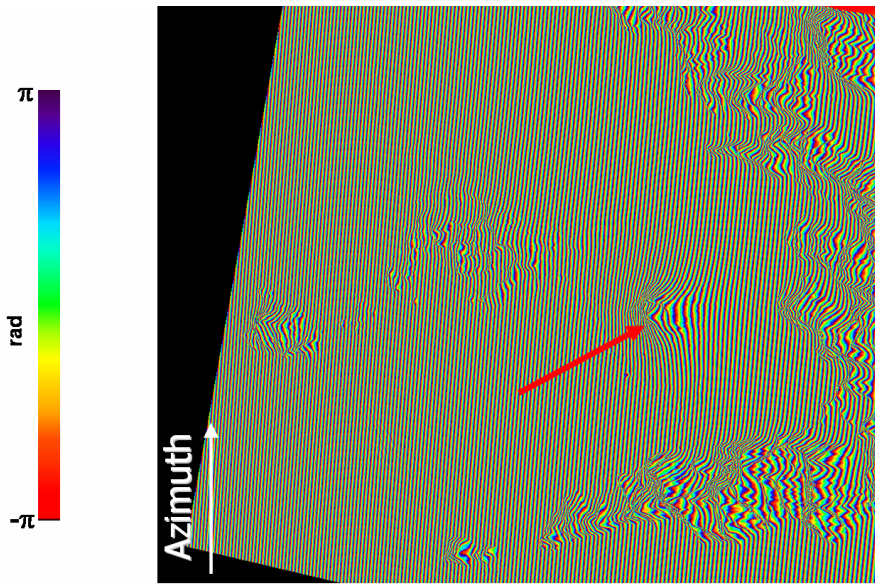

Figure 2. 8 An example of a synthetic interferogram relevant to the Napoli bay test site. The topographic fringes related to the Vesuvius complex are clearly visible at the center of the image in correspondence to the red arrow line.

The second step of the procedure concerns the measure, acquisition by acquisition, of the SAR sensor position in the SAR coordinates, directly. In particular, the k-th SAR acquisition will be characterized by its own orbital parameters so that, at the time t_i (which corresponds to the azimuth pixel i onto the SAR geometry), the position vector will be

$$\vec{s}_k = \begin{cases} x_{s_k} = \tilde{a}_0 + \tilde{a}_1 (t_i - t_0) + \tilde{a}_2 (t_i - t_0)^2 + \tilde{a}_3 (t_i - t_0)^3 \\ y_{s_k} = \tilde{b}_0 + \tilde{b}_1 (t_i - t_0) + \tilde{b}_2 (t_i - t_0)^2 + \tilde{b}_3 (t_i - t_0)^3 \\ z_{s_k} = \tilde{c}_0 + \tilde{c}_1 (t_i - t_0) + \tilde{c}_2 (t_i - t_0)^2 + \tilde{c}_3 (t_i - t_0)^3 \end{cases} \quad (9)$$

The third step concerns the estimation of the slant range distances performed directly onto the SAR reference system. To do this, we observe that, for the i-th azimuth line, the slant range distance with respect to the target associated to the j-th range coordinate, it can be easily evaluated in application of the Pitagora's law

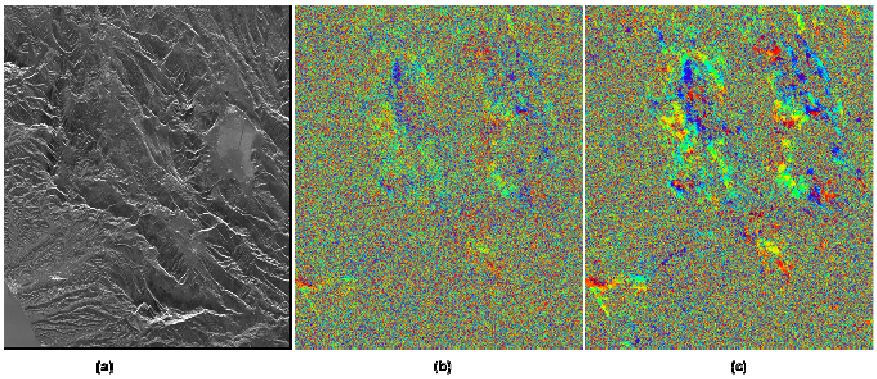

Figure 2. 9 SAR products relevant to the Napoli bay test site. (a) Multilook intensity image of the investigated area. (b) Multilook differential interferogram computed from the ERS data pair acquired on September 5, 1992 and March 11, 1996, respectively. (c) The noise-filtered differential interferogram relevant to the same data-of (b).

$$r_k(i,j) = \sqrt{\left(\tilde{X}_e(i,j) - x_{s_k}(i)\right)^2 + \left(\tilde{Y}_e(i,j) - y_{s_k}(i)\right)^2 + \left(\tilde{Z}_e(i,j) - z_{s_k}(i)\right)^2}$$
$$\forall j = 1,\ldots,N_{RG} \qquad (10)$$
$$i = \left(t - t_0\right)\cdot PRF$$

wherein N_{RG} is the number of range samples. Finally, according to the equation (4) the topographic, synthesized fringes will be directly evaluated onto the SAR geometry by exploiting the two so-estimated slant range differences, associated to the SAR images involved in the considered D-InSAR data pair.

We finally note that the described procedure is particularly flexible to produce whatever topographic fringes one wants through a trivial estimation of the slant range distance matrices.

2.6 Differential Interferogram Generation

Once the topographic phase contribution has been estimated, the differential interferometric phase can be carried out by subtracting it to the interferometric phase term

$$\Delta\varphi = \frac{4\pi}{\lambda}\Delta r \qquad (11)$$

As stated before, the retrieved phase takes also accounts of spurious terms depending on the inaccuracies on the knowledge of the real topography and on the errors on the baseline estimation and on the presence of noise contributions. Hence, before to proceed, it is convenient to reduce the noise effect via a proper noise filtering operation. This task can be achieved, for example, by following the approach proposed by Goldstein et al. [49] , whose key aspects will be briefly summarized.

We start from the observation that the interferogram power spectra of most regions is characterized by a "white" component, generated by thermal noise and loss of correlation, and a narrow band component, related to the fringes. The non-stationarity of the fringe spectrum requires an adaptive filtering algorithm sensitive to the local phase noise and fringe rate. The proposed algorithm requires the interferogram is segmented into overlapping rectangular patches and the power spectrum (as for example a Gaussian shaped one) for each patch is computed by smoothing the intensity of the two-dimensional FFT. The response of the used, adaptive filter $H(u,v)$ is then computed from the power spectrum $Z(u,v)$ as follows

$$H(u,v) = \left|Z(u,v)\right|^{\alpha} \tag{12}$$

For the case where the filter parameter is equal to zero no filtering occurs, while for $\alpha = 1$ the filtering is strong. A pictorially example of the achievable improvement which can be gained by applying this algorithm to a set of differential interferograms is shown in Figure 2.9 wherein the filtered (with $\alpha = 0.75$) and the corresponding non-filtered differential interferogram have been presented.

2.7 Deformation time-series processing chain

This section will deal the procedures followed to produce deformation time-series from a set of "noise-filtered differential SAR interferograms". Note that, since the interferometric products are related to differential measurements, before to proceed, it is necessary to select as reference a point in space, located in a non-deforming zone (or in a zone whose real deformation is a-priori known) with respect to each the estimated deformation will be referred.

The whole procedure can be essentially viewed as the cascade of the following steps (see Figure 2.10):

1. In order to extract from each differential interferogram an information concerning the full deformation occurring between the

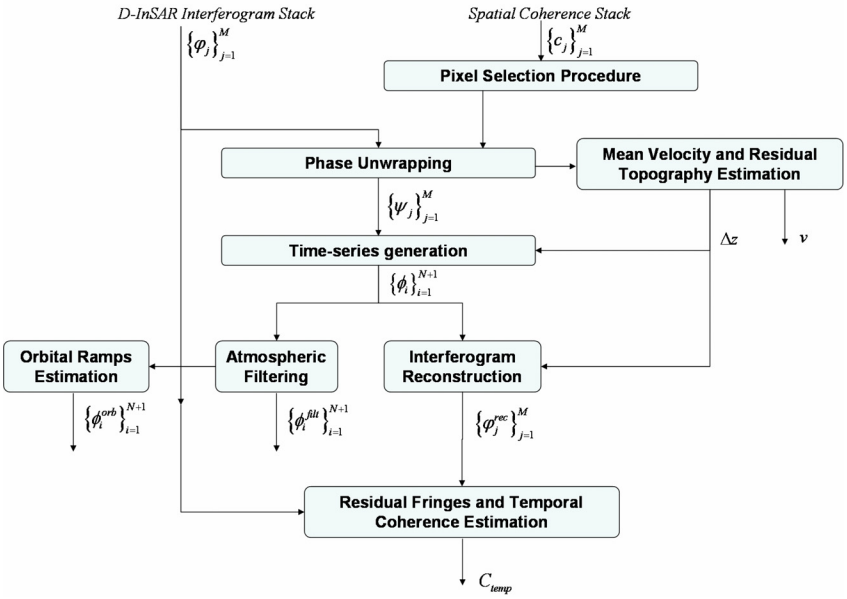

Figure 2. 10 SBAS time-series generation flow chart.

two sensor flights over the illuminated, the differential phases must be, first of all, properly unwrapped.

2. The unwrapped phases can be, in turn, used within the time-series generation process, which can be carried out (with regard to the SBAS algorithm) in application of the Singular Value Decomposition (SVD) [50] method. Indeed, as already discussed, the chosen interferometric data pair distribution satisfies a set of constraints on the spatial and temporal baseline separation as well on the doppler frequency shift. Accordingly, the SAR images involved in the interferogram generation could be arranged in several, independent small baseline subset, thus requiring that a proper linkage of the different subset must be considered.
3. The atmospheric phase screen (APS) is finally evaluated and subsequently removed from the obtained deformation time-series.

As an example, in this section the results achieved by referring to two different data-set, relevant to the Abruzzi (central Italy) and the Napoli bay (southern Italy) areas will be presented. Moreover, although a more comprehensive analysis relevant to this issue can be found in [39], a short review of the overall procedure will be done.

For this purpose, let us refer to a set of N+1 SAR images, acquired at the ordered times $(t_0, t_1, ..., t_N)$ and relevant to the same area, from which a sequence of M differential SAR interferograms $(\varphi_0, \varphi_1, ..., \varphi_{M-1})$ has been produced.

2.7.1 Pixel Selection Criterion

The first step of the presented algorithm involves the selection of a set of spatial pixels, characterized by a stable phase screen (i.e. with a relatively small phase standard deviation). This task can be accomplished, equivalently, by searching for the pixels characterized by high values of the spatial coherence (evaluated interferogram by interferogram). Basically, starting from the available sequence of the spatial coherence maps, a mask accounting of the highly spatially coherent pixels can be produced. In particular, the mask will account of the pixels with a coherence value, estimated in a box whose dimensions are related to the multi-looked resolution cell, greater than a given threshold (for example equal to 0.35) in at least a certain percentage of the number of interferograms.

This pixel selection procedure is aimed to neglect areas with significant decorrelation effects that are particularly difficult to be analyzed, especially if we refer to the Phase Unwrapping step.

2.7.2 Phase Unwrapping (PhU) Step

Following the pixel selection step, since the phase information in the interferograms is restricted to the $[-\pi, \pi]$ interval while we are interested to the full phase contribution, a critical, non linear operation step to unwrap the measured phases is clearly necessary. Several different approaches have been up to now proposed to solve this problem, most of them typically applied to each single interferogram, only [51-57]. Among these, one of the most utilized procedure is based on the solution of an equivalent Minimum Cost Flow (MCF) network and is typically applied to a sparse data grid [56]. Here, we would like introduce only the key concepts of the time-series generation algorithm, by referring the reader to the next chapter for a complete overview of the phase unwrapping technique. Accordingly, by referring to the generic pixel of SAR coordinates (a_z, r_g), the PhU procedure will be treated like a black box whose inputs are the wrapped phase signals $\{\varphi_j(a_z, r_g)\}_{j=0}^{M-1}$ and the corresponding outputs are the unwrapped ones $\{\psi_j(a_z, r_g)\}_{j=0}^{M-1}$.

It is important to note that in the D-InSAR scenario, the temporal relationships among the different interferometric phases should be effectively investigated in order to limit the Phase Unwrapping errors. Nevertheless, this is a difficult task to be accomplished, thus requiring that a joint analysis of both spatial and temporal constraints are considered.

In this context a novel phase unwrapping algorithm that works by exploiting also a set of temporal constraints on the differential phases has been developed and will be presented in the next chapter.

2.7.3 Estimation of the residual topography contribution

The unwrapped phase interferograms are directly related to the relative deformation occurring between the corresponding flights of the radar sensor over the illuminated area. The expression of the generic j-th differential interferogram, computed from the SAR acquisitions at times t_a and t_b and evaluated with regard to the generic pixel of SAR coordinates (a_z, r_g), will be (see chapter 1, equation 78) the following

$$\begin{aligned}\psi_j(a_z,r_g) = &\frac{4\pi}{\lambda}\frac{b_{\perp j}}{r\sin\vartheta'}\Delta z(a_z,r_g) + \frac{4\pi}{\lambda}\left[d(t_B,a_z,r_g) - d(t_A,a_z,r_g)\right] + \\ &+ \frac{4\pi}{\lambda}\left[d_{atm}(t_B,a_z,r_g) - d_{atm}(t_A,a_z,r_g)\right] + \Delta n_j(a_z,r_g)\end{aligned} \tag{13}$$

wherein λ is the signal wavelength, $b_{\perp j}$ the perpendicular baseline of the interferometric data pair, ϑ' the incidence angle (of about 23° for the ERS1-2 radar sensors), r the sensor to target distance of the considered pixel, $\Delta z(a_z, r_g)$ the unknown residual topography due to an incorrect estimation of the topographic fringes, $d(t_k, a_z, r_g)$ the unknown, requested deformation value of the considered SAR pixel relevant to the t_k time, $d_{atm}(t_k, a_z, r_g)$ the atmospheric contribution and, finally, $\Delta n_j(a_z, r_g)$ is the noise which affects the interferometric phase. Note also that possible orbital ramps artifacts can be considered as a part of the unknown atmospheric phase screen and that the $b_{\perp j}/r\sin\vartheta'$ term (which may significantly vary over the whole scene) here has been here thought, for sake of convenience, as a constant.

We can easily estimate the residual topographic term Δz by imposing the $d(\cdot) + d_{atm}(\cdot)$ signal could be approximated with a linear model, which

depends on the mean velocity factor v, only. In this manner, we can reformulate the system of equation (13) in a novel fashion with respect to the two unknowns $(\Delta z, v)$, as follows

$$\psi_j(x,r) \cong \frac{4\pi}{\lambda}\left[\frac{b_{\perp j}}{r\sin\vartheta}\Delta z + v\Delta T\right] \tag{14}$$

which can be solved in the Least Squares (LS) sense. As a further remark, we observe that the evaluation of the residual topography $\Delta z(a_z, r_g)$ benefits for the presence of interferometric distribution with significantly large perpendicular baseline values, thus suggesting us to increase the maximum acceptable perpendicular baseline value but, obviously, the higher are the baseline values the more significant are the noise effects. Therefore, the choice of the optima maximum baseline separation must be take account of these two opposite requirements.

Accordingly, the residual topographic pattern can be subtracted to each unwrapped differential interferogram, thus leading to the following expression of the topography-compensated differential interferogram

$$\begin{aligned}\tilde{\psi}_j(a_z,r_g) = \frac{4\pi}{\lambda}\left[d(t_B,a_z,r_g) - d(t_A,a_z,r_g) + d_{atm}(t_B,a_z,r_g) - d_{atm}(t_A,a_z,r_g)\right] + \\ + \Delta n_j(a_z,r_g) = \phi(t_B,a_z,r_g) - \phi(t_A,a_z,r_g)\end{aligned} \tag{15}$$

which defines a novel system of equations in the $\{\phi_i(a_z, r_g)\}_{i=0}^{N}$ unknowns to be properly solved.

2.7.4 Deformation Time-series extraction

In this section, the solution of the system of equations (15) will be addressed. First of all, we observe that it can be reorganized by using a matrix formalism as follows

$$\mathbf{A}\cdot\mathbf{\Phi} = \tilde{\mathbf{\Psi}} \tag{16}$$

where A is an incidence-like matrix, directly related to the set of generated interferograms, whose elements are so-defined

$$\begin{cases} A\left(j, IM_j\right) = 1 & IM_j \neq 0 \\ A\left(j, IS_j\right) = -1 & IS_j \neq 0 \\ 0 & \text{otherwise} \end{cases} \tag{17}$$

wherein **IM** and **IS** are the vectors whose generic elements represent the indices of the master and the slave time acquisitions (with respect to the whole time acquisitions vector $\left(t_0, t_1, ..., t_N\right)$), respectively. Note the rank of **A** would be M-1 if all the SAR acquisitions were connected (that would be the case if one subset was present). The equation system will be well-determined if $N = M - 1$, or over determined if $N > M - 1$. The solution of this system can be obtained in the Least Squares (LS) sense, that is

$$\mathbf{\Phi} = \mathbf{A}^{+} \cdot \tilde{\mathbf{\Psi}} = \left(\left(\mathbf{A}^{\mathbf{T}} \cdot \mathbf{A}\right)^{-1} \cdot \mathbf{A}^{\mathbf{T}}\right) \cdot \tilde{\mathbf{\Psi}} \tag{18}$$

where $\mathbf{A}^{+}$ is the left inverse matrix. But data, in general, will correspond to several different subsets so that the matrix **A** will not be of a complete rank. Its rank will be reduced according to the number of subsets, leading to a singular matrix $\mathbf{A}^{+}$ which suggests us that the number of solutions will be infinite. In this case, we will use the singular value decomposition (SVD) method to invert the system.

The SVD decomposition of a generic matrix **A** may be written as

$$\mathbf{A} = \mathbf{U} \cdot \mathbf{S} \cdot \mathbf{V}^{\mathbf{T}} \tag{19}$$

where U is an $M \times M$ orthogonal matrix, whose first N columns are the eigenvectors of the matrix $A^T A$, S is an MxM diagonal matrix, whose elements are the so-called singular values and V is an $N \times M$ orthogonal matrix, whose columns are the eigenvectors of the matrix $A^T A$. We explicitly note that, if L is the number of the different subset we have, only $N - L + 1$ of the diagonal values of the matrix S will be not equal to zero. The minimum norm least squares solution for $\mathbf{\Phi}$ is then achieved via the equations (18) and (19) and will be

$$\mathbf{\Phi} = \left[\mathbf{V} \cdot \mathbf{diag}\left(1/\sigma_1, 1/\sigma_2, ..., 1/\sigma_{\text{N-L+1}}, 0, ..., 0\right) \cdot \mathbf{U}^{\mathbf{T}}\right] \cdot \tilde{\mathbf{\psi}} = \sum_{i=1}^{N-L+1} \frac{\mathbf{\psi}^{\mathbf{T}} \cdot \mathbf{u}_i}{\sigma_i} \mathbf{v}_i \tag{20}$$

The determination of the inverse matrix of **A** is a well-posed problem and therefore the propagation of relative errors from the data to the solution is controlled by the condition number, so-defined

$$cond\left(A\right)=\left\|\mathbf{A}\right\|\cdot\left\|\mathbf{A}^{-1}\right\|=\frac{\sigma_1}{\sigma_{N-L+1}}\geq 1 \tag{21}$$

When this number is too large, the problem (15) is said to be well-conditioned and the solution is stable with respect to small variations of the data. On the other hand, when *cond*(A) is very large, the problem is said to be ill-conditioned and a small variation of the data can produce a completely different solution.

Unfortunately, this solution, being obtained by imposing a minimum norm criterion on the cumulative deformation phase Φ is responsible to introduce large discontinuities in the obtained results, thus leading to a non physical sound solution (see Figure 2.11). A most effective strategy to overcome this problem can be accomplished by manipulating the system of equations (16) in such a way to replace the present unknowns with the mean phase velocity between time adjacent acquisitions. Therefore, in application of the minimum norm solution, this is equivalent to minimize the adjacent, mean deformation velocity. Accordingly, the new unknowns become

$$v_d^T=\left(v_{1d}=\frac{\Phi_1-\Phi_0}{t_1-t_0},v_{2d}=\frac{\Phi_2-\Phi_1}{t_2-t_1},...,v_{Nd}=\frac{\Phi_N-\Phi_{N-1}}{t_N-t_{N-1}}\right) \tag{22}$$

which, properly substituted in equation (16), lead to the new system of equations

$$\mathbf{B}\cdot\mathbf{v_d}=\tilde{\mathbf{\Psi}} \tag{23}$$

where $\mathbf{B}$ is an $M\times N$ matrix, whose elements are so-defined

$$B\left[i,j\right]=\begin{cases}t_{j+1}-t_j & IM_i\leq j\leq IS_i\\ 0 & elsewhere\end{cases} \tag{24}$$

The unknown mean velocity vector can be again estimated via the application of the singular value decomposition technique, but now with reference to the matrix $\mathbf{B}$. In this case, compared to the previously analyzed case, an additional integration step will be necessary in order to compute the required deformation phases, starting from the estimated vector $\mathbf{v_d}$, that is

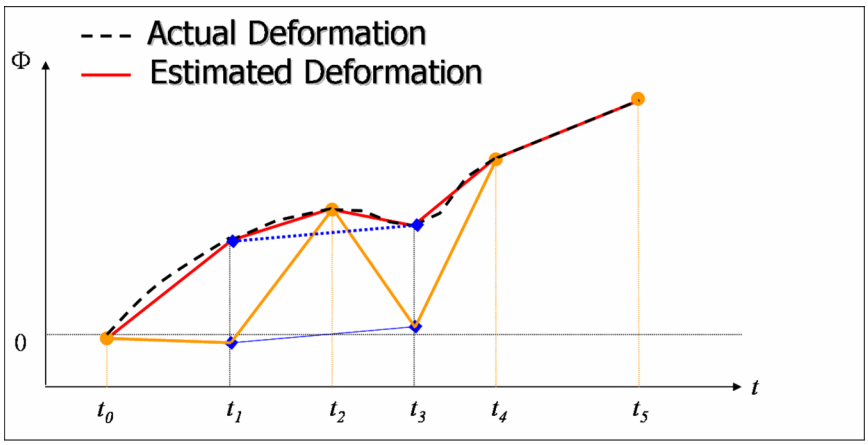

Figure 2. 11 A key example describing how the SVD works. The dotted line refers to the simulated deformation time-series, the orange lines describes the deformation time-series achieved in application of a minimum norm deformation criterion search and the blu line concerns the independently obtained subset two deformation time-series. The red line finally represents the estimated deformation time-series obtained in application of the SVD inversion method.

$$\Phi(t_i) = \sum_{k=1}^{i} v_{dk}\left(t_k - t_{k-1}\right) \quad \forall i = 1,\ldots,N$$
$$\textit{with} \qquad (25)$$
$$\Phi(t_0) = 0$$

2.7.5 Estimation of the reconstruction accuracy

Phase unwrapping errors, noisy differential interferograms and incongruences on the solution of the system of equations (23) (due to a high value of the relevant condition number), may lead to a resulting deformation pattern that is not consistent with the original fringe phases. For this purpose, a procedure allowing us to argue on the correctness of our results has to be introduced. To do this, pixel by pixel, we can reproduce the original D-InSAR phases, starting from the achieved phase terms Φ associated to each SAR image. Obviously, within the reconstruction procedure, the previously estimated residual topography must be again taken into account; hence, the reconstructed D-InSAR phase will be expressed as follows

$$\varphi_j^{rec} = \frac{4\pi}{\lambda}\frac{b_{\perp j}}{r\sin\vartheta}\Delta z + \left[\Phi\left(t_{IM_j},x,r\right) - \Phi\left(t_{IS_j},x,r\right)\right] \tag{26}$$

where $P(x,r)$ is the generic pixel on the SAR geometry we considered.

Therefore, we can use as a quality index of the deformation retrieval, the temporal coherence factor, defined for each pixel as follows

$$C_{temp} = \frac{\left|\sum_{k=1}^{N}\exp\left[j\left(\varphi_k^{rec} - \varphi_k\right)\right]\right|}{N} \tag{27}$$

Note that for pixels where $\gamma \to 1$, we expect that no errors (for the most part due to phase unwrapping inconsistencies) are present, since a nearly perfect retrieval of the original phase has been obtained. On the other hand, low values of γ will correspond to poorly reconstructed data. A pictorial example of this kind of products has been shown in Figure 2.12.

2.7.6 Atmospheric Filtering and Orbital Ramps Estimation

The final step of the deformation time-series extraction process is focused on the separation of the atmospheric phase screen (APS) term from the deformation component, itself. This operation can be performed according to the strategy discussed in [35,45]. It is based, in particular, on the key observation that the atmospheric phase component is highly correlated in space, but poorly in time so that, the undesired APS can be estimated as follows

- First of all, the Low Pass (LS) deformation signal is detected and removed from the estimated deformation time-series;
- After that, the APS component is estimated as the High Pass (HP) temporal component of the residual phase signal, which is highly correlated in space. This is done through the cascade of a HP-temporal filtering step and a LP-spatial one.

When the APS signal has been estimated, it is then subtracted from the achieved deformation phase signal. At this stage, to obtain the displacement signal, the phase must be subsequently multiplied by the factor $\lambda/4\pi$ (see equation 11).

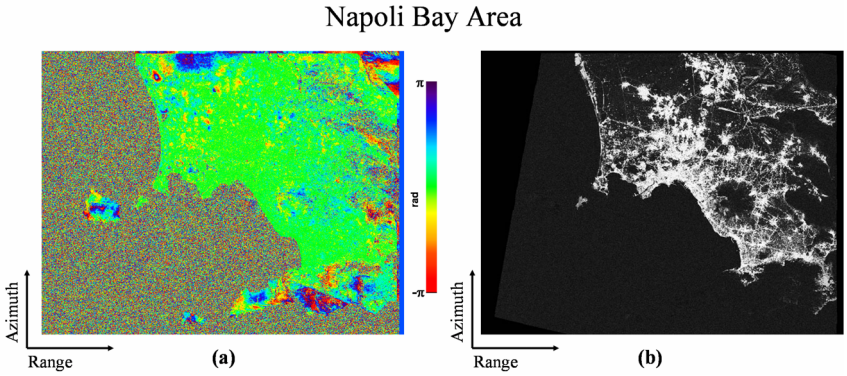

Figure 2. 12 Interferometric products concerning the correctness of the deformation time-series reconstruction. (a) An example of the residual phase term (defined as the wrapped phase difference between the reconstructed differential interferogram and the original one) that one can obtain. (b) The temporal coherence map, represented in a grey scale, of the considered interferometric data-pair distribution.

Once the atmospheric filtered deformation term $\vec{\varphi}^{filt}(t_0,t_1,...,t_N)$ has been retrieved, one can estimate, for each temporally coherent pixel, the correct mean velocity deformation value directly searching for the inclination of the line that best fits the deformation time-series, itself. In other words we may look for the term α which satisfies the following condition

$$\min\left\|\alpha\vec{t}-\vec{\varphi}^{filt}\right\| \tag{28}$$

Nevertheless, the estimated APS term could also contain phase terms due to the inaccuracies on the knowledge of the orbital parameters (see equation 75, chapter one), which imply the presence of residual orbital planes on each layer of the estimated APS stack of data.. To isolate these effects that are responsible, for example, for a quality reconstruction decrease of the unwrapped interferograms, a further filtering step, applied to each single component of the APS term, can be arranged. This approach allows retrieving an estimate of the term we are searching for

$$d_{atm}(t_i)=\hat{d}_{atm}(t_i)+e_{orb}(t_i)\cong\hat{d}_{atm}(t_i)+\frac{4\pi}{\lambda}\frac{r'-r_0}{r'\tan(\vartheta')}\Delta B_{\perp i} \tag{29}$$

wherein $\Delta B_{\perp i}$ represents the error on the knowledge of the data-pair perpendicular baseline value, $r'-r_0$ is the slant range difference with respect to the reference SAR pixel, $\hat{d}^{atm}(t_i)$ is the actual atmospheric phase contribution and $e_{orb}(t_i)$ is the orbital ramp contribution. However, it is important to underline that the presented approach is less precise if a deformation pattern spatially correlated with a ramp is actually present. In these cases, conversely, the spurious phase ramps can be also detected and removed directly on each interferogram by searching for the phase ramps correlated to the unwrapped interferogram, itself.

Once the phase ramp term have been estimated, they can be effectively subtracted modulo-2π to the original interferograms, thus obtaining a novel sequence of differential interferograms that can be subsequently re-processed via the same strategy up to now described.

2.8 Geocoding of the SAR products

The deformation products, directly obtained onto the SAR reference geometry, have to be finally represented with respect to an easier output reference grid and, for this purpose, they are *"geolocalized"* onto a cartographic reference system [58-59]. To do this, the knowledge of the scene topography, eventually achieved directly onto the SAR geometry via the application of InSAR techniques and/or properly corrected via the procedure discussed in section 2.7.5, is needed. We observe that, according to the considerations we made about the estimation of the slant range matrices (see section 2.2), we can assume that the available information from a SAR image, with respect to a target on the ground, are:

1. The target slant range coordinate, which allows localizing it on a sphere;
2. The target azimuth coordinate, representing the position of the target on the plane orthogonal to the flight path.

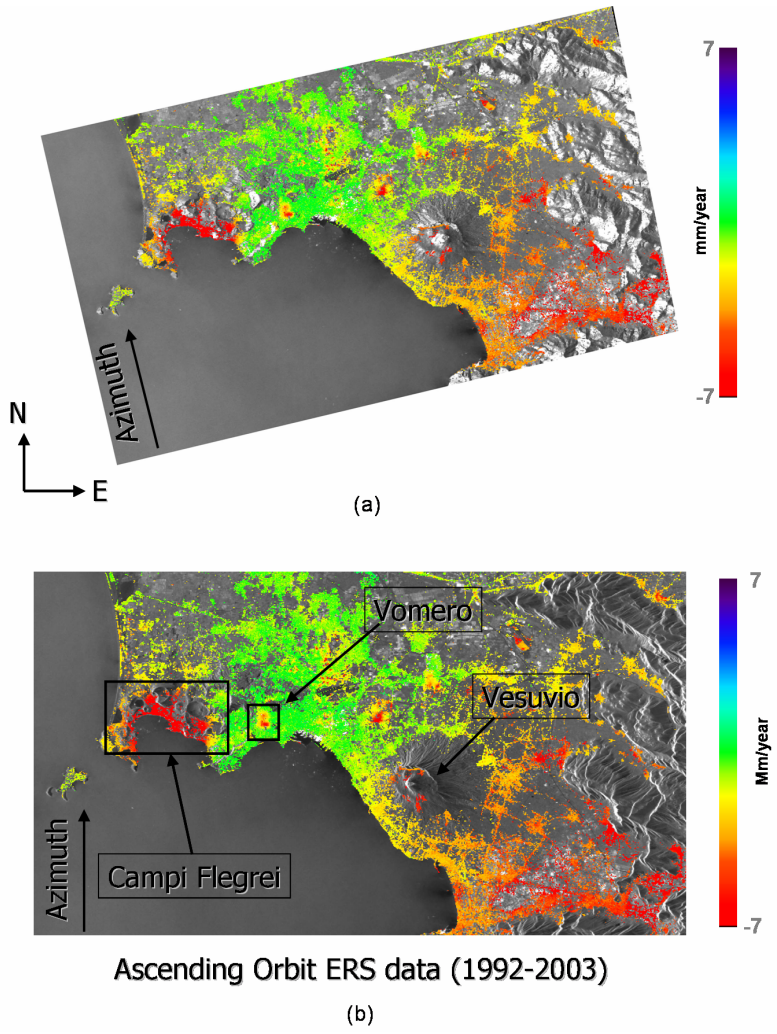

Figure 2. 13 False color deformation velocity maps relevant to the Napoli bay area, as measured from a set of SAR data acquired from the ascending orbits, represented both in the cartographic output grid (a) and with respect to the SAR coordinates (b), respectively.

The problem to locate the target on the ground, that is to individuate its coordinates with respect to the cartesian reference system we considered (see section 2.2), can be solved if the height of the target (with respect to the reference ellipsoid) is a priori known, only. In this manner, each SAR pixel will be transformed in a corresponding point of cartesian coordinates

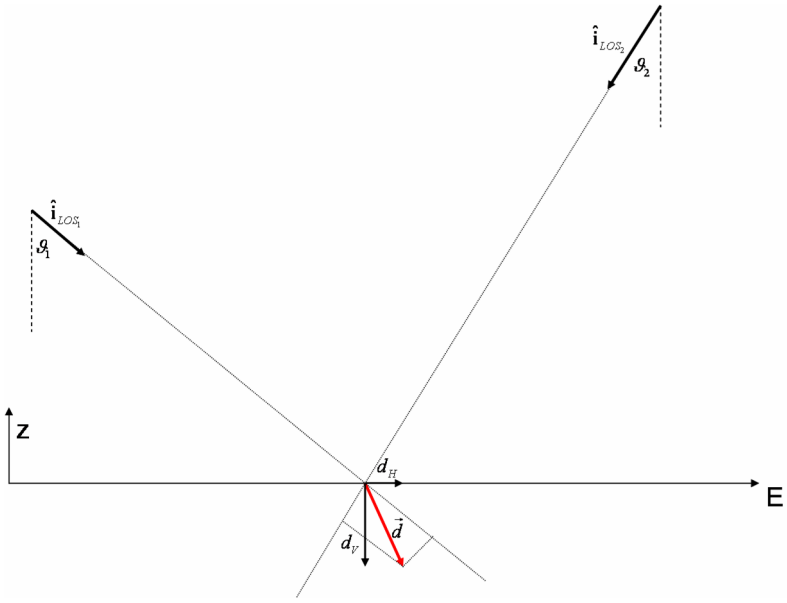

Figure 2. 14 SAR geometry in the East-z plane with the displacement vector d (red line), its two generic LOS projections and the east-west d_H and vertical deformation components d_V highlighted, respectively.

(x, y, z) in the reference system, by searching for the solution of the following, non linear system of equations with respect to the P unknowns

$$\begin{aligned} & r = \left|\mathbf{s}(t) - \mathbf{P}\right| \\ & \mathbf{v}(t) \cdot \left(\mathbf{s}(t) - \mathbf{P}\right) = 0 \\ & \frac{x^2 + y^2}{\left(a+h\right)^2} + \frac{z^2}{\left(b+h\right)^2} = 1 \end{aligned} \tag{30}$$

where the last equation accounts for the fact that the target has a known height h with respect to the reference ellipsoid. Once the system has been solved, the target position can be referred to a geographic system or transformed into a cartographic projection (as for example the Universal Transverse Mercator (UTM) projection). In Figure 2.13, as an example, is shown the velocity map of the Napoli bay area, as observed from the ascending orbits, represented onto the SAR reference geometry and with respect to the geocoded output grid, respectively.

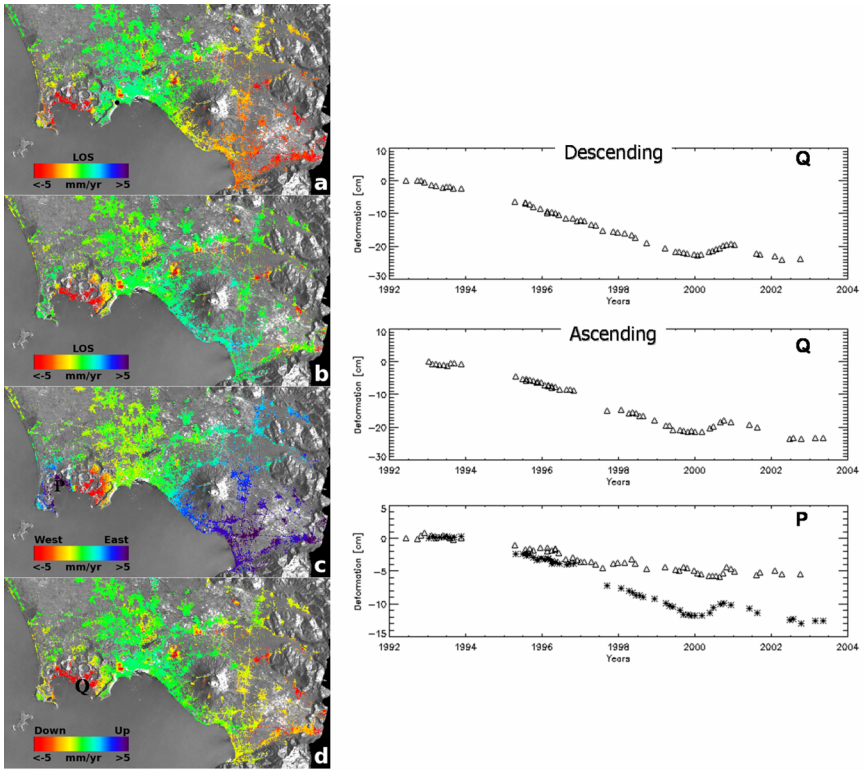

Figure 2. 15 The Campi Flegrei and Vesuvius test site area results. (a) and (b) shows the LOS mean velocity deformation of the area, as observed by the descending and the ascending orbits, respectively. (c) is the east-west deformation component and (d) the vertical displacement components. The presented ascending and descending deformation time-series demonstrate that if the area is affected by a nearly vertical deformation phenomenon the two LOS components are of the same magnitude (see pixel Q) , while if the east-west deformation components are not negligible, the comparison shows (see pixel P) that the two trends are significantly different.

2.9 Multi-orbital deformation combination

The exploitation of the deformation measurements, directly represented onto the output, geocoded geometry, allows us to merge the information about the deformation collected from the different orbital positions and to discriminate one another the deformation components, itself [60,61].

To this purpose, let us suppose (by referring to the most generalized case represented in Figure 2.14) to have two different viewing angles. Therefore,

the components of the deformation, as measured from the SAR sensors along the two lines of sight, can be expressed

$$\begin{cases} d_{LOS_1} = \vec{d} \cdot \vec{i}_{LOS_1} = d_H \sin \vartheta_1 + d_V \cos \vartheta_1 \\ d_{LOS_2} = \vec{d} \cdot \vec{i}_{LOS_2} = -d_H \sin \vartheta_2 + d_V \cos \vartheta_2 \end{cases} \tag{31}$$

which can be equivalently expressed via the following matrix representation

$$\begin{pmatrix} \sin \vartheta_1 & \cos \vartheta_1 \\ -\sin \vartheta_2 & \cos \vartheta_2 \end{pmatrix} \cdot \begin{pmatrix} d_H \\ d_V \end{pmatrix} = \begin{pmatrix} d_{LOS_1} \\ d_{LOS_2} \end{pmatrix} \tag{32}$$

and easily solved with respect to the two components of the deformation, the former (d_H) is relevant to the east-west direction and the latter (d_V) to the vertical one.

$$\begin{pmatrix} d_H \\ d_V \end{pmatrix} = \begin{pmatrix} \sin \vartheta_1 & \cos \vartheta_1 \\ -\sin \vartheta_2 & \cos \vartheta_2 \end{pmatrix}^{-1} \cdot \begin{pmatrix} d_{LOS_1} \\ d_{LOS_2} \end{pmatrix} = \frac{\begin{pmatrix} d_{LOS_1} \cos \vartheta_2 - d_{LOS_2} \cos \vartheta_1 \\ d_{LOS_1} \sin \vartheta_2 + d_{LOS_2} \sin \vartheta_1 \end{pmatrix}}{\sin(\vartheta_1 + \vartheta_2)} \tag{33}$$

This approach can be, in particular, followed if the ascending and descending deformation time-series have to be combined. Obviously, in this case, the two side-looking angles, being the area imaged by two perfectly symmetrical viewing angles, are the same. Hence, it is easy to demonstrate that

$$\begin{cases} d_H = \dfrac{\cos \vartheta}{\sin(2\vartheta)} \left(d_{LOS_1} - d_{LOS_2} \right) = \dfrac{d_{LOS_1} - d_{LOS_2}}{2 \sin \vartheta} \\ d_V = \dfrac{\sin \vartheta}{\sin(2\vartheta)} \left(d_{LOS_1} + d_{LOS_2} \right) = \dfrac{d_{LOS_1} + d_{LOS_2}}{2 \cos \vartheta} \end{cases} \tag{34}$$

We may observe that the vertical displacement is associated to the sum of the two LOS deformation measurements while the east-west component is related to the difference of the two deformation measurements, respectively. It is important to stress that the sensibility of the radar measurements along the north-south direction is quite limited. In fact, the sensor flight trajectories are approximately parallel to the north-south direction and, as already explained, the radar techniques (measuring range distances, only) are not

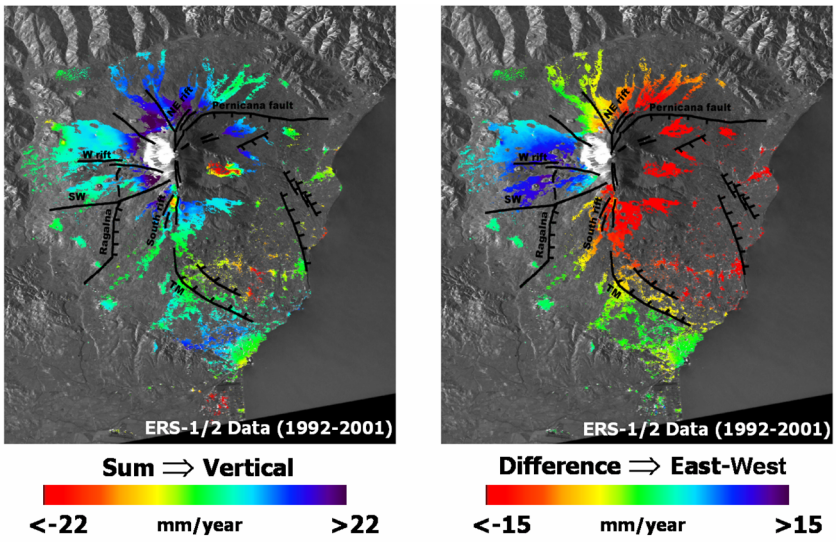

Figure 2. 16 Time series inversion velocity maps. Average linear velocities for each pixel are shown with an average coherence greater than or equal to 0.6, following the analysis technique of Berardino et al. [2002]. The deformation has been evaluated with respect to a point located in Catania city (at the lower right side of the image) which has been considered stable. (a) Sum of the ascending and descending velocity maps. (b) Difference between the ascending and descending velocity maps for pixels in common. Solid lines indicate the fault system of the area.

capable to measure displacements with respect to the sensor flight trajectory (i.e., the azimuth direction). Two examples showing what one can be achieved by applying these combination strategies are shown in Figures 2.15 and 2.16, where the decomposition of the mean velocity deformation onto its two observable components are presented with respect to the investigated areas of the Mount Etna (Sicily, Italy) and to the Napoli bay (Italy) area.

2.10 Summary

In this chapter, the interferometric products achievable by using a set of multiple differential interferograms and the relevant applied techniques have been presented. In particular, we focused on the application of the Small Baseline inversion algorithm, thus exploring its potentiality to retrieve the temporal deformation pattern of illuminated areas. We remark that the investigated D-InSAR approach has been successfully applied in the recent

years to study an extremely wide range of geophysical processes and several works have been also published [61-67].

In this context, we have firstly introduced the key ideas of the algorithms one can exploits and, after that, a set of possible applications.

Chapter 3

Extended Minimum Cost Flow (EMCF) Phase Unwrapping Algorithm

We focused, up to now, on the key topics of the Differential Synthetic Aperture Radar Interferometry (D-InSAR) that, as said before, is a well-known remote sensing technique with important applications within the investigation of several geophysical processes, thanks to its capability to produce spatially dense deformation maps with centimeter to millimeter accuracy [30] . Besides, as discussed in the previous chapter, while the D-InSAR approach has been applied first to the analysis of single deformation episodes, now is a growing interest on extending this technique to the study of the temporal evolution of the detected displacements, via the generation of deformation time-series. To achieve this task, the information available from each interferometric data pair must be properly related to those included in the other acquisitions via the generation, and a subsequent combination , of an appropriate sequence of D-InSAR interferograms. Thus, the profitably information is essentially associated to phase terms. Nevertheless, we can exploit that the interferometric phase signatures vary relatively smoothly from point to point in the interferogram, thus recovering the overall displacements fields. In fact, the measurable phase are restricted to the $[-\pi,\pi]$ interval, that is the integral number of phase cycles on each measurement is lost. Consequently, if the surface displacement in a scene is greater than one half radar wavelength, and the resulting interferogram phase excursion greater than one cycle, or if the combination of interferometric baseline and residual surface topography yields more than one fringe on the topographic signature, the interferogram cannot be uniquely inverted without a procedure to recover the missing cycles. We refer to such a procedure to as Phase Unwrapping (PhU).

This chapter will be focused on the analysis of this task and will start from a short overview of the basic theory concerning this issue. After that, we will concentrate on the presentation of a novel PhU approach, realized within the framework of the doctoral studies, that represents an extension of the Minimum Cost Flow (MCF) algorithm [55] to the Temporal/Perpendicular baseline domain.

3.1 Phase Unwrapping Problem

In order to clarify the key aspects of the phase unwrapping problem, let us firstly refer to a single differential interferogram and denote with $\phi(a_z, r_g)$ the measured interferometric phase related to the pixel of SAR coordinates (a_z, r_g). As stated before, we are interested to the evaluation of the corresponding full interferometric phase $\psi(a_z, r_g)$, directly related to the deformation $d(a_z, r_g)$ occurring between the corresponding passages of the radar sensor over the selected area, via the following relation

$$d(a_z, r_g) = \frac{\lambda}{4\pi}\psi(a_z, r_g) \tag{1}$$

where the full interferometric phase (i.e. the unwrapped phase) differs from the wrapped one by 2π-multiple integers $H(a_z, r_g)$, that is

$$\psi(a_z, r_g) = \phi(a_z, r_g) + 2\pi H(a_z, r_g) \tag{2}$$

Therefore, the aim of the phase unwrapping procedure is to retrieve a measure of the full phase through the observation of its wrapped value. To solve this problem, additional information must be employed. First of all, we may observe that the involved phase maps can be also viewed as functions of discrete coordinates (i, j) (that is, for example, $\psi = \psi(i, j)$), being

$$\begin{aligned} a_z &= a_{z0} + i\frac{v_s}{PRF} \\ r_g &= r_{g0} + j\frac{c}{2f_{samp}} \end{aligned} \tag{3}$$

the expression of the corresponding SAR coordinates, wherein (see chapter one) a_{z0} is the azimuth of the first line, v_s the sensor velocity, PRF the pulse repetition frequency, r_{g0} the near slant range difference, c is the speed of the light and, finally, f_{samp} is the range sampling frequency.

Consequently, we may refer to the discrete counterpart of the partial derivatives and, in particular, by using the popular wrapped-differences-of-wrapped-phases estimator, we can introduce the "measurable" phase gradient vector, defined as follows

$$\hat{\nabla}\boldsymbol{\psi} = \left\langle \Delta_x \psi \right\rangle_{-\pi,\pi} \hat{\mathbf{x}} + \left\langle \Delta_y \psi \right\rangle_{-\pi,\pi} \hat{\mathbf{y}} \tag{4}$$

whose components with respect to the two spatial axis $\hat{x}$ and $\hat{y}$ are

$$\begin{aligned} \left\langle \Delta_x \psi(i,j) \right\rangle_{-\pi,\pi} &= \left\langle \psi(i+1,j) - \psi(i,j) \right\rangle_{-\pi,\pi} = \left\langle \phi(i+1,j) - \phi(i,j) \right\rangle_{-\pi,\pi} \\ \left\langle \Delta_y \psi(i,j) \right\rangle_{-\pi,\pi} &= \left\langle \psi(i,j+1) - \psi(i,j) \right\rangle_{-\pi,\pi} = \left\langle \phi(i,j+1) - \phi(i,j) \right\rangle_{-\pi,\pi} \end{aligned} \tag{5}$$

being the symbol $\langle \cdot \rangle_{-\pi,\pi}$ representative of the modulo-2π operation. In other words, the measurable phase gradient vector has been estimated by wrapping possible phase differences greater than π in the $[-\pi,\pi]$ interval by adding the correct multiples of 2π and implicitly assuming that, in a properly sampled interferogram, the phase differences of adjacent samples are likely to be restricted to the $[-\pi,\pi[$ interval. Moreover, the probability that the phase difference exceed $\pm\pi$ depends both on the noise level (i.e. the lower is the coherence value the more likely the derivatives exceed $\pm\pi$) and, eventually, on the slope of the residual topography. For this reason, the introduced operator is not conservative, that is

$$rot\left(\hat{\nabla}\psi\right) = \nabla \times \left(\hat{\nabla}\psi\right) \neq 0 \tag{6}$$

and, hence, an integration of it will be path-dependent. On the contrary, the first constraint on the most part of the phase unwrapping algorithms is that it produce consistent results, that is, the same phase field should be recovered independently of the direction we choose to integrate the phase gradients. Moreover, we can observe that the phase gradient estimate has the advantage that its errors are localized and come in integer multiples of 2π so that, its curl (hereafter referred to as residue field) can be profitably used to reconstruct the full phase terms.

The residue field expression (see Figure 3.1) is the following

$$\begin{aligned} r(i,j) &= \nabla \times \left(\hat{\nabla}\psi(i,j)\right) = \Delta_x \left[\left\langle \Delta_y \psi(i,j) \right\rangle_{-\pi,\pi} \right] - \Delta_y \left[\left\langle \Delta_x \psi(i,j) \right\rangle_{-\pi,\pi} \right] = \\ &= \left\langle \Delta_x \psi(i,j) \right\rangle_{-\pi,\pi} + \left\langle \Delta_y \psi(i+1,j) \right\rangle_{-\pi,\pi} - \left\langle \Delta_x \psi(i,j+1) \right\rangle_{-\pi,\pi} - \left\langle \Delta_y \psi(i,j) \right\rangle_{-\pi,\pi} \end{aligned} \tag{7}$$

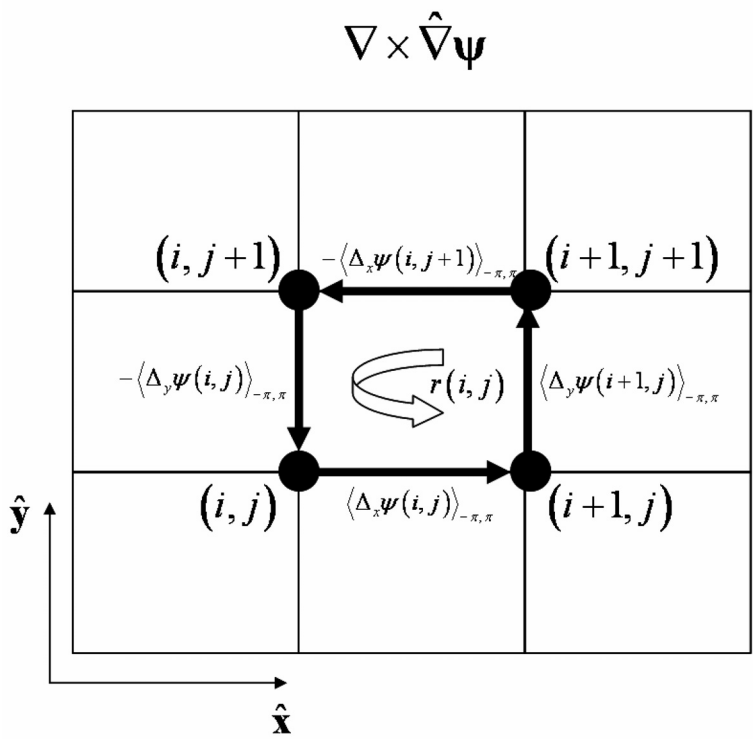

Figure 3. 1 Representation of the residue field r(i,j).

Its values are either zero (no residues) or 2π (positive or negative residue, respectively). Therefore, it is the goal of the phase unwrapping procedure to eliminate potential integration paths enclosing unequal numbers of positive and negative residues. Residue derives from two sources in the radar measurements. First is actual discontinuities in the data. The fringe spacing may be so fine on certain topographic slopes, or from large inter-observation displacement, as to exceed the Nyquist criterion of half-cycle spacing. The second is the noise in the data set, whatever from thermal and other noise sources or from decorrelation due to baseline length and temporal changes in the scene. However, residues from whatever source require compensation in the phase unwrapping procedure.

One of the major PhU algorithm exploits the fact that residues mark the endpoints of lines in the interferogram along which the true phase gradient exceed π/sample, these lines are commonly referred to as "branch-cuts" or "ghost-lines". Most of the algorithm up to now proposed are based on a

proper compensation of these residues and, among these, we will concentrate in the following on the residue-cut and the least-square approaches [68]

3.1.1 Branch-Cuts Algorithm

As an example, within this algorithm class we will refer to the "residue-cut tree algorithm" in particular. The initial residue-cut phase unwrapping procedure proposed by Goldstein [51] is implemented by first of all identifying the locations of all residues in an interferogram, and then connecting them with branch-cuts, so as to prevent the existence of integration paths that can encircle unbalanced numbers of positive and negative residues. The tree algorithm is a relatively conservative algorithm that tends to grow rather dense networks of trees in residue-rich regions. The algorithm initially connects closely spaced, oppositely charged, pairs of residues with cuts that prevent integration paths between them and, if all permitted integration paths enclose equal numbers of positive and negative residues, consistency is assured. Progressively longer trees are permitted until all residues are connected to, at least one, other residue and until the next charge on each tree is zero. Networks on small trees are used to prevent any single branch from becoming too long and isolating large sub-areas from the rest of the image. A consequence of the indiscriminate branch growth until charge neutrality is achieved from all trees, and all residues accounted for, is that in residue-rich regions the tree growth is so dense that the region is isolated from the remainder of the image and no unwrapped phase estimate can be obtained. By concluding, this conservative approach nearly eliminates mistakes but, at the expense of providing an incomplete unwrapping result.

3.1.2 Least-Squares Algorithms

The second major class of Phase Unwrapping algorithms, in common use today, was presented by Ghiglia and Romero [52], who applied a mathematical formalism first developed by Hunt [69] to the radar interferometry phase unwrapping problem. Hunt developed a matrix formulation suitable for general phase reconstruction problems; Ghiglia found that a discrete cosine transform technique permits accurate and efficient least-squares inversion, even for the very large matrices encountered in the radar interferometry special case. In particular, the unweighted LS method performs the following minimization problem

$$\min_{\tilde{\psi}} \left\{ \sum_i \sum_j \left| \nabla \tilde{\boldsymbol{\psi}}(i,j) - \hat{\nabla} \boldsymbol{\psi}(i,j) \right|^2 \right\} \tag{8}$$

where $\hat{\psi}(\cdot)$ is the unknown unwrapped phase field. We may stress that, with respect to the branch-cut approaches, in these cases the solution will be no longer congruent with the original interferometric phase $\varphi(\cdot)$, that is $\langle \psi(i,j) \rangle_{-\pi,\pi} \neq \varphi(i,j)$.

Equation (7) represents a variational problem, whose Euler equation is the Poisson one

$$\nabla^2 \tilde{\psi}(i,j) = \nabla \cdot \nabla \tilde{\psi}(i,j) = \Delta_x \left(\langle \Delta_x \psi(i,j) \rangle_{-\pi,\pi} \right) + \Delta_y \left(\langle \Delta_y \psi(i,j) \rangle_{-\pi,\pi} \right) \qquad (9)$$

under the Neumann boundary condition, which can be finally solved by using simple cosine or Fourier transform filtering [70].

One major difference between the residue-cut and least-squares solutions is that in the residue-cut approach only integral numbers of cycles are added to the measurements to produce the result. Conversely, in the least-squares approach, any value may be added to ensure smoothness and continuity in the solution, thus the spatial error distribution may differ between the approaches, and the relative merits of each method must be determined depending on the application.

Least-squares methods are very computationally efficient when they make use of fast Fourier transform techniques [54,71] but the resulting unwrapping is not very accurate, because they tend to spread the errors that are instead concentrated on a limited set of points. To overcome this problem a weighting of the wrapped phase can be useful. However, the proposed, weighted least squares algorithms [54-72] are iterative and not as efficient as the unweighted ones and the result accuracy strongly depends on the weighting mask we used.

Several other approaches, which can be found in the bibliography at the end of this work have also been investigated but, in the following, we will address the capability of one of these, known as the minimum cost flow phase unwrapping technique, developed for the two-dimensional case by Costantini [55,56], belonging to the branch-cuts PhU algorithm class.

3.2 Minimum Cost Flow Algorithm

Within the branch-cuts phase unwrapping algorithms an easy and fast algorithm is based on a solution of an equivalent minimum cost flow network and will be here addressed.

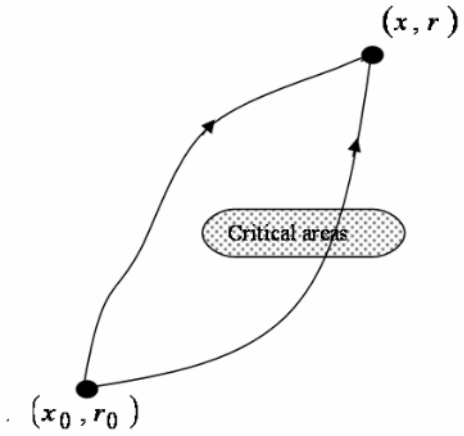

Figure 3. 2 The representation of the key point of the Phase Unwrapping problems. To connect two points on the space it is possible to follow different paths but, any of these, could cross critical areas where the wrapped phase differences are greater than p, thus implying that a correct procedure should be able to individuate these areas in such a way that only paths not crossing them are used to integrate the wrapped phase differences.

Branch-cut methods are based on the integration of the estimated neighboring pixel differences of the unwrapped phase along conservative paths, thus avoiding the regions where these estimated differences are inconsistent (see Figure 3.2). The problem of building cuts delimiting these regions is very difficult and the resulting phase unwrapping algorithm is very computationally expensive. However, we may exploit the fact that the neighboring pixel differences of the unwrapped phases are estimated with possibly an error which is an integer multiple of $\pm 2\pi$. This circumstance allows formulating the phase unwrapping problem as the one of minimizing the weighted deviations between the estimated and the unknown neighboring pixel differences of the unwrapped phases with the constraint that the deviations must be integer multiple of $\pm 2\pi$. With this constraint, the unwrapping results will not depend critically on the weighting mask we used, and errors are prevented to spread.

Minimization problems with integer variables are usually computationally very complex. However, recognizing the network structure underlying the phase unwrapping problem, it makes possible to employ very efficient strategies for its solution. In fact, the problem can be equated to the one of finding the minimum cost flow on a network, for the solution of which there are very efficient algorithms.

In order to explain its basic principles and clarify how it can be performed, we refer to the unknown, unwrapped phase field and we impose that the result is consistent, thus requiring the irrotational property of this field

$$\begin{aligned}&\nabla\times\nabla\psi(i,j)=\Delta_x\left(\Delta_y\psi(i,j)\right)-\Delta_y\left(\Delta_x\psi(i,j)\right)=\\&=\Delta_x\psi(i,j)+\Delta_y\psi(i+1,j)-\Delta_x\psi(i,j+1)-\Delta_y\psi(i,j)=0\end{aligned}\tag{10}$$

Obviously, we can also express each term of equation (10) with respect to the wrapped phase derivates by introducing, for each phase term, a corresponding, unknown 2π-multiple term, as follows

$$\begin{aligned}\Delta_x\psi(i,j)&=\left\langle\Delta_x\psi(i,j)\right\rangle_{-\pi,\pi}+2\pi K_x(i,j)\\\Delta_y\psi(i+1,j)&=\left\langle\Delta_y\psi(i+1,j)\right\rangle_{-\pi,\pi}+2\pi K_y(i+1,j)\\\Delta_x\psi(i,j+1)&=\left\langle\Delta_x\psi(i,j+1)\right\rangle_{-\pi,\pi}+2\pi K_x(i,j+1)\\\Delta_y\psi(i,j)&=\left\langle\Delta_y\psi(i,j)\right\rangle_{-\pi,\pi}+2\pi K_y(i,j)\end{aligned}\tag{11}$$

These relations, properly substituted in the equation (10) and taking account of the equation 11, finally lead to the following equation

$$K_x(i,j)+K_y(i+1,j)-K_x(i,j+1)-K_y(i,j)=-\frac{r(i,j)}{2\pi}\tag{12}$$

that relates the $K_q(i,j)\quad q\in[x,y]$ unknown terms to the measurable residues. At this stage, the phase unwrapping problem can be formulated as the searching of the K terms satisfying the constraints (11), which solve the following minimization problem

$$\min_{K_x,K_y}\left\{\sum_i\sum_j c_x(i,j)\left|K_x(i,j)\right|+\sum_i\sum_j c_y(i,j)\left|K_y(i,j)\right|\right\}\tag{13}$$

wherein $c(\cdot)$ are the so-called cost functions allowing us to individuate areas where the location of branch-cuts is likely or unlikely. It is easy to verify that if they were chosen to be constant, the problem (13) would be equivalent to search for the minimum total cut-line length. Cost functions are essentially expressed as a function of the estimated local interferogram quality (by exploiting the spatial coherence, or the phase gradient density or other properly identified quality factors). The problem given in (13) is a non-linear minimization problem with integer variables, and, if the following change of variables is considered

$$\begin{aligned} K_x^-(i,j) &= \min\left[0, K_x(i,j)\right] \\ K_x^+(i,j) &= \max\left[0, K_x(i,j)\right] \\ K_y^-(i,j) &= \min\left[0, K_y(i,j)\right] \\ K_y^+(i,j) &= \max\left[0, K_y(i,j)\right] \end{aligned} \tag{14}$$

it can be re-formulated via two different linear problem, as follows

$$\min_{K_x K_y}\left\{\sum_i\sum_j \begin{matrix}\left[c_x(i,j)K_x^+(i,j)+c_y(i,j)K_y^+(i,j)\right] \\ +\left[c_x(i,j)K_x^-(i,j)+c_y(i,j)K_y^-(i,j)\right]\end{matrix}\right\} \tag{15}$$

It can be seen that the problem stated in (15) can be transformed so that it defines a minimum cost flow problem on a network (see Figure 3.3), with the new variables representing the net flow running along the network arcs. Once the network has been solved, the solutions in terms of the 2π-multiple integer functions will be so expressed

$$\begin{aligned} K_x(i,j) &= K_x^+(i,j) - K_x^-(i,j) \\ K_y(i,j) &= K_y^+(i,j) - K_y^-(i,j) \end{aligned} \tag{16}$$

and, finally

$$\nabla\psi = \hat{\nabla}\psi + 2\pi K \tag{17}$$

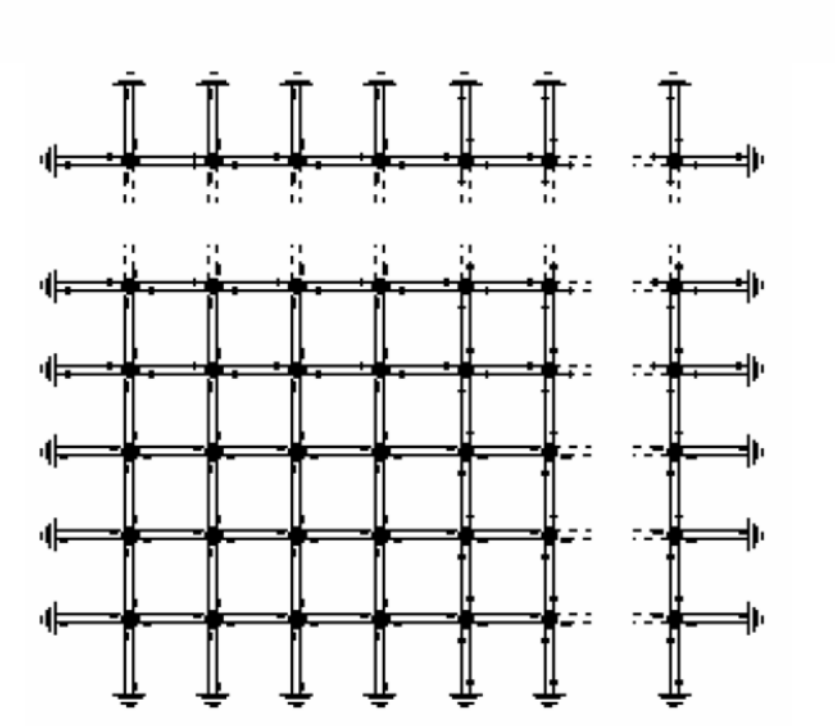

Figure 3. 3 The equivalent network to be solved to argue on the 2p-multiples integer needed to reconstruct a conservative phase field. The network nodes are associated to each residue-cut and the bidirectional arcs are related to the phase differences arcs.

The full phase gradient vector allows us to individuate the phase associated to each pixels because we can choose a generic spatial path to integrate it, starting from the position of the selected reference point in space whit respect to which the relative deformation must be referred (see chapter two).

3.3 Extended Minimum Cost Flow (EMCF) algorithm

This section will be focused on the presentation of the Extended Minimum Cost Flow technique. Before discussing the characteristics of the proposed approach, some considerations about the MCF technique are now

in order. The original minimum cost flow algorithm, thought to be applied to a regular spatial grid, has been subsequently changed in order to deal with sparse data [56] and, consequently, the grid of the investigated samples is chosen to be relevant to the coherent pixels of the D-InSAR interferograms, while the Delaunay triangulation is used to define the neighboring points and the elementary cycles in the set of the identified coherent sparse pixels.

The possibility to extend this approach to the three-dimensional case, in order to simultaneously unwrap an interferometric sequence, has been already investigated in [73]. However, in this case the problem could not be formulated in terms of network minimum cost flow procedures. Accordingly, no computationally efficient codes are available and, therefore, the overall unwrapping process can be extremely time-consuming, particularly for long interferogram sequences.

The proposed unwrapping solution, which has been already described in [74], in addition to the spatial characteristics of each D-InSAR interferogram, also exploits the temporal relationships among a properly selected interferogram sequence, thus allowing us to improve the performance of the original MCF technique [56].

3.3.1 Introduction to the algorithm

The starting point of our approach, mostly oriented to deformation time-series generation, is the computation of two Delaunay triangulations. The former is relevant to the SAR data acquisitions distribution in the so-called "Temporal/Perpendicular baseline" plane and allows us to identify the D-InSAR interferograms sequence to be computed; the latter is carried out in the Azimuth/Range plane and involves the coherent pixels common to the interferograms within the sequence. The unwrapping operation of the overall data set is then performed via a two-step processing procedure: first of all, we identify all the segments of the computed "spatial" triangles (i.e., the arcs connecting the coherent neighboring pixels in the $A_z \times R_g$ plane) and, for each of these, we carry out a "temporal" PhU step by applying the MCF technique to the grid relevant to the $T \times B_\perp$ plane. The second step uses, for each arc, the previously computed unwrapped phases as a starting point for the subsequent spatial unwrapping operation, performed on each single interferogram; again the standard MCF network programming technique is applied and, in this case, we use the "costs" of the previous solutions to set the weights associated with the single arcs involved in the spatial unwrapping. Overall, the basic rationale of the procedure is quite simple: to exploit the temporal relationships among the computed multi-temporal interferograms to bootstrap the subsequent spatial unwrapping operation.

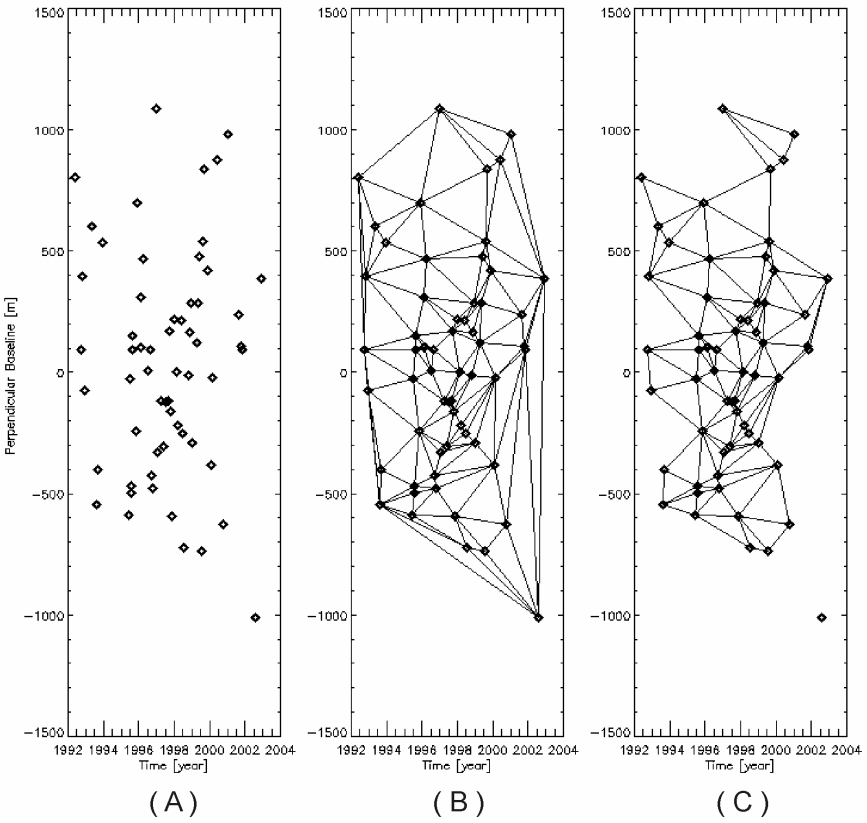

Figure 3. 4 SAR data representation in the temporal/perpendicular baseline plane for the ERS SAR data analyzed in the following experiments. (A) SAR image distribution. (B) Delaunay triangulation. (C) Triangulation after removal of triangles with sides characterized by spatial and/or temporal baseline values exceeding the selected thresholds (corresponding in our experiments to 300 m and 1500 days, respectively).

We remark that the presented approach is focused on multilook interferograms. Moreover, the possibility to apply the MCF network programming algorithm to both the temporal and spatial unwrapping steps leads to a computationally efficient procedure.

3.3.2 D-InSAR interferogram selection

Let us start our analysis by investigating the generation process of the interferograms needed for the algorithm implementation discussed in the

following sections. Accordingly, we consider a set of N+1 independent SAR images of the same area, acquired at the ordered $(t_0, t_1, ..., t_N)$ times. We also assume that each image is co-registered with respect to a reference one, with respect to which we may compute the temporal and spatial (perpendicular) baseline components $t_i - t_{master}, i = 0, ..., N$ and $b_{\perp i}, i = 0, ..., N$, respectively, being t_{master} the image reference time. Accordingly, each SAR image can be represented by a point in the $T \times B_\perp$ plane (see Figure 3.4A) where we may also compute a Delaunay triangulation (see Figure 3.4B). Note that, in order to generate this triangulation, we need to define a ratio between the perpendicular and temporal baseline axis units. In our analysis we assume that this ratio is equal to $\delta T / \delta b_\perp$, wherein δT and $\delta b_\perp$ represent the maximum allowed temporal and spatial baselines, respectively, that have been introduced in order to avoid the generation of interferograms strongly corrupted by decorrelation phenomena [21]. Note that the selection of the factor $\delta T / \delta b_\perp$ is not a very critical issue; indeed, within a realistic range of variation of this ratio, say in the interval between 1 and 5, the corresponding triangulation in the plane typically does not significantly change as shown in the analysis presented in the Appendix C. Note also that, each arc connecting two different points in the $T \times B_\perp$ plane, say $P_i \equiv (t_i, b_{\perp i})$ and $P_j \equiv (t_j, b_{\perp j})$, identifies a corresponding D-InSAR data pair. Therefore, as a result of this triangulation, we finally identify a sequence of interferograms for which $\Delta \mathbf{t} = (\Delta t_0, \Delta t_1, ..., \Delta t_{M-1})$ and $\Delta b_\perp = (\Delta b_{\perp 0}, \Delta b_{\perp 1}, ..., \Delta b_{\perp M-1})$ represent the associated temporal and perpendicular baseline vectors, respectively, while M is the overall number of interferograms. As a final issue, we have defined for each arc of our triangulation (i.e., for each selected interferometric data pair) a normalized length expressed as follows:

$$L_{i,j} = \sqrt{\left(\frac{t_i - t_j}{\delta T}\right)^2 + \left(\frac{b_{\perp i} - b_{\perp j}}{\delta b_\perp}\right)^2} \tag{18}$$

wherein δT and $\delta b_\perp$ are our normalization factors.

Despite our constraints on the maximum allowed baseline extensions, we remark that the obtained triangulation may involve arcs relevant to data pairs whose baselines exceed the assumed maxima, thus potentially leading to generate interferograms strongly decorrelated. To avoid these effects without loosing our triangulation representation, we may remove all the triangles involving arcs with too large baselines, as shown in Figure 3.4C. Equivalently, we may also remove the triangles corresponding to interferograms including data pairs with large Doppler centroid [15]

differences; this is often the case for interferograms involving ERS data acquired after 2000, i.e., following the gyroscopes failure events [41]. Note that this triangles removal step may lead to discarding some acquisitions and/or to the generation of more than one independent subset of triangles, i.e., to a data representation consistent with the one described in the D-InSAR Small Baseline Subset (SBAS) procedure [39]. Therefore, the compatibility between this data organization and the one exploited in the SBAS technique is clearly evident.

Following the identification of the final triangulation in the $T \times B_{\perp}$ plane, the computation of the D-InSAR interferogram sequence, referred hereafter to as $\varphi = (\varphi_0, \varphi_1, ..., \varphi_{M-1})$, is performed. At this stage, we can generate the "mask" of the pixels in the $A_z \times R_g$ plane that are considered coherent within the generated sequence. This mask can be obtained, for instance, by considering those pixels with an estimated coherence value greater than a selected threshold, which are common to a part or even to the entire interferogram sequence. The mask can be also obtained by searching for the set of pixels with a relatively stable phase pattern. For this purpose, we can refer to a generic triangle in the $T \times B_{\perp}$ plane (whose sides are labeled to as α, β, γ, respectively) and evaluate the corresponding curl of the wrapped phase differences

$$C_{\alpha,\beta,\gamma} = \Delta\phi_{\alpha} + \Delta\phi_{\beta} + \Delta\phi_{\gamma} = 2\pi h_{\alpha,\beta,\gamma} + \Delta n_{\alpha,\beta,\gamma} \tag{19}$$

wherein $h_{\alpha,\beta,\gamma}$ is an integer number and $\Delta n_{\alpha,\beta,\gamma}$ accounts for the fact that the multi-looked phase differences are spread around the corresponding expectation values. It is easy to recognize that the larger is the dispersion of the measured phase around its expectation value (i.e. the spatial coherence value is little enough) the larger is the $\Delta n_{\alpha,\beta,\gamma}$ term, thus suggesting us to search for the pixels for which the norm of the vector $\Delta \mathbf{n} = \left(\Delta n_0, \Delta n_1, ..., \Delta n_{N_{Tr}-1}\right)$ is smaller than a given threshold (being N_{Tr} the number of the triangles involved in the considered Delaunay triangulation in the $T \times B_{\perp}$ plane) or, equivalently, for which the following factor

$$\frac{\left|\sum_{k=1}^{N_{Tr}} \exp\left[j\Delta n_k\right]\right|}{N_{Tr}} \tag{20}$$

is larger than a selected threshold.

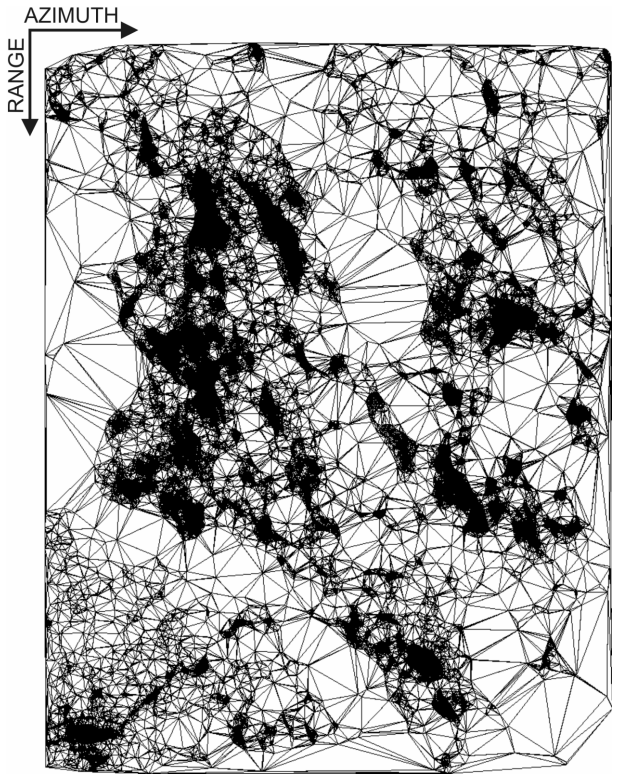

Figure 3. 5 Delaunay triangulation in the azimuth/range plane involving the set of spatially coherent pixels (in black) relevant to the SAR data analyzed in the following experiments.

Accordingly, as a final step, we compute a second Delaunay triangulation which involves the arcs connecting the neighboring pixels of the computed mask in the $A_z \times R_g$ plane, as shown in the example of Figure 3.5.

3.3.3 Extended MCF approach theory

The presented PhU procedure is based on a two-step processing approach that benefits of the information available from both the $T \times B_\perp$ and $A_z \times R_g$ grids. In particular, the key idea is to carry out first, for each arc connecting neighboring pixels of the $A_z \times R_g$ grid (see Figure 3.5), a "temporal" unwrapping operation which implies the basic MCF approach. The second step relies on the use of these results as a starting point for the

"spatial" unwrapping performed on each single interferogram. The key issues of these two processing steps are described in the following analysis which is focused on the use of multilook interferograms. In particular, this section is organized as follows: first of all, we briefly describe the main aspects of the original Minimum Cost Flow approach; subsequently, we address the main characteristics of the temporal and spatial PhU steps, respectively.

3.3.3.1 Sparse-Grid-MCF approach

Although an extensive analysis on the basic principles of the MCF PhU procedure can be found in [55,56], let us briefly summarize which are the modifications with respect to the original approach to take account of a sparse data grid.

For sake of simplicity, we refer to a generic D-InSAR pair and assume that $\tilde{\varphi}$ and $\tilde{\psi}$ represent the wrapped and unwrapped phase interferograms, respectively. The method benefits of the relationships existing between the phase differences of pixel pairs relevant to the wrapped and unwrapped signals. In particular, if we consider the spatial arc connecting the generic A and B pixel pair in the $A_z \times R_g$ plane, the unknown, unwrapped phase difference $\Delta\tilde{\psi}_{AB}$ can be expressed as follows

$$\begin{aligned}\Delta\tilde{\psi}_{AB} &= \tilde{\psi}(A) - \tilde{\psi}(B) = \left\langle \tilde{\varphi}(A) - \tilde{\varphi}(B) \right\rangle_{-\pi,\pi} + 2\pi H_{AB} = \\ &= \Delta\tilde{\varphi}_{AB} + 2\pi H_{AB}\end{aligned} \tag{21}$$

wherein $\Delta\tilde{\varphi}_{AB}$ is the phase difference computed from the wrapped data and H_{AB} is the unknown integer number we want to estimate. Therefore, we may compute a Delaunay triangulation in the $A_z \times R_g$ plane (see, for instance, the example shown in Figure 3.5) in order to define a set of elementary cycles relevant to the coherent pixels only, and we may impose the irrotational property for the phase gradient, in a discrete space, of $\tilde{\psi}$. By referring to a generic triangle in the $A_z \times R_g$ plane (whose arcs are labeled to as α, β and γ, respectively), this is equivalent to impose the following constraint

$$\Delta\tilde{\psi}_{\alpha} + \Delta\tilde{\psi}_{\beta} + \Delta\tilde{\psi}_{\gamma} = 0 \tag{22}$$

which can be also expressed, by taking into account of the equation (21), as follows

$$H_\alpha + H_\alpha + H_\alpha = -\frac{1}{2\pi}\left[\Delta\tilde{\psi}_\alpha + \Delta\tilde{\psi}_\beta + \Delta\tilde{\psi}_\gamma\right] \tag{23}$$

At this stage, the PhU problem can be solved, as done for the original case, in a very efficient way by recognizing that a network structure underlines it and, by searching for the network minimum cost flow solution. This can be carried out, by choosing the weighted L_1 norm for the error criterion, via the following minimization problem

$$\min_{H_p}\left\{\sum_{p=0}^{N_A-1} w_p \cdot \left|H_p\right|\right\} \tag{24}$$

subject to the constraints (21), wherein the $\min\{\cdot\}$ symbol stands for the minimization operation, N_A is the overall number of arcs relevant to the Delaunay triangulation and $\mathbf{w} = \left(w_0, w_1, ..., w_{N_A-1}\right)$ set the weights relevant to the weighted L_1 norm.

3.3.3.2 Temporal Unwrapping step

Let us start our discussion by reconsidering the spatial Delaunay triangulation in the $A_z \times R_g$ plane (see for example the one in Figure. 3.5) and to assume that, for each given arc, $\boldsymbol{\delta\varphi} = \left(\delta\varphi_0, \delta\varphi_1, ..., \delta\varphi_{M-1}\right)$ and $\boldsymbol{\delta\psi} = \left(\delta\psi_0, \delta\psi_1, ..., \delta\psi_{M-1}\right)$ are the (measured) wrapped and (unknown) unwrapped D-InSAR phase gradient vectors of the D-InSAR interferometric sequence, respectively. Moreover, in order to facilitate the procedure, we observe that a profitably model of the unknown unwrapped phase gradient vectors can be considered as follows [39,75]

$$\mathbf{m}\left(\Delta z, \Delta v\right) \approx \frac{4\pi}{\lambda} \cdot \left(\frac{\boldsymbol{\Delta b}_\perp}{r \cdot \sin\left(\vartheta\right)} \cdot \Delta z + \boldsymbol{\Delta t} \cdot \Delta v\right) \tag{25}$$

wherein Δz accounts for the error in the knowledge of the scene topography while Δv for the deformation velocity variations along the considered spatial arc. Moreover, r represents the sensor to target distance, λ the transmitted signal central wavelength and ϑ the incidence angle. Note that, because of the spatially correlated behavior of the atmospheric artifacts [75], we have assumed in (25) that they do not contribute to the model $\mathbf{m}(\cdot)$.

Since the wrapped phases differ from the unwrapped ones by 2π-integer multiples only, the D-InSAR unwrapped vector can be expressed as follows

$$\boldsymbol{\delta\psi} = \mathbf{m} + \left\langle \boldsymbol{\delta\varphi} - \mathbf{m} \right\rangle_{-\pi,\pi} + 2\pi\mathbf{K} = \boldsymbol{\delta\chi} + 2\pi\mathbf{K} \tag{26}$$

wherein $\mathbf{K}$ is the 2π-integer multiple vector and

$$\boldsymbol{\delta\chi} = \mathbf{m} + \left\langle \boldsymbol{\delta\varphi} - \mathbf{m} \right\rangle_{-\pi,\pi} \tag{27}$$

represents the phase component, for each considered arc, related to the computed model $\mathbf{m}(\cdot)$ and to the measured phase contribution $\boldsymbol{\delta\varphi}$.

Note also that, for sake of simplicity, the explicit dependence of $\mathbf{m}(\cdot)$ on the Δz and Δv factors has been neglected in (26) and (27); this notation will be maintained hereafter.

At this stage, we can evaluate for each $(\Delta z, \Delta v)$ pair, the unknown vector $\mathbf{K}$ in (26) by applying the basic MCF technique (summarized in the previous section) to the grid. In particular, we search in this case for the solution of the following minimization problem

$$\min_{k_j}\left\{ C = \sum_{j=0}^{M-1} \left| k_j \right| \right\} \tag{28}$$

subject to the constraints

$$k_\alpha + k_\beta + k_\gamma = -\text{round}\left[\frac{\delta\chi_\alpha + \delta\chi_\beta + \delta\chi_\gamma}{2\pi} \right] \tag{29}$$

wherein k_j is the j-th element of the $\mathbf{K}$ vector in (26). Moreover, the $round[\cdot]$ symbol represents the operation of approximation to the nearest integer number and the constraints in (29) are expressed in terms of a generic triangle in the $TxB_\perp$ plane whose arcs have been labeled as α, β and γ, respectively. We explicitly observe that the round operator is needed to work, also in this case, with integer variables because, as explained in the introduction, the multilook operation has introduced additional terms Δn on the curls expression. We remark that for each $(\Delta z, \Delta v)$ pair we will have a different solution, characterized by its overall network cost

$$C = \sum_{j=0}^{M-1} \left| k_j \right| \tag{30}$$

Accordingly, by exploring different values of the $(\Delta z, \Delta v)$ pair and the corresponding model $\mathbf{m}(\cdot)$ in (27), we may finally identify the unknown vector

$$\boldsymbol{\delta\psi}_{\mathbf{opt}} = \boldsymbol{\delta\chi}_{\mathbf{opt}} + 2\pi\mathbf{K}_{\mathbf{opt}} \tag{31}$$

characterized by the "overall minimum" cost:

$$C_{\min} = \sum_{j=0}^{M-1} \left| k_{opt_j} \right| \tag{32}$$

wherein $\boldsymbol{\delta\chi}_{\mathbf{opt}}$ and $\mathbf{K}_{\mathbf{opt}}$ are the vectors (whose k_{opt_j} and $\delta\chi_{opt_j}$ are the j-th components, respectively) evaluated in the minimum cost condition. Accordingly, $\boldsymbol{\delta\psi}_{\mathbf{opt}}$ in (31) will represent our estimate of the unwrapped vector for the considered arc.

3.3.3.3 Spatial Unwrapping step

For what concerns this operation, it exploits the unwrapped DInSAR phase differences computed via the previous temporal PhU step as a starting point for the spatial unwrapping operation. This second step is carried out on the single interferograms through the application of the MCF unwrapping technique. Moreover, in this case, we may use the minimum costs of the solutions achieved in the $T \times B_{\perp}$ plane, in order to set the weights w_p, associated to the single arcs. In particular, since the weights represent the confidence on the correctness of the achieved solution, we can reasonably assume that, for each spatial arc, the smaller is the temporal network cost, the larger should be the weight applied within the minimization step involved in the spatial unwrapping. Accordingly, an inverse exponential relationship between the temporal network cost and the corresponding spatial weight w_p has been chosen

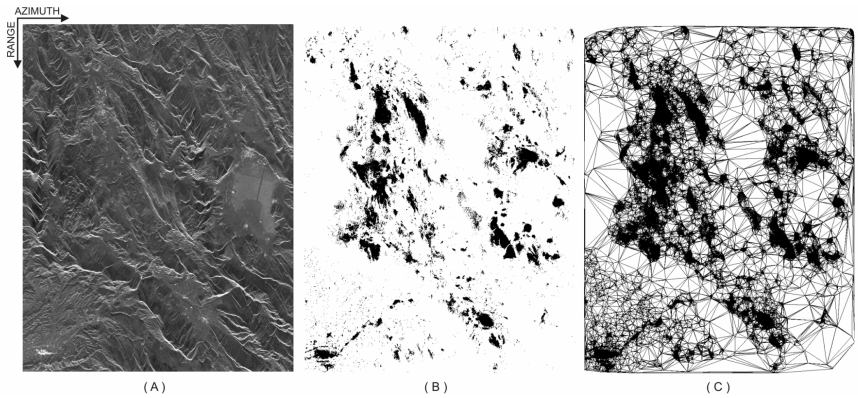

Figure 3. 6 SAR products relevant to the investigated area and represented in the azimuth/range plane. (a) Multilook image. (b) Mask of the spatially coherent pixels (in black) defining the investigated spatial grid and the corresponding (c) spatial Delaunay triangulation.

$$w_p = \begin{cases} \dfrac{2^S}{2^{C_{\min}}} & C_{\min} < \rho \\ 1 & C_{\min} \geq \rho \end{cases} \tag{33}$$

wherein 2^S represents the maximum allowed weight, $C_{\min}$ is the minimum temporal cost, with $C_{\min} < S$, and ρ is a threshold value that, based on experimental results, is typically set not greater than 5% of the total number of interferograms M.

Following the implementation of this spatial unwrapping step, carried out for each interferogram, the unwrapped phase can be easily retrieved via the integration of the computed spatial gradients.

3.3.3.4 Algorithm validation

In order to investigate the performance of the proposed unwrapping approach, a number of experiments, involving both real and simulated data, were carried out. The considered real data set is relevant to the Central Apennines (Abruzzi, Italy) area, see the multilook image shown in Figure 3.6A , and is composed by 58 acquisitions collected by the ERS1/2 sensors between August 1992 and October 2002, see Table 3.1, that are relevant to the track 308 and frame 2755. The space/time data distribution is the one depicted in Figure 3.4A while the final triangulation is shown in Figure

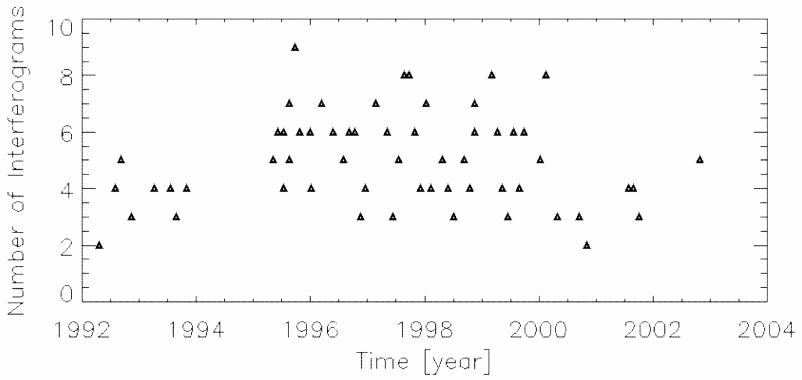

Figure 3. 7 Number of occurrences for each SAR image within the generated interferogram data set.

3.4C; the latter has been obtained by imposing a maximum spatial and temporal baseline value of 300 m and 1500 days, respectively, and a doppler centroid separation, between the images pair, not larger than 1000 Hz. We further remark that, instead of imposing separate constraints on the maximum allowed spatial and temporal baselines, we could alternatively consider an upper limit for the normalized arc length. Moreover, the value of the imposed constraints could be also changed depending on the characteristics of the investigated zone; for instance, larger values could be considered in presence of highly coherent areas as for the case of urbanized zones.

Following the triangulation step shown in Figure 3.4C, we have identified the sequence of D-InSAR interferograms to be generated for implementing the proposed algorithm. In particular, we have computed 145 interferograms with 4 looks in the range direction and 20 looks in the azimuth one, having a pixel spacing of about 90 x 90m. Note that the number of interferograms generated from each SAR image is dependent on the result of the Delaunay triangulation within the $T \times B_{\perp}$ plane. In this case, it is evident that acquisitions relevant to the triangulation boundaries are characterized by fewer arcs, i.e., are involved in a smaller number of interferograms; obviously, this effect becomes less significant when increasing the number of SAR acquisitions. For what concerns our data set, we present in Figure 3.7 the plot showing the number of appearances of each SAR image within the interferogram data set; note that only two acquisitions contribute to two interferograms only. Moreover, we also present in Figure

3.8 the distribution of the temporal and spatial baselines obtained by using our interferogram selection based on the Delaunay triangulation. We remark that, within the limits we defined as maximum baselines, the interferogram distribution is rather uniform, which is a relevant issue within the DInSAR scenarios.

Based on the computed interferograms we have generated the coherence mask shown in Figure 3.6B, i.e., the mask of the pixels that are considered coherent in our sequence of multilook interferograms. In our case they have been selected by identifying the pixels that have a coherence, estimated in a box of 4 pixels in the range direction and 20 pixels in the azimuth one, greater than 0.35 in at least the 30% of the interferograms. Based on the mask shown in Figure 3.6B, the spatial triangulation has been generated, see Figure 3.6C We remark that the selection of this Abruzzi test site area is related to the difficulty in the unwrapping operation of the relevant interferograms caused by the presence of strong decorrelation phenomena.

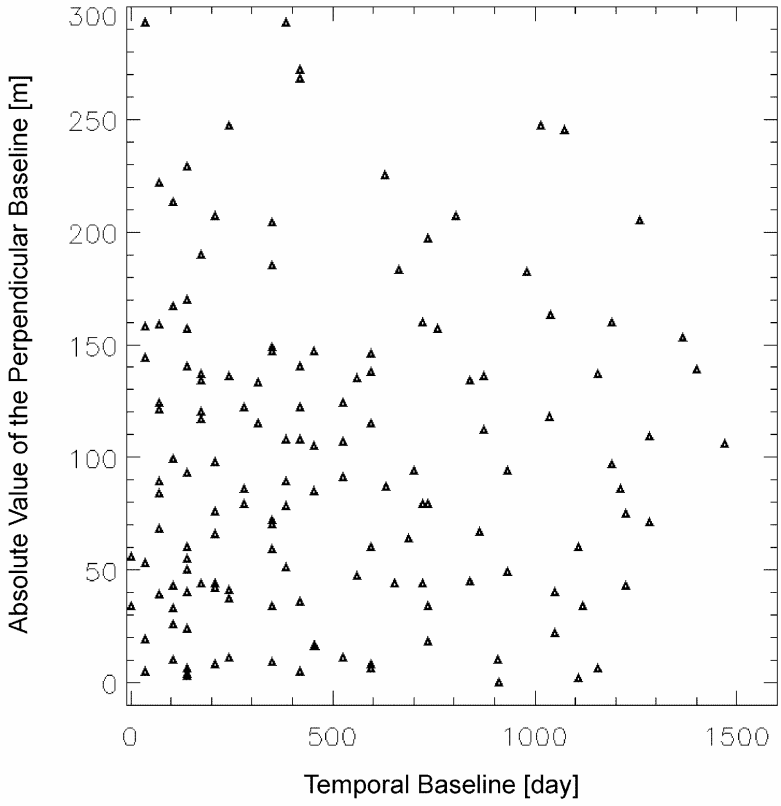

Figure 3. 8 Distribution of the temporal and spatial baselines relevant to the generated interferogram data set.

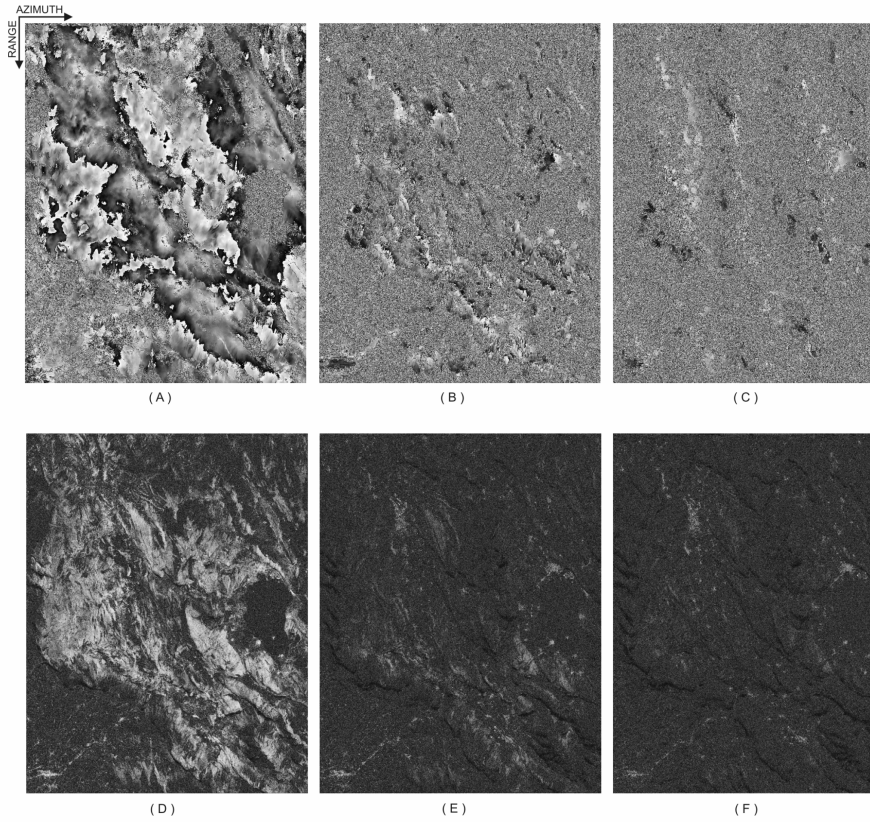

Figure 3. 9 Examples of the computed D-InSAR interferograms and of the corresponding coherence maps. (a) and (b) have been computed from the ERS data pair acquired on July 15, 1997 and September 23, 1997, respectively. (b) and (e) have been computed from the ERS data pair acquired on April 6, 1999 and September 28, 1999, respectively. (c) and (f) have been computed from the ERS data pair acquired on October 28, 1997 and January 11, 2000, respectively.

To give an idea of these effects we present in Figure 3.9 a selection of computed interferograms: it is evident that the impact of the decorrelation effects can be very strong.

Before discussing in details the results achieved on the considered real SAR data, we prefer to start our analysis with some simulations that represent controlled experiments allowing a direct assessment of the

algorithm performance. To this end we have retained both the $A_z \times R_g$ and $T \times B_\perp$ triangulations, respectively. Moreover, the same interferogram sequence generated for the real data set has been produced in the simulated experiments but, by exploiting the High Pass (HP) spatial components of a Digital Elevation Model (DEM) of the area and by introducing a deformation parametric model. In particular the j-th interferogram of the simulated D-InSAR sequence, say φ_{sj}, has the following expression

$$\varphi_{sj} = \frac{4\pi}{\lambda} \cdot \left[\frac{\Delta b_{\perp j}}{\mathrm{r} \cdot \sin(\vartheta)} \cdot \mathrm{h} + \left(\Delta \mathrm{t_j} \cdot vel + \frac{1}{2} \cdot \Delta \mathrm{t_j^2} \cdot acc \right) \right], \ \mathrm{j} = 0,...,\mathrm{M}-1 \tag{34}$$

wherein the first term represents the topographic phase contribution depending on the DEM height h, while the vel and acc factors are the velocity and acceleration model terms, respectively, the latter representing a significant deviation from the assumed model $\mathbf{m}(\cdot)$ Moreover, in our experiments we also assumed that both the simulated deformation components had a Gaussian spatial shape, as shown in Figure 3.10 wherein both the masked and unmasked data are presented.

In order to investigate the algorithm performances on the simulated data we unwrapped the generated interferogram sequence both via the original and the extended MCF technique; obviously, the former has been independently applied to each single interferogram. In the performed experiments a comparison between the original and the unwrapped phases is directly possible. As a result of our analysis we present in Figures 3.11A, 3.11B and 3.11C the percentage, for each interferogram, of correctly unwrapped pixels of the mask shown in Figure 3.6B, obtained by applying the original MCF technique and considering on the horizontal axis the spatial and temporal baselines and the normalized arc length, respectively. Moreover, the results achieved via the extended MCF procedure are shown in Figure 3.11D, where the horizontal axis is relevant to the normalized arc length. The results presented in Figures 11A, 11B and 11C clearly show that, for the original MCF approach, an increase of the spatial and/or of the temporal baseline (thus of the normalized arc length) may lead to significant degradations of the achieved reconstruction. On the contrary, the extended MCF approach guarantees a very good retrieval, as shown in Figure 3.11D. For what concerns the computational aspects, we remark that, on a PC equipped with an AMD Athlon MP2600+ processor, the basic MCF unwrapping procedure required about 75 min for unwrapping the overall interferogram sequence, while the extended MCF algorithm needed about 225 min. We remark that this computational increase is mostly related to the

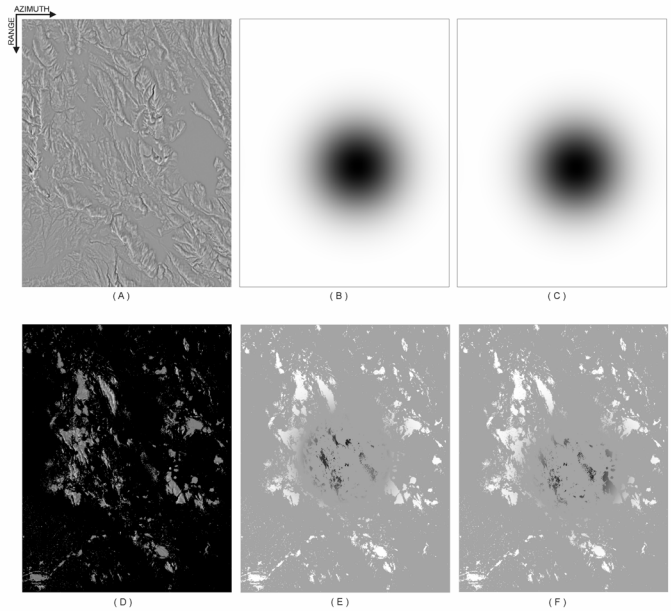

Figure 3. 10 Maps relevant to three components of the model presented in () and used to generate the simulated D-InSAR interferograms. (a) and (d) are the unmasked and masked topography maps, respectively. (b) and (e) are the unmasked and masked velocity patterns, respectively. (c) and (f) are the unmasked and masked acceleration patterns, respectively. Note that the position of the minima of the simulated velocity and acceleration patterns are relatively shifted by 100 pixels in both directions.

evaluation of the model function $\mathbf{m}(\cdot)$ within the temporal unwrapping step. Indeed, this operation is carried out via an exhaustive search, with a limited spacing, of the Δz and Δv factors within the intervals (-100,100) m and (-5,5) cm/year, respectively. Obviously, the availability of an a-priori information on the Δz and Δv terms would lead to a significant computational improvement of the extended MCF PhU algorithm performance.

As a final test on our simulated data, we investigated the quality of the retrieved solution if the model adjustment step, relevant to m, is not implemented. In this case the required computing time reduced to about 80 min. However, the achieved results presented in Figure 3.11E, clearly show that the computational reduction is "paid" with a considerable degradation of the obtained unwrapped data with respect to those generated through the extended MCF approach, the latter shown in Figure 3.11D.

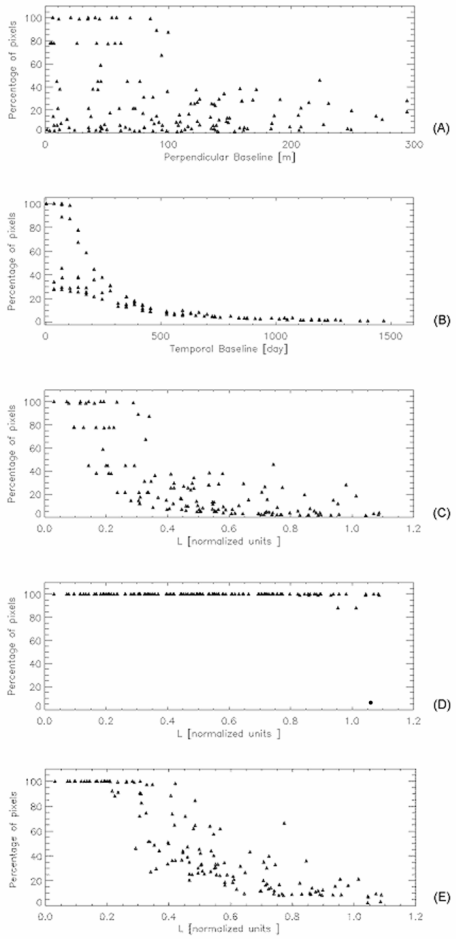

Figure 3. 11 Percentage of the coherent pixels of each interferogram that has been correctly unwrapped. (a) Results obtained by applying the original MCF approach with the horizontal axis relevant to the perpendicular baseline; (b) same as (a) but with the horizontal axis relevant to the temporal baseline; (c) same as (a) but with the horizontal axis relevant to the normalized arc length **L** defined in (). (d) Results obtained by applying the extended MCF approach with the horizontal axis relevant to the normalized arc length L. (e) Results obtained by applying the extended MCF approach but without the model adjustment step; the horizontal axis is relevant to the normalized arc length **L**.

Let us now move to the real data analysis; in this case the dimensions of the processed data set are the same of the simulated signals thus the

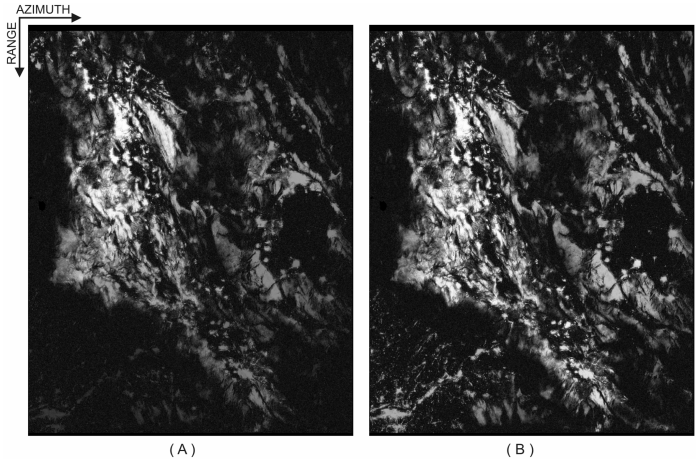

Figure 3. 12 Temporal coherence maps obtained from (a) the original and (b) the extended MCF unwrapping procedures, respectively.

computing requirements remained practically unchanged; on the contrary, we had now to define a quality index for our results. To achieve this task we decided to use the SBAS algorithm that, as previously stated, is fully compatible with the presented data representation and allows us to generate D-InSAR deformation time-series from a sequence of unwrapped multi-temporal interferograms. In particular, we considered the following strategy: first of all, we applied the SBAS procedure to both the unwrapped sequences computed via the original and the extended MCF algorithm; this allowed us to produce deformation time-series for each pixel of the mask shown in Figure 3.6B. Subsequently, we used the computed time-series (without any atmospheric filtering) and the estimated topographic errors to regenerate the original interferograms referred to as $\overline{\varphi} = \left(\overline{\varphi}_0, \overline{\varphi}_1, ..., \overline{\varphi}_{M-1}\right)$. At this stage, we use as quality index of the PhU retrieval, the temporal coherence factor defined for each pixel as follows (see also chapter two)

$$\gamma = \frac{\left| \sum_{p=0}^{M-1} \exp\left[j\left(\varphi_p - \overline{\varphi}_p\right)\right] \right|}{M}, \; 0 \le \gamma \le 1 \tag{35}$$

Note that for pixels where $\gamma \to 1$, we expect that no unwrapping errors are present, since a nearly perfect retrieval of the original phase has been

obtained. On the other hand, low values of γ will correspond to poorly unwrapped data. Following the application of the SBAS algorithm to the two unwrapped D-InSAR sequences, obtained through the original and the extended MCF technique, respectively, we have evaluated the temporal coherence map for both data set. The achieved results are shown in Figures 3.12A and 3.12B, respectively. The improvement of the coherence obtained through the application of the extended PhU algorithm is evident, particularly in the areas in the lower left and upper right corners of the map. To emphasize the achieved gain, the histograms relevant to these two results have been computed and superimposed in Figure 3.13A: again the obtained improvement is clear. In particular we remark that in this case we achieved an increase of about 60% for what concerns the number of pixels with a temporal coherence value greater than the selected threshold $\gamma = 0.7$, that is a typical value in D-InSAR applications [64,66].

As final point we have investigated the impact, on the unwrapping algorithm performance, of the $\mathbf{K}_{opt}$ vector component. To this end we have repeated the overall processing operation based on the extended MCF approach but assuming no 2π-integer correction, i.e., with $\mathbf{K}_{opt} = 0$; this implies we assumed $\boldsymbol{\delta\psi}_{opt} = \boldsymbol{\delta\chi}_{opt}$. The histogram of the computed new temporal coherence has been superimposed (see Figure 3.10B) to those shown in Figure 3.10A. The degradation of the achieved results is remarkable with respect to those of the overall extended MCF procedure; in particular, in this case we had a reduction of the number of coherent pixels with $\gamma \geq 0.7$, of about 30% with respect to the extended MCF results. This clearly indicates a significant impact of the 2π-integer correction component within the proposed unwrapping procedure.

3.4 Summary and conclusion

We have proposed a solution for extending the MCF phase unwrapping algorithm dealing with a sparse data grid, to process multi-temporal DInSAR interferograms for the generation of deformation time-series. The approach involves the computation of a properly chosen interferograms sequence and is based on the cascade of two main steps, both involving the use of the basic MCF technique. In particular, we identify first the arcs connecting neighboring coherent pixels of the Azimuth/Range grid and, for each of these; we estimate the unwrapped phase gradients via the MCF technique applied in the Temporal/Perpendicular baseline plane. These results are used to bootstrap the subsequent spatial unwrapping operation carried out on each

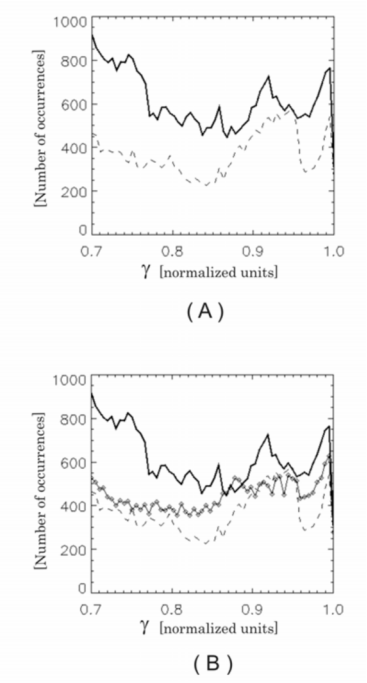

Figure 3. 13 Histograms of the temporal coherence maps. (a) The dashed line is related to the results obtained via the basic MCF approach; the continuous line is relevant to those achieved by using the extended MCF approach. (b) Same plots as in (a) with the superimposed diamond plot relevant to the results of the extended MCF approach implemented without 2π-multiple corrections, i.e. by assuming $\mathbf{K_{opt}=0}$ in Equation (31).

single interferogram via the conventional MCF approach. Presented results obtained on simulated and real data confirm the effectiveness of the approach. Moreover, we underline that the proposed solution is naturally compatible with the SBAS algorithm for the generation of deformation time-series. The implemented extension of the unwrapping procedure is based on the application of the network programming algorithm for both the temporal and spatial unwrapping steps. Accordingly, the overall approach is computationally efficient.

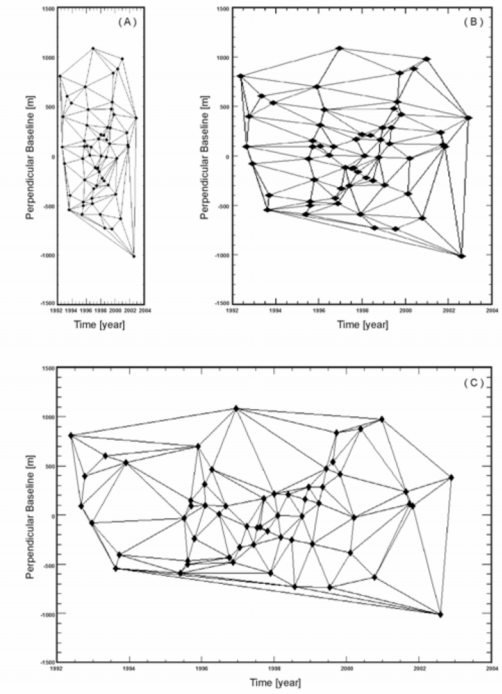

Figure 3. 14 Delaunay triangulations in the temporal/perpendicular baseline plane relevant to the ERS data analyzed in our experiments. The triangulations are obtained by assuming that the ratio between the perpendicular and temporal baseline axis units is equal to $\delta T/\delta b_{\perp}$, with (a) $\delta T = 1500$ days and $\delta b_{\perp} = 300$ m; (b) $\delta T = 900$ days and $\delta b_{\perp} = 300$ m; (c) $\delta T = 300$ days and $\delta b_{\perp} = 300$ m.

APPENDIX C

CONSIDERATIONS ABOUT THE TEMPORAL/PERPENDICULAR BASELINE DELAUNAY TRIANGULATION

Let us investigate in the following the impact of the different selection of the $\delta T/\delta b_{\perp}$ factor that represents the ratio between the temporal and perpendicular baseline axis units and is needed in order to generate the

triangulation in the $T \times B_{\perp}$ plane. To achieve this task we started from the triangulation relevant to our experiments presented in Section 3.3.2, where we have assumed δT =1500 days and $\delta b_{\perp}$ =300m; subsequently, we maintained constant the value of $\delta b_{\perp}$ and considered the two additional cases relevant to δT = 900 days and δT = 300 days, respectively.

The results of the corresponding triangulations, presented in Figures 3.11A, 3.11B and 3.11C, respectively, show a strong similarity. More specifically, we found that more than 60% of the arcs (thus of the corresponding interferograms) are common to the three triangulations. Accordingly, we may finally conclude that, within a realistic range of variation of the $\delta T / \delta b_{\perp}$ ratio, the corresponding triangulations in the $T \times B_{\perp}$ plane do not significantly change.

TABLE 3.1
ERS1/2 SAR DATA SET

Mission	Orbit	Day	Month	Year	$b_{\perp}$ [m]
ERS1	3960	18	4	1992	808
ERS1	5463	1	8	1992	90
ERS1	5964	5	9	1992	396
ERS1	6966	14	11	1992	-78
ERS1	8970	3	4	1993	603
ERS1	10473	17	7	1993	-544
ERS1	10974	21	8	1993	-400
ERS1	11976	30	10	1993	537
ERS1	19835	1	5	1995	-589
ERS1	20336	5	6	1995	-29
ERS1	20837	10	7	1995	-499
ERS2	1664	11	7	1995	-464
ERS1	21338	14	8	1995	151
ERS2	1665	15	8	1995	93
ERS2	2166	19	9	1995	-242
ERS1	22340	23	10	1995	698
ERS1	23342	1	1	1996	309
ERS2	3669	2	1	1996	101
ERS1	24344	11	3	1996	468
ERS2	5673	21	5	1996	6
ERS2	6675	30	7	1996	91
ERS2	7176	3	9	1996	-427
ERS2	7677	8	10	1996	-482
ERS2	8178	12	11	1996	1086
ERS2	8679	17	12	1996	-327
ERS2	9681	25	2	1997	-117
ERS2	10683	6	5	1997	-303
ERS2	11184	10	6	1997	-128
ERS2	11685	15	7	1997	-122
ERS2	12186	19	8	1997	170

TABLE 3.1
ERS1/2 SAR DATA SET

Mission	Orbit	Day	Month	Year	$b_\perp$ [m]
ERS2	12687	23	9	1997	-161
ERS2	13188	28	10	1997	-590
ERS2	13689	2	12	1997	215
ERS2	14190	6	1	1998	0
ERS2	14691	10	2	1998	-223
ERS2	15693	21	4	1998	209
ERS2	16194	26	5	1998	-250
ERS2	16695	30	6	1998	-727
ERS2	17697	8	9	1998	-12
ERS2	18198	13	10	1998	164
ERS2	18699	17	11	1998	286
ERS2	19200	22	12	1998	-292
ERS2	20202	2	3	1999	123
ERS2	20703	6	4	1999	282
ERS2	21204	11	5	1999	476
ERS2	21705	15	6	1999	-737
ERS2	22206	20	7	1999	544
ERS2	22707	24	8	1999	837
ERS2	23208	28	9	1999	420
ERS2	24711	11	1	2000	-383
ERS2	25212	15	2	2000	-25
ERS2	26214	25	4	2000	880
ERS2	28218	12	9	2000	-631
ERS2	29220	21	11	2000	979
ERS2	32727	24	7	2001	236
ERS2	33228	28	8	2001	111
ERS2	33729	2	10	2001	91
ERS2	37737	9	7	2002	-1013
ERS2	39240	22	10	2002	385

Chapter 4

Multi-Platform D-InSAR algorithm

This chapter will deal in the extension of the original, multiple interferogram D-InSAR algorithms, presented in the previous chapters, to the case where SAR data are collected by different sensors.

In particular, we will refer to the case-study characterized by the combination of the ERS1/2 SAR data with those acquired by the new European radar satellite ASAR (Advanced Synthetic Aperture Radar) mounted on board to the ENVISAT platform..

Moreover, as subsequently clarified, these approaches could be also effectively used to combine interferometric products, obtained by using multi-mode SAR data acquisitions.

4.1 Introduction

Differential SAR Interferometry (D-InSAR) is a microwave remote sensing technique that exploits the phase difference between SAR image pairs acquired at different times, in order to extract information on the radar line of sight (LOS) projection of the displacements, occurred between the relevant acquisitions [29]. The D-InSAR approach has been mostly applied, until now, to SAR data acquired by the same radar sensor, with a major role played by the ERS-1 and ERS-2 systems that have collected more than twelve years of data relevant to a large part of the Earth surface.

Since March 2002, also the ENVISAT satellite has been collecting SAR data by operating the ASAR sensor. The ASAR sensor has been designed to provide a large degree of operational flexibility. The main instrument parameters can be selected by ground command for each of the five operational modes:

- The Image mode generates high-spatial resolution data products selected from the total of seven available swaths, located over a range of incidence angles spanning 15 to 45 deg;
- The Wave mode generates vignettes of 5 Km by 5 Km, spaced 100 Km along track, whose positions can be selected to alternate between any two of the seven swaths;

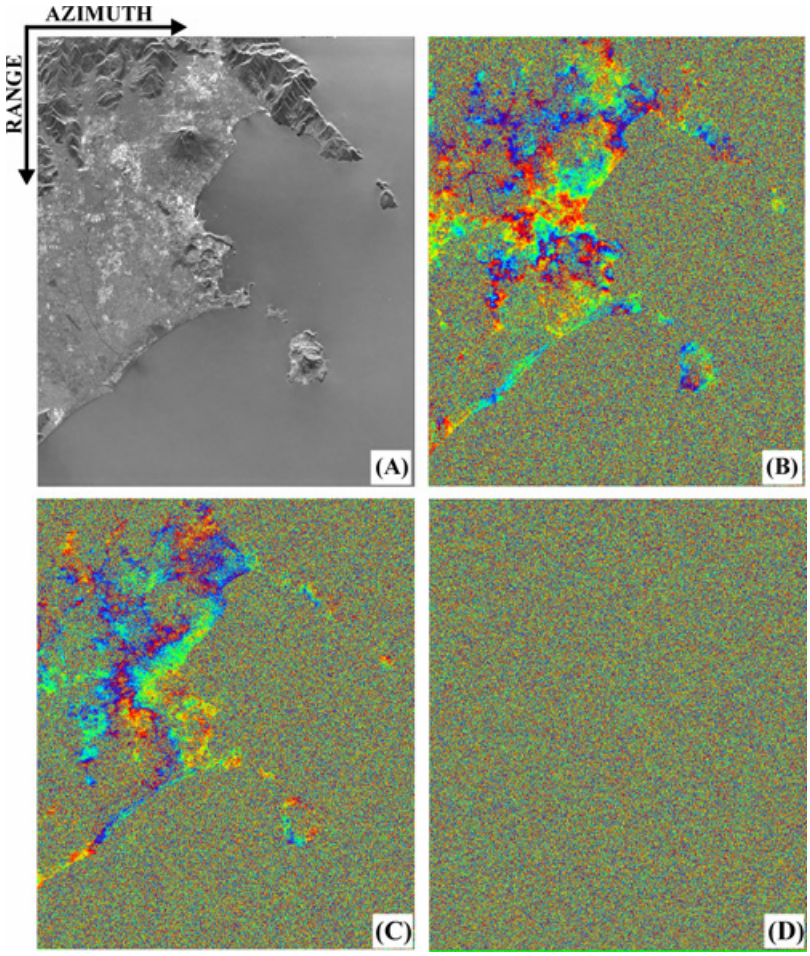

Figure 4. 1 SAR products relevant to the Napoli bay area. A) Multilook intensity image of the area. B) Single-platform multilook interferogram computed from the ERS data pair acquired on 02/03/2000 and 20/07/2000, respectively (=56 m). C) Single-platform multilook interferogram computed from the ENVISAT data pair acquired on 07/11/2002 and 05/06/2003, respectively (=246 m). D) Multilook cross-interferogram computed by using the ERS data acquired on 20/07/2000 and the ENVISAT one acquired on 07/11/2002 (=12 m).

- The Wide Swath and the Global Monitoring modes are based on the ScanSAR technique. By using five sub-swaths, they generate wide-swath products (400 Km) with spatial resolutions of 150 and 1000m, respectively;

- The Alternating Polarization mode provides two simultaneous images from the same area in HH and VV polarizations (the first letter indicates the polarization of the transmitted signal – H for horizontal, V for vertical – and the second the polarization of the received signal), HH and HV or VV and VH, with the same imaging geometry as the Image mode and, similarly, high spatial resolution.

One of the operational modes of the ASAR sensor, characterized by a side looking angle of about 23° (swath IS2), being geometrically compatible with the ERS-1/2 sensors illumination mode, can be therefore exploited within the interferometric SAR (InSAR) processing of multi-platform ERS/ENVISAT data. However, even if geometrically feasible, a combination of this kind of data is not easy because the two radar sensors operate both at C-band, but with slightly different carrier frequencies: 5.331 GHz for the ENVISAT sensor vs. 5.3 GHz for the ERS one. This circumstance limits the use of ERS/ENVISAT multilook cross-interferograms because they are corrupted by the decorrelation noise induced by the carrier frequency difference.

A first solution to circumvent this limitation would require the selection of a set of interferometric pairs, whose perpendicular baseline values are able to balance the range frequency shift due to the difference on the two carrier frequencies, as expected from the following relation (see equation 48, chapter one)

$$\Delta f_{ERS-ENVISAT} \approx -\frac{2b_{\perp e}}{\lambda r' \tan\left(\vartheta' - \bar{\Omega}\right)} \tag{1}$$

wherein $\Delta f_{ERS-ENVISAT}$ is the range frequency shift due to the difference in the two carrier frequency, λ is the ERS operational wavelength, ϑ' is the side-looking angle, $\bar{\Omega}$ is the local topographic slope, r' is the slant range difference and, finally, $b_{\perp e}$ is the equivalent perpendicular baseline separation corresponding to the same spectral shift. To better clarify these issues, some examples are presented in Figure 4.1 relevant respectively to ERS and ENVISAT conventional (Figure 4.1B and Figure. 4.1C) and cross (Figure. 4.1D) interferograms.

Another possible solution to circumvent the decorrelation phenomena, clearly visible in Figure 4.2D, is to exploit point-wise targets, as in the case of the Permanent Scatterers approach which is based on the analysis of full resolution (single look) interferograms [76].

Here, an alternative solution for the generation of deformation time-series from ERS and ENVISAT data, which exploits multi-looked

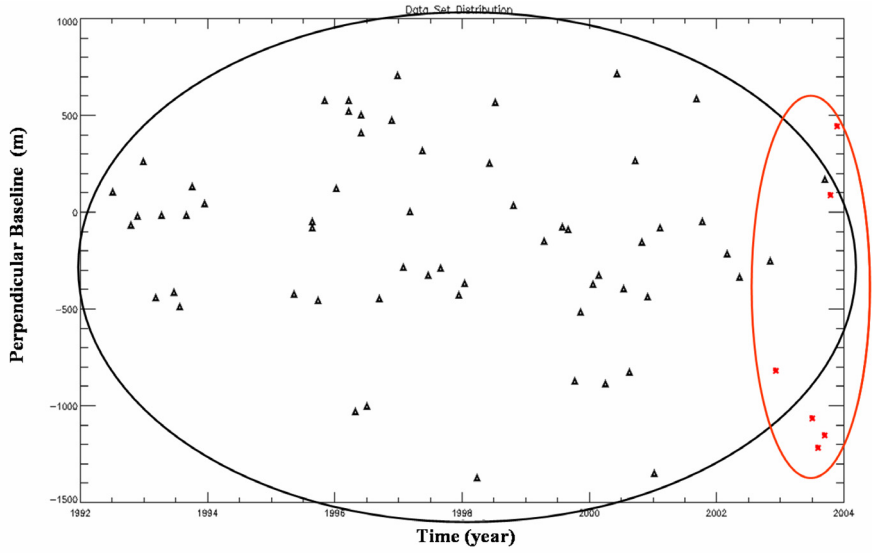

Figure 4. 2 ERS/ENVISAT data-set distribution relevant to the Napoli bay area test-site (acquired on descending orbits). The triangles are related to the ERS acquisitions while the red stars refer to the ENVISAT data. The difference in the two carrier frequency can be viewed responsible for the presence of another set of independent data (subset) to be properly connected.

interferograms, will be presented. Our approach exploits the Small Baseline Subset (SBAS) algorithm [39] in order to combine ERS and ENVISAT multi-looked interferograms; in particular, we avoid the use of ERS/ENVISAT cross-interferograms, benefiting, whenever possible, of the temporal overlap between the time-series acquisitions of the two sensors. Indeed, the images acquired by the ERS and ENVISAT radar systems are assumed to belong to independent subset (see Figure 4.2) and the time-series generation, involving single platform (i.e., ERS/ERS or ENVISAT/ENVISAT) interferograms only, is carried out by searching for a least squares solution with a minimum norm energy constraint; this result is easily achieved by applying the singular value decomposition (SVD) technique.

We note that the impact of the multi-sensor data processing on the original SBAS algorithm is minimal and, therefore, the procedure implementation is straightforward.

The presented results, obtained on a SAR data set relevant to the Napoli city area (Italy) and acquired on descending orbits confirm the effectiveness of the presented approach.

4.2 Multi-sensor SBAS algorithm

The SBAS technique is a relatively new D-InSAR approach for detecting earth surface deformations and, above all, for the analysis of their temporal evolution. For a detailed discussion on the original SBAS approach the reader is remained to the chapter two or, directly, to the literature concerning this task [65,77-78]. Accordingly, in the following, we will focus on the main issues relevant to the extension of this technique to multi-sensor data processing, with the key application represented by the ERS and ENVISAT/ASAR (swath IS2) case.

Let us start our analysis by considering the ERS and ENVISAT systems acquiring, at the ordered times $(t_0,...,t_N)$, a set of N+1 SAR images, relative to the same area. Accordingly, we specify for each focused SAR image the corresponding transmitted signal central wavelength $\lambda_i = (\lambda_{ERS} \quad or \quad \lambda_{ENV}) \quad i = 0,...,N$, being λ_{ERS} and λ_{ENV} the ERS and ENVISAT central wavelengths, respectively. We also assume, for sake of simplicity, that all the images are co-registered with respect to a master image in order to have a common reference grid; in particular this operation also takes into account for the different pulse repetition and range sampling frequencies of the ERS and ENVISAT sensors. Accordingly, a common pixel spacing dimension for all the images is assumed hereafter.

The starting point of the proposed combination technique is represented by the generation of a number, say M, of differential interferograms that have to be properly unwrapped; these interferograms involve the previously mentioned set of N+1 SAR acquisitions and, in particular, the selected D-InSAR pairs are characterized by a small perpendicular baseline constraint (significantly smaller than the critical baseline [21]) and no ERS/ENVISAT cross-interferograms are considered. Let us also assume that $\left[IE_1,...,IE_j,...,IE_M\right] \quad \forall j = 1,...,M$ and $\left[IS_1,...,IS_j,...,IS_M\right] \quad \forall j = 1,...,M$ are the vectors corresponding to the acquisition time-indexes associated with the chronologically ordered image pairs used for the interferograms generation (i.e., $IE_j > IS_j \quad \forall j = 1,...,M$); moreover, let $\left[\lambda_1,...,\lambda_j,...,\lambda_M\right] \quad \forall j = 1,...,M$ be the vector of the transmitted signal central wavelengths associated with each single interferogram, without any ambiguity in the identification of the factor λ_j for each interferogram, since the use of cross-interferograms is avoided.

Let us now to refer to a generic pixel of azimuth and range coordinates (x,r) and to assume that the phase signal of each interferogram is calibrated with respect to a pixel whose deformation behavior is a priori known (typically a highly coherent pixel located in a non-deforming zone); the

expression of the generic j-th interferogram, computed from the SAR acquisitions at times t_B and t_A has the following expression [39]:

$$\begin{aligned}\delta\phi_j(x,r) &= \phi(t_B,x,r)-\phi(t_A,x,r)\cong \\ &\cong \frac{4\pi}{\lambda_j}\left[d(t_B,x,r)-d(t_A,x,r)\right]+\frac{4\pi}{\lambda_j}\frac{b_{\perp j}}{r'\sin\vartheta'}\Delta z+ \\ &+\frac{4\pi}{\lambda_j}\left[d_{atm}(t_B,x,r)-d_{atm}(t_A,x,r)\right]+\Delta n_j \\ &\forall j=1,...,M\end{aligned} \tag{2}$$

wherein $\phi(t_B,x,r)$ and $\phi(t_A,x,r)$ represent the phases of the two images involved in the interferogram generation while $d(t_B,x,r)$ and $d(t_A,x,r)$ are the line of sight cumulative deformations at times t_B and t_A with respect to the instant t_0, assumed as a reference. Moreover, for what concerns the right hand side part of the last identity in equation (2), the second term accounts for possible topographic artifacts Δz that can be present in the used DEM and depends on the perpendicular baseline component $b_{\perp j}$ as well as on the sensor-target distance r' and on the look angle ϑ'. Finally, the terms $d_{atm}(t_B,x,r)$ and $d_{atm}(t_A,x,r)$ in (2) accomplish for possible inhomogeneities between the two acquisitions (usually referred to as atmospheric phase signal), while the last term Δn_j accounts for decorrelation phenomena and thermal noise effects.

By considering (2) and neglecting the Δn_j term, it is evident that the ERS and ENVISAT (single-platform) interferograms expression only differs for the sensor wavelength values. Accordingly, in order to homogenize the data set and to end up with a stack of unwrapped interferograms depending on a single wavelength (the ERS one, for example), we may easily rescale the overall data set as follows

$$\delta\tilde{\phi}_j(x,r)=\delta\phi_j(x,r)\frac{\lambda_j}{\lambda_{ERS}} \quad \forall j=1,...,M \tag{3}$$

The expressions (2) and (3) define a system of M equations in the N unknowns

$$\tilde{\phi}(t_i,x,r)=\phi(t_i,x,r)\frac{\lambda_i}{\lambda_{ERS}} \quad \forall i=0,...,N-1 \tag{4}$$

this system can be re-organized by using the following matrix formalism

$$A\tilde{\phi} = \delta\tilde{\phi} \tag{5}$$

wherein A is an incidence-like matrix, directly related to the set of interferograms generated from the available data [39]. Note also that the presented technique implies a pixel-by-pixel temporal analysis; accordingly, the dependence on the variables (x,r) has been neglected in (5) and the simplification is maintained in the matrix representation hereafter.

We may now manipulate the equation system in (5) in such a way to replace the present unknowns with the mean phase velocity between time adjacent acquisitions. Accordingly, the new unknowns become

$$v = \left[v_1 = \frac{\tilde{\phi}(t_1, x, r)}{t_1}, ..., v_N = \frac{\tilde{\phi}(t_N, x, r) - \tilde{\phi}(t_{N-1}, x, r)}{t_N - t_{N-1}} \right] \tag{6}$$

and, by substituting (6) in (5), we finally get the new system equation expression

$$Bv = \delta\tilde{\phi} \tag{7}$$

wherein B represents an $M \times N$ matrix, whose generic (j,k) element is now $B(j,k) = t_{k+1} - t_k$ for $IS_j \le k \le IE_j \quad \forall j = 1, ..., M$, and $B(j,k) = 0$ elsewhere.

Few considerations on the expression (7) are now in order. First of all, we remark that it is formally identical, except for the wavelength scaling step in (3), to the one computed in [39]. Moreover, we stress that, in addition to the perpendicular baseline constraint, which is common to the original SBAS technique, the assumed separation of the ERS and ENVISAT data in independent subset causes an additional rank deficiency of the matrix B, leading the system (7) to have infinite solutions. However, as in [39], the application of the SVD method allows us to evaluate the pseudo-inverse of the matrix B, which gives the minimum norm LS solution of the system (7). In this context, the above mentioned minimum norm constraint for the velocity vector v avoids the presence of discontinuities in the final result, guaranteeing a physically sound solution [79]; this consideration is at the base of the data manipulation leading to (7). Obviously, an additional

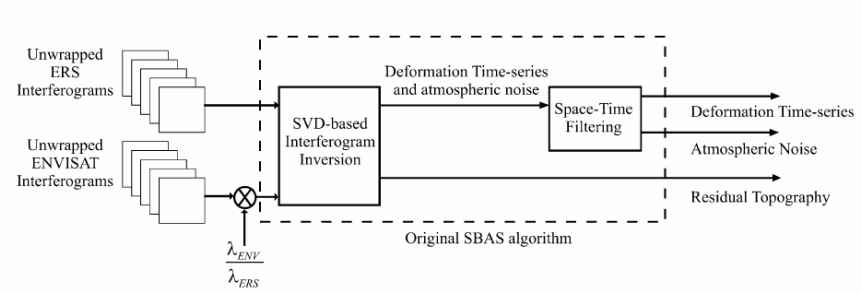

Figure 4. 3 Block diagram of the ERS/ENVISAT SBAS procedure.

integration step is necessary to compute the solution $\tilde{\phi}$ from the estimated v vector, but this represents a trivial operation.

As a final remark, we observe that following the solution of the system of equations (7), the processing steps applied to separate the deformation signal component $d(\cdot)$ from the atmospheric and topographic components $d_{atm}(\cdot)$ and Δz, respectively, remains the same of the original SBAS procedure with no need for any further modification.

In summary, following a trivial rescaling step, the application of the SBAS technique to produce ERS/ENVISAT deformation time-series is straightforward. Consistently with the original SBAS algorithm, an important constraint is represented by the availability of a temporal overlap between the different platform acquisitions; on the other hand, the decorrelation noise induced by the use of ERS/ENVISAT cross-interferograms is completely avoided and the use of multi-looked interferograms is ensured.

The presented extension of the SBAS algorithm may be effectively used also in the case where the combination of SAR data acquired by the same sensor but by using different operational modes (as for example, if we would be interested to combine STRIPMAP and SCANSAR data). This can be done by easily observing that multi-mode SAR data can be also viewed as belonging to independent subset and consequently can be integrated each other via the application of the SVD method. This approach is expected to be more and more significant in the future when SAR data collected by novel multi-operational radar sensor will be available.

4.3 Experimental Results

The validation of the proposed algorithm has been carried out by processing a set of SAR images relevant to the Napoli city area (Italy), and acquired by the ERS-1/ERS-2 and ENVISAT systems on descending orbits (track 36 and frame 2781).

In particular, the ERS dataset is composed by 63 images spanning the time interval from June 1992 to February 2004 while the ENVISAT one includes 12 images, acquired during the last two years (see Table 4.1). From these data, 181 D-InSAR interferograms have been produced: 157 involving ERS images, the remaining 24 computed from ENVISAT acquisitions. For the D-InSAR interferogram generation, we have imposed for both the ERS and the ENVISAT data a perpendicular baseline constraint of 300m and a maximum temporal separation of about 4 years. The D-InSAR products have been obtained following a complex multi-looked operation with 4 looks in the range direction and 20 looks in the azimuth one (the resulting pixel dimensions are of about 100m x 100m) and precise satellite ERS and ENVISAT orbital information, in conjunction with an SRTM DEM of the overall area, have been used.

In order to provide an overall picture of the achieved results, we present in Figure 4.4 the estimated mean deformation velocity, superimposed on the multilook SAR image of the Napoli city area. This kind of representation is visually effective and allows us to easily get an information about the detected mean deformations; note also that noisy areas with a low accuracy measurement have been excluded from the presented map.

In order to demonstrate the capability of the proposed approach to provide information not only on the mean displacements, but also on the temporal evolution of the detected deformations, some experiments are presented. These examples involve a comparison between the deformation time-series computed from the ERS/ENVISAT data set and those measured via on site precise leveling techniques.

The first experiment is relevant to two pixels labeled b and c in Figure 4.4a, which are located in the maximum displacement zone of the Campi Flegrei Caldera area where both D-InSAR and leveling measurements are available; we remark that in this zone the deformations have a nearly vertical component only [77], thus allowing a direct comparison between SAR and geodetic measurements. By observing the D-InSAR time-series relevant to the pixels b and c of Figure 4.4a, which are plotted in Figures 4.4b and 4.4c, respectively, it is evident a deformation behavior characterized by a rather continuous subsidence, except at the beginning of 2000, when a change of the displacement trend (resulting in an uplift phase) occurred; following the beginning of 2002, a stable situation is recovered. This deformation trend is

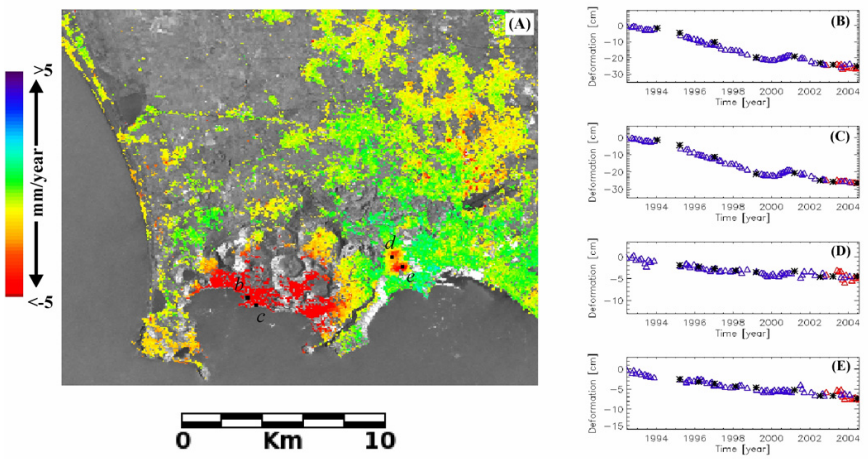

Figure 4. 4 ERS/ENVISAT DInSAR results. (A) Geocoded map of the mean deformation velocity of the area of Napoli city (Italy) computed in coherent areas only and superimposed on the multilook SAR image (grayscale representation) of the zone. (B), (C), (D), (E) Deformation time-series relevant to the pixels in (A) labeled b, c, d, e, respectively, computed from the DInSAR (ERS data are identified in the plot by red triangles, while the ENVISAT ones are in blue) and leveling (black stars connected by a continuous line) measurements.

confirmed by the leveling measurements, which have been projected into the radar LOS and superimposed to the D-InSAR measurements; the good agreement between leveling and D-InSAR data is evident.

The second experiment concerns two pixels located in the highly urbanized area of the Vomero quarter where leveling measurements are available for the two pixels labeled d and e in Figure 4.4a; a direct comparison between these geodetic data and the D-InSAR results is again possible because the deformations have a dominantly vertical characteristic also in this area [78]. The time-series relevant to these two pixels are plotted in Figures 4.4d and 4.4e, respectively, wherein D-InSAR and leveling results have been superimposed. Also in this case a very good agreement between the different measurements is found, confirming the effectiveness of the proposed multi-sensor D-InSAR processing procedure.

4.4 Conclusion

Within this chapter, we have exploited the SBAS approach to produce multi-sensor deformation time-series by combining SAR data acquired by the ERS and ENVISAT/ASAR sensors. The algorithm is focused on

investigating deformations of large areas with a spatial resolution of about 100m x 100m and is based on a simple but effective combination of ERS/ERS and ENVISAT/ENVISAT multi-looked interferograms, with no need for ERS/ENVISAT cross-interferograms.

Moreover, the procedure is easy to implement because no significant modifications are required within the original SBAS processing technique. The presented results, relevant to the Napoli city area, confirm the effectiveness of the approach.

Mission	Orbit	Day	Month	Year	$B_\perp$	Subset
ERS1	4690	8	6	1992	93	1
ERS1	6193	21	9	1992	-74	1
ERS1	6694	26	10	1992	-24	1
ERS1	7195	30	11	1992	258	1
ERS1	8197	8	2	1993	-440	1
ERS1	8698	15	3	1993	-19	1
ERS1	9700	24	5	1993	-418	1
ERS1	10201	28	6	1993	-492	1
ERS1	10702	2	8	1993	-22	1
ERS1	11203	6	9	1993	127	1
ERS1	12205	15	11	1993	42	1
ERS1	19563	12	4	1995	-425	1
ERS1	21066	26	7	1995	-52	1
ERS2	1393	27	7	1995	-87	1
ERS2	1894	31	8	1995	-452	1
ERS2	2395	5	10	1995	564	1
ERS2	3397	14	12	1995	117	1
ERS1	24072	21	2	1996	513	1
ERS2	4399	22	2	1996	568	1
ERS2	4900	28	3	1996	-1021	2
ERS1	25074	1	5	1996	491	1
ERS2	5401	2	5	1996	402	1
ERS2	5902	6	6	1996	-997	2
ERS2	6904	15	8	1996	-443	1
ERS2	7906	24	10	1996	464	1
ERS2	8407	28	11	1996	696	1
ERS2	8908	2	1	1997	-285	1
ERS2	9409	6	2	1997	0	1
ERS2	10411	17	4	1997	310	1
ERS2	10912	22	5	1997	-329	1
ERS2	11914	31	7	1997	-292	1
ERS2	13417	13	11	1997	-425	1
ERS2	13918	18	12	1997	-368	1
ERS2	14920	26	2	1998	-1362	3
ERS2	15922	7	5	1998	248	1
ERS2	16423	11	6	1998	556	1
ERS2	17926	24	9	1998	30	1
ERS2	20431	18	3	1999	-152	1
ERS2	21934	1	7	1999	-79	1
ERS2	22435	5	8	1999	-91	1
ERS2	22936	9	9	1999	-867	2
ERS2	23437	14	10	1999	-513	1
ERS2	24439	23	12	1999	-370	1
ERS2	24940	27	1	2000	-327	1
ERS2	25441	2	3	2000	-880	2
ERS2	26443	11	5	2000	705	1
ERS2	26944	15	6	2000	-399	1
ERS2	27445	20	7	2000	-824	2
ERS2	27946	24	8	2000	258	1
ERS2	28447	28	9	2000	-158	1
ERS2	28948	2	11	2000	-435	1
ERS2	29449	7	12	2000	-1337	3
ERS2	29950	11	1	2001	-83	1
ERS2	32455	5	7	2001	-209	1
ERS2	32956	9	8	2001	576	1
ERS2	33457	13	9	2001	-45	1
ERS2	35461	31	1	2002	-213	1
ERS2	36463	11	4	2002	-357	1
ERS2	38467	29	8	2002	-346	1
ERS2	38968	3	10	2002	-249	1
ENVISAT	3597	7	11	2002	-812	4
ENVISAT	6603	5	6	2003	-1058	4
ENVISAT	7104	10	7	2003	-1206	4
ENVISAT	7605	14	8	2003	-1141	4
ERS2	43477	14	8	2003	165	1
ENVISAT	8106	18	9	2003	87	4
ENVISAT	8607	23	10	2003	439	4
ERS2	44479	23	10	2003	-44	1
ENVISAT	9108	27	11	2003	-345	4
ERS2	45982	5	2	2004	-940	2
ENVISAT	10611	11	3	2004	264	4
ENVISAT	11112	15	4	2004	-128	4
ENVISAT	11613	20	5	2004	-133	4
ENVISAT	12114	24	6	2004	-516	4
ENVISAT	12615	29	7	2004	-27	4

Table 4. 1 ERS/ENVISAT SAR data-set.

Chapter 5

Experimental results

This chapter will be focused on the application of the D-InSAR approaches, up to now discussed, to real case-studies, with a particular emphasis on the role played by the different interferometric distributions one can consider.

Firstly, we will concentrate on the application of the Extended Minimum Cost Flow (E-MCF) [74,80] phase unwrapping algorithm (see also chapter three) to a properly chosen, interferometric data distribution. To this end, the SAR data-set of the Umbria test-site area has been chosen and the achieved results have been properly analyzed. Moreover, in the D-InSAR scenario, the joint availability of SAR data acquired both on ascending and descending orbits allowed us to combine the obtained results, in order to discriminate the deformation velocity components along the east-west and the vertical direction, respectively (by exploiting the strategy explained within the chapter two).

Finally, it has been investigated the possibility to apply the E-MCF algorithm to a multi-platform/multi-mode case, thus extending the proposed algorithm to the cases explored in the previous chapter. With regards to this task, the SAR data-set of the Napoli Bay area, acquired from both the ERS sensors and the ENVISAT one, has been selected.

A discussion concerning the achieved products and the future improvement of the presented D-InSAR techniques (with emphasis on the phase unwrapping problems) will be finally addressed.

5.1 Interferogram selection strategy

To introduce the experimental results hereafter presented, it can be convenient, first of all, to clarify how the list of differential interferograms to use within the processing procedure could be chosen. We also remark that, as explained within the chapter three, the application of the Extended Minimum Cost Flow phase unwrapping algorithm would explicitly require a peculiar interferometric distribution, obtained via a Delaunay triangulation on the Temporal/Perpendicular Baseline plane. In any case, in order to increase the robustness of the deformation time-series extraction procedure, it is ever possible to expand the original interferometric data-set (triangulation-driven) by introducing a set of additional interferometric pairs,

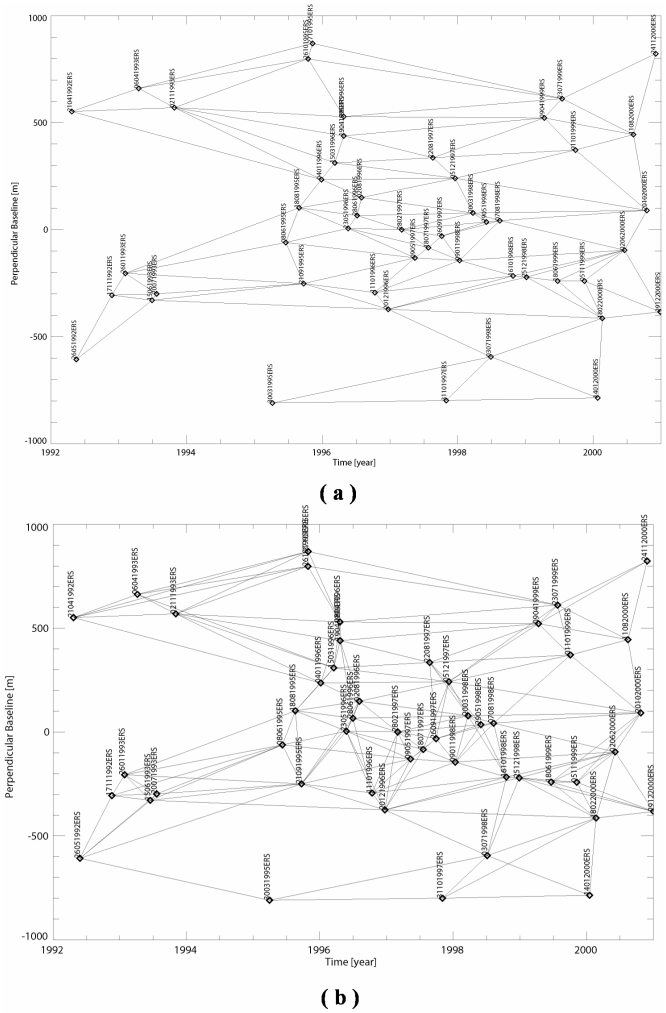

Figure 5. 1 Umbria area case-study interferometric distribution (a) relevant to the Delaunay triangulation and (b) those obtained after the introduction of additional data-pairs. The descending SAR data have been here considered.

and eventually re-use the SAR acquisitions which were formerly discarded, because not belonging to the Delaunay sub-triangulation (obtained, as explained in chapter three, after the triangles removal step needed if we want to manage low-decorrelated differential interferograms, only).

To give an example, we can refer to the SAR data acquisition of the Umbria area test-site and to the corresponding Delaunay triangulation used within the E-MCF algorithm (Figure 5.1a). The key idea is to consider, with

respect to the original interferometric distribution, a set of additional interferograms which also respect the constraints about the maximum baseline separations (also eventually including the limitations on the common azimuth bandwidth depending on the doppler centroid differences). The whole interferometric distribution, shown in Figure 5.1b will be subsequently used for the extraction of the corresponding deformation time-series. The differential phase interferograms associated to the interferometric distribution we chose, could be effectively unwrapped by applying a specific phase unwrapping algorithm but, being interested to investigate on the potentiality of the E-MCF algorithm, we will concentrate hereafter (at least with regards to the part of them relevant to the Delaunay triangulation in the $T \times B_{\perp}$ plane) on the application of the proposed algorithm, by using other approaches (and, in particular, the original MCF algorithm) to compare the corresponding results, only.

At this stage, the problem to be solved will concern the way to proceed to unwrap the additional D-InSAR interferograms.

Basically, there are essentially two possibilities:

1. To independently unwrap each single additional phase, in application of other phase unwrapping approaches (the original MCF algorithm, for example);
2. To exploit the information achievable by the set of the D-InSAR interferograms relevant to the Delaunay triangulation in the $T \times B_{\perp}$ plane (used for the E-MCF algorithm) to unwrap them.

Clearly, the second strategy is based on the assumption that the triangulation-driven unwrapped phases could be representative of the true phases without any other additional information, which can be eventually obtainable through the additional unwrapped phases. For this reason, by following this strategy, the result we can obtain will be similar to those previously achieved by using the triangulation one.

On the other hand, especially if the additional interferometric data-set is composed by a significantly high number of interferogram, the phase unwrapping incongruence (or errors), introduced by the two different phase unwrapping approaches we used, can decrease the quality of our reconstruction. These observations suggest us that, in any case, if we want to preserve the robustness of the algorithm, the number of additional interferograms should be relatively small. Basically, the choice of the best strategy to follow has to be done in dependence of the peculiar distribution which we have. Hereafter, the overall procedure to unwrap these additional interferograms will be investigated.

Let us now clarify how to unwrap these interferograms and, to do this, consider a set of $N+1$ independent SAR images of the same area, acquired

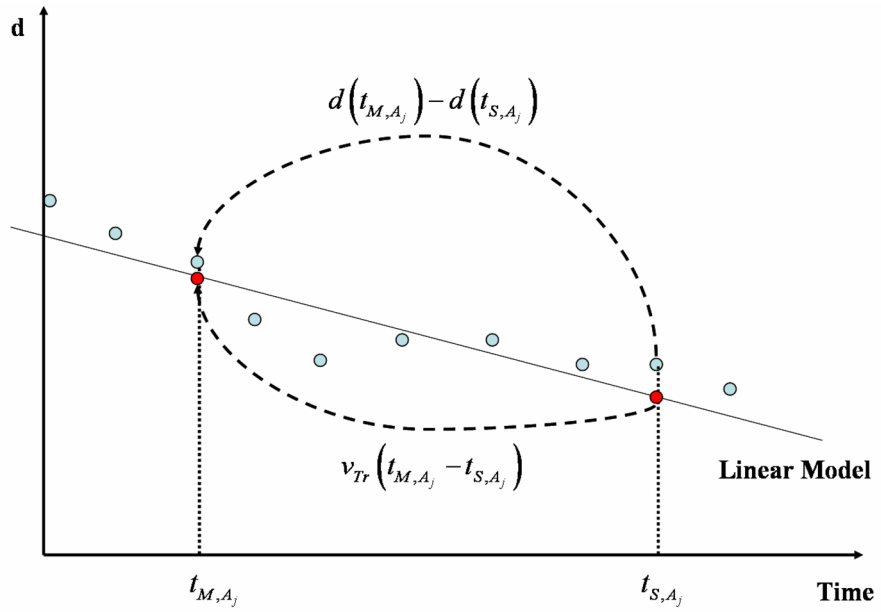

Figure 5. 2 A pictorial representation of the strategy can be applied to unwrap the additional interferograms, characterized by the introduction of a linear (red circles) and/or non-linear (blue circles) deformation model, respectively.

at the ordered $(t_0,t_1,...,t_N)$ times and define a Delaunay triangulation in the $T\times B_\perp$ plane, whose arcs will be unambiguously associated to the set of differential interferogram $\varphi_{Tr}=\left(\varphi_{Tr_1},...,\varphi_{Tr_M}\right)$. The set of additional interferograms (composed by L pairs) can be hence introduced with respect to the original data set, and the overall wrapped phase sequence will be finally the following one $\varphi=[\varphi_{Tr},\varphi_{Added}]=\left(\varphi_{Tr_1},...,\varphi_{Tr_M},\varphi_{A_1},...,\varphi_{A_L}\right)$.

First of all, we discuss how to proceed following the first strategy, in this case the additional phases can be independently unwrapped via the application of the original Minimum Cost Flow phase unwrapping algorithm [56] while the interferograms involved in the Delaunay triangulation will be unwrapped with the Extended-Minimum Cost Flow approach.

For what concerns the second strategy, we start from the observation that, if we introduce the E-MCF unwrapped interferograms $\psi_{Tr}=\left(\psi_{Tr_1},...,\psi_{Tr_M}\right)$, first of all, we will be able to retrieve the deformation trend of the analyzed area. In particular, starting from them and following the steps discussed in chapter two, for each pixel of the area, it will be

possible to evaluate the residual topography Δz and the relevant deformation time-series $d_{Tr}(t_0,t_1,...,t_N)$. In such a way, if the added interferograms are related to the same set of SAR acquisitions, the additional phases can be unwrapped by exploiting of an expectable model of the deformation, which can be retrieved from the achieved deformation time-series and the residual topography.

To better explain this concept, let us refer to Figure 5.2 and suppose that the generic, added j-th differential interferogram $\varphi_{A_j}\ j=1,...,L$ involves the master time acquisition t_{M,A_j} and the slave master acquisition t_{S,A_j}, respectively, with $t_{M,A_j}\in(t_0,t_1,...,t_N)$, $t_{S,A_j}\in(t_0,t_1,...,t_N)$. Consequently, the model for the unwrapped phase that we can introduce could be expressed as follows

$$m_{A_j}=\frac{4\pi}{\lambda}\left(\frac{\Delta b_{\perp A_j}}{r'\sin\vartheta'}\Delta z+d\left(t_{M,A_j}\right)-d\left(t_{S,A_j}\right)\right) \tag{1}$$

wherein $\Delta b_{\perp A_j}$ is the perpendicular baseline of the j-th interferogram, λ is the operational wavelength, r' is the slant range distance between the radar sensor and the center of the image and ϑ' is the sensor side-looking angle.

However, even if the condition $t_{M,A_j}\in(t_0,t_1,...,t_N)$, $t_{S,A_j}\in(t_0,t_1,...,t_N)$ was not verified, a model could be also introduced through the interpolation of the achieved deformation time-series relevant to a given point in space, or by taking account of the relevant, mean deformation velocity v_{Tr} (which can be estimated starting from the basic set of interferograms).

In the former case, the model we can introduce may be expressed as follows

$$m_{A_j}=\frac{4\pi}{\lambda}\left(\frac{\Delta b_{\perp A_j}}{r'\sin\vartheta'}\Delta z+d\left(t_{M,A_j}\right)-d\left(t_{S,A_j}\right)\right) \tag{2}$$

while, in the latter case, it could be equivalently expressed as

$$m_{A_j}=\frac{4\pi}{\lambda}\left(\frac{\Delta b_{\perp A_j}}{r'\sin\vartheta'}\Delta z+v_{Tr}\left(t_{M,A_j}-t_{S,A_j}\right)\right) \tag{3}$$

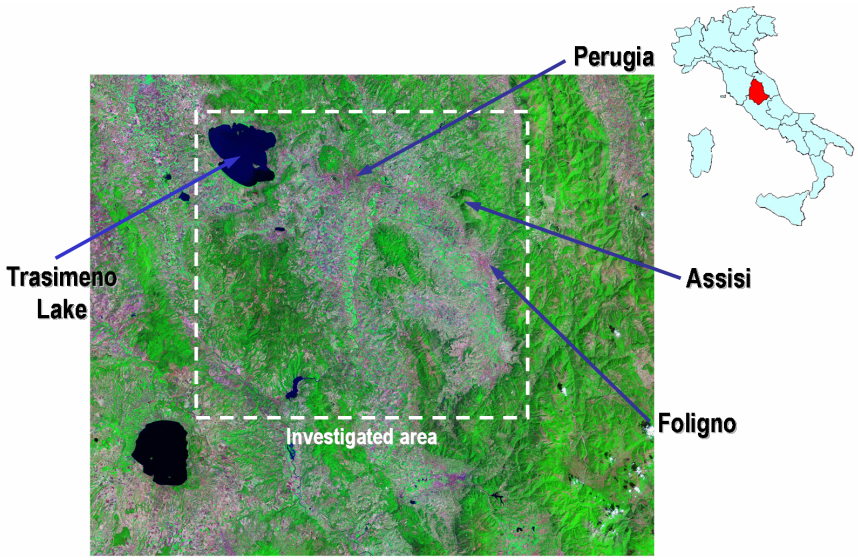

Figure 5. 3 The illuminated area of the Umbria region involved within the D-InSAR experiments.

In absence of noise effects, phase unwrapping and reconstruction errors, the wrapped version of the introduced model (i.e. $\langle m_{A_j} \rangle_{-\pi,\pi}$) should automatically fit (by neglecting the effect of the model inaccuracies) the phase φ_{A_j} we would like to unwrap. Obviously, this is not true in general, so that the residual phase pattern, so-defined

$$r_j = \langle \varphi_{A_j} - m_{A_j} \rangle_{-\pi,\pi} \tag{4}$$

will account for the overall incongruence of the achieved results. It may also contain ambiguous phase jumps, so that it must be unwrapped by using, for sake of simplicity, the original MCF approach.

Consequently, the unwrapped phase solutions will be finally expressed as follows

$$\psi_{A_j} = m_{A_j} + Unw(r_j) \quad j = 1,...,L \tag{5}$$

where the $Unw(\cdot)$ symbol accounts for the unwrapping operation.

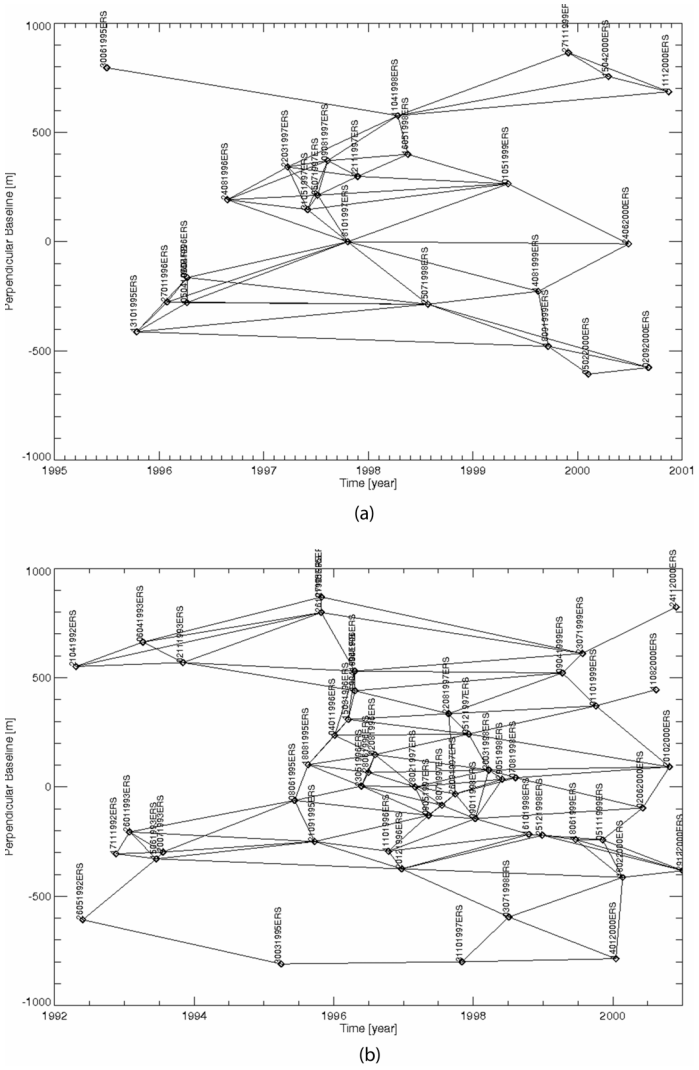

Figure 5. 4 Umbria area test site interferometric pairs distribution onto the Temporal/Perpendicular baseline plane both for the ascending (a) and the descending (b) oribits.

The presented procedure allows increasing the number of differential interferograms and, at the same time, verifying the correctness of the computed deformation time-series via the inspection of the residual phase terms but, as already explained, the best strategy to follow depends on the particular cases we encounter. For example, we would like to note that the

original Delaunay triangulation could be generally decomposed in more than one independent sub-triangulations (as shown in chapter three, section 5.3) even less overlapped and, when it occurs, a model for the additional phase unwrapping interferograms could be difficult to be effectively introduced. In these cases, even if the achievable temporal coherence factor could be significantly decrease (especially for high values of L), it is convenient to unwrap each interferogram without any additional information.

5.2 Umbria area experiments

In order to investigate the performances of the proposed algorithm, several experiments involving different SAR data-configuration typologies, have been performed. In this section, we firstly addressed the possibility to apply the E-MCF algorithm to an interferometric data-set composed by one subset, which has been selected by applying the strategy discussed in the previous section. The two SAR data-set relevant to the Umbria region (acquired on ascending and descending orbits, respectively) both satisfy this requirement. The investigated area, shown in Figure 5.3, is characterized by the presence of isolated plots of urbanized zones while the most part of it is quite vegetated and/or mountainous, thus rendering the achievable D-InSAR phases difficult to be effectively unwrapped.

Regardless to the expectable deformation patterns, we can observe that the selected area is essentially affected by subsidence phenomenon due to the water extraction activities. Note also that the deformation pattern in the neighborhood of the Foligno town takes necessarily account of the effect of the September 26, 1997 Colfiorito-Earthquake [81].

5.2.1 Deformation Time-Series Generation

We firstly applied the E-MCF algorithm both to the ascending and descending data-set. In particular, the ascending SAR data-set was composed by 24 acquisitions (see Table 5.1A), spanning the time interval between 1995 to 2000 and the descending one was composed by 48 SAR acquisitions from 1992 to 2000 (see Table 5.1B). Starting from them, the two corresponding sequences of differential interferograms have been formerly selected and, subsequently, generated. The two interferometric distribution are shown in Figure 5.4(a) and (b), respectively. In application to the Extend Minimum Cost Flow phase unwrapping algorithm and to the SBAS approach, the deformation time-series relevant to the two orbits have been evaluated. Figure 5.5 shows the achieved mean deformation velocity pattern of the observed area, superimposed to a relevant multi-looked SAR image and projected onto the descending line of sight (with a resolution of about

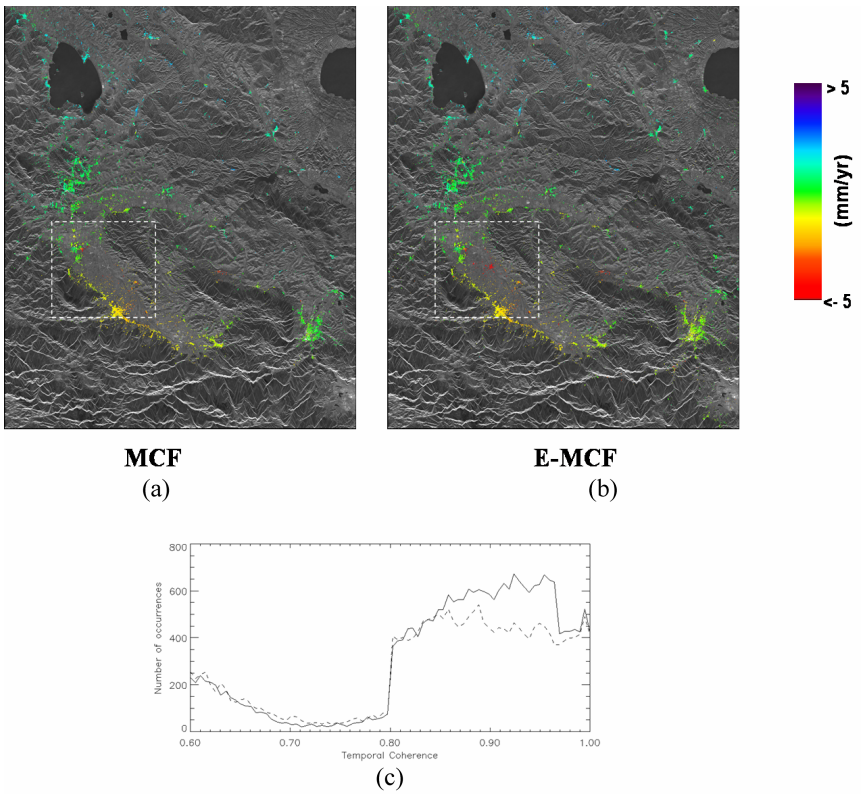

Figure 5. 5 False color maps representing the mean deformation velocity of the Umbria zone test-site, superimposed to a SAR amplitude image of the area, obtained via the application of the original (a) and the extended (b) minimum cost flow phase unwrapping algorithm, respectively. A direct comparison between the histograms of the temporal coherence factor is also shown in (c) wherein the dashed line refers to the results obtained by applying the original MCF approach and the continuous line to those achieved in application of the E-MCF algorithm.

100 x 100m). The whole processing procedure, aimed to the extraction of the deformation time-series, has been applied, and both the original and the extended phase unwrapping algorithm has been considered.

The same procedure has been applied to generate the corresponding time-series from the ascending SAR data. The joint analysis between our results and those obtained in application of the original MCF approach demonstrated, first of all, that the E-MCF algorithm guarantees higher temporal coherence maps. A direct comparison between the two temporal coherence maps has been considered and the corresponding results are

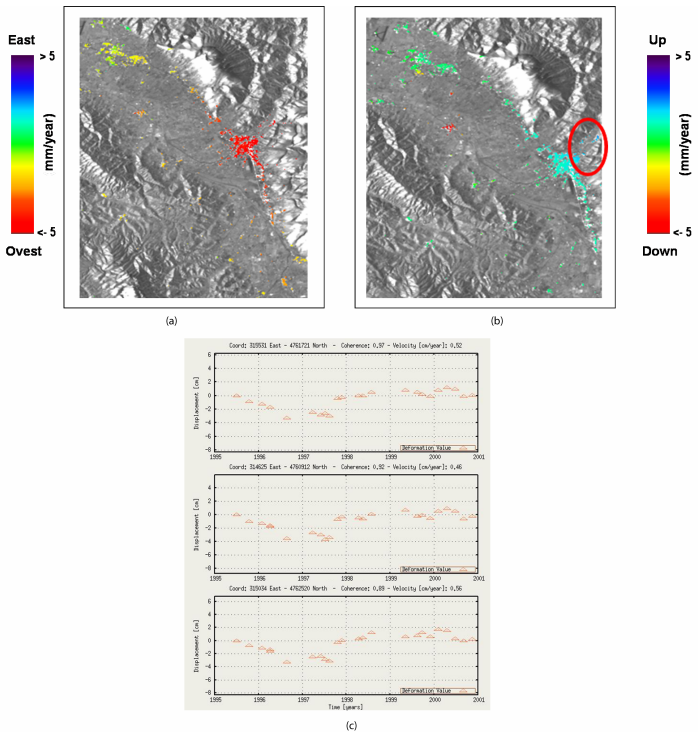

Figure 5. 6 Combination of ascending and descending interferometric products. The presented false color maps represents (a) the East-West component of the mean deformation velocity and (b) the vertical component of the mean deformation velocity, respectively and are relevant to the Assisi/Colfiorito area. The Colfiorito area (highlighted by a red oval in (b)) deformation time-series, shown in (c), allow us to clearly identify the effect of the earthquake phenomenon on September 26, 1997.

shown in Figure 5.5c. Moreover, it has allowed us to verify that, if areas affecting with fast-varying deformation trends are present, the relevant interferograms will be well-unwrapped through the application of the E-MCF algorithm while, the application of the original approach does not permit us to reproduce these trends (see the following sub-section).

5.2.2 Multi-orbital combination

As explained within the chapter three, the processing of both the ascending and the descending SAR data-set of the same test site area, allows discriminating the East-west and vertical displacements components, respectively. Following this procedure, the two unknown deformation components has been obtained and subsequently geocoded (see Figure 5.6).

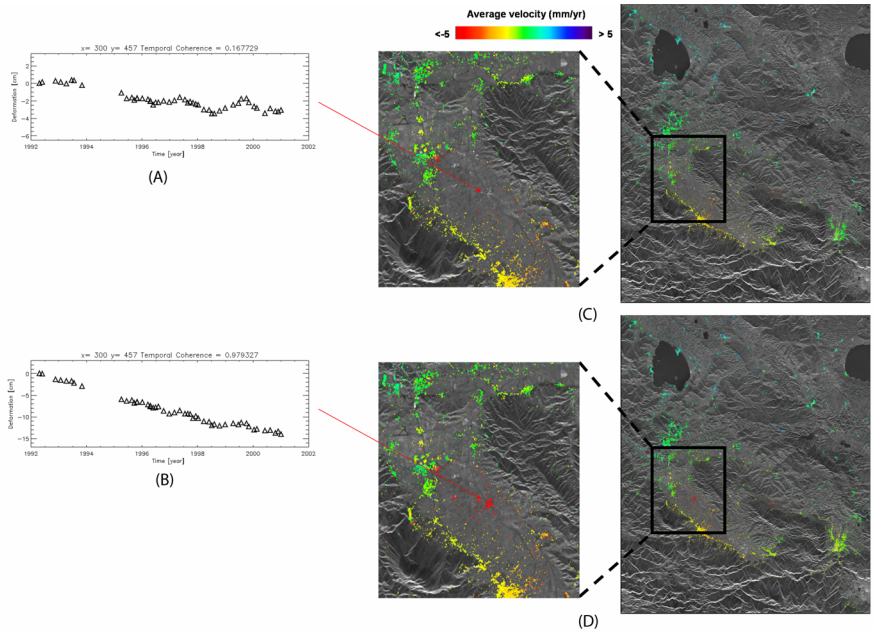

Figure 5. 7 Descending Umbria area results. (A) and (B) are the deformation time-series relevant to the center of the highlighted box achieved by applying the original and the extended MCF approach, respectively while, the mean deformation velocity maps are shown in (C) and (D), respectively.

We can observe that the highlighted area is essentially stable, except for the Foligno Town neighborhoods where the effect of the Colfiorito-Earthquake is clearly evident, especially if one refers to the vertical map. In particular, if we consider a single pixel here located, we can observe that a jump is present in the relevant time-series in correspondence to the earthquake phenomenon. Nevertheless, the other features on the vertical displacement map are essentially due to gravitational effects and/or to the water extraction activities [82].

Moreover, as introduced in the previous sub-section, the application of the extended MCF approach allowed us to monitor the deformation affecting areas which originally, through the application of the basic MCF phase unwrapping algorithm, were incoherent. In our maps, a significant portion of the novel coherent areas are affected by deformation mechanisms with a very rapidly temporal evolution, thus justifying the difficulty on the phase unwrapping steps. This affirmation can be, for example, supported by the observation of the two maps shown in Figure 5.7, and considering the achieved deformation time-series relevant to a pixel located at the center of the highlighted area. We can observe that, while the boundary of the

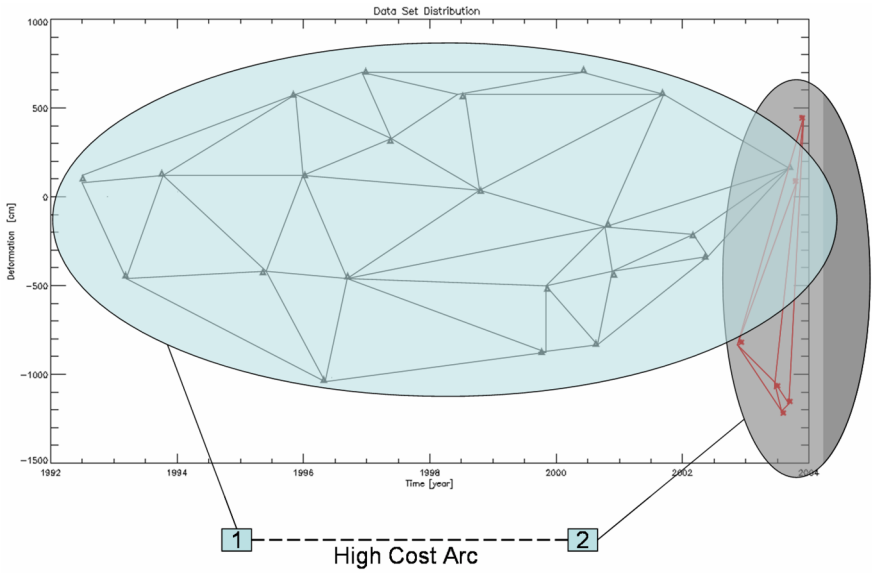

Figure 5. 8 A pictorially example of a network to be solved within the E-MCF algorithm to reconstruct the unwrapped phase difference vector associated to a selected spatial arc, in the case where two different subsets (as happens if the data acquired by two different radar sensors must be combined) are present. In particular, the example refers to the ERS/ENVISAT data combination of the Napoli Bay area. In circumstances like these, the algorithm requires that for each subset a proper reference node has to be introduced (labeled (1) and (2)), where the arcs connecting the novel nodes have to be characterized by an extremely large cost, in order to avoid that flows relevant to each sub-triangulation could interfere with those associated to other sub-triangulations.

investigated area are quite stable, the center of it is characterized by a significantly change on the deformation rate that appears to be essentially vertical.

5.3 Extension of the E-MCF approach to multi-platform (multi-subset) data-set

In this section, we will deal on the presentation of the results achieved by applying the E-MCF algorithm to a SAR data set composed by more than one independent subset, as happens for example if we are interested to combine the data acquired by two different radar sensor (see chapter two)

and/or in the case where the perpendicular/temporal baseline separation between a set of data is big enough (see chapter two).

Basically, in these cases, the basic Delaunay triangulation involved in the application of the E-MCF algorithm will be decomposed in more than one different sub-triangulations. The modifications to be applied to the algorithm, with respect to the case where a single triangulation is present, concern the introduction (see chapter three) of additional reference nodes (whose number is equal to the number of subset that are present) and the introduction of additional network arcs connecting the so-introduced "reference nodes" (as pictorially shown in Figure 5.7 with reference to the Napoli test site area). In such a way, the equivalent-temporal network to be solved (for each spatial arcs) will be composed in several sub-networks (whose number is equal to the subsets number).

If we want to follow the strategy explained within the chapter three, we will have to be able to solve, for each arc of the spatial Delaunay triangulation, the equivalent network, now composed by several different sub-networks, thus also guaranteeing that each sub-network is completely separated from the other ones. This task can be easily accomplished by requiring that the arcs connecting the "reference nodes" one another have an extremely high cost, thus implicitly preventing that each sub-network flow could address other sub-networks (see Figure 5.8). Once these assumptions have been assumed, the proposed algorithm can be effectively used also in these cases.

Moreover, also in these circumstances, other interferometric pairs can be subsequently added (and properly unwrapped following the strategy discussed in Section 5.1).

In order to demonstrate the capability of the proposed phase unwrapping technique, in conjunction to the application of the SBAS algorithm inversion, to investigate the deformation of the Campi Flegrei caldera and of the Vesuvius volcano, we have re-processed the same data-set we considered within the chapter for, which was composed by 63 ERS1/2 SAR acquisitions and 12 ASAR images, relevant to descending (track 36, frame 2781) orbits. Each interferometric SAR image pair has been chosen by applying the strategy discussed within the chapter three, by also imposing that the interferometric perpendicular baselines were smaller than 300m and the maximum time interval had been of approximately for years. Precise satellite orbital information and a DEM relevant to the Shuttle Radar Topography (SRTM) have been also used. Moreover, all the DInSAR products have been obtained following a complex multilook operation with for looks in the range direction and twenty looks in the azimuth one, with a resulting pixel spacing of about 100 x 100m. The results achieved on this area has been presented in Figure 5.9, where the mean deformation velocity maps,

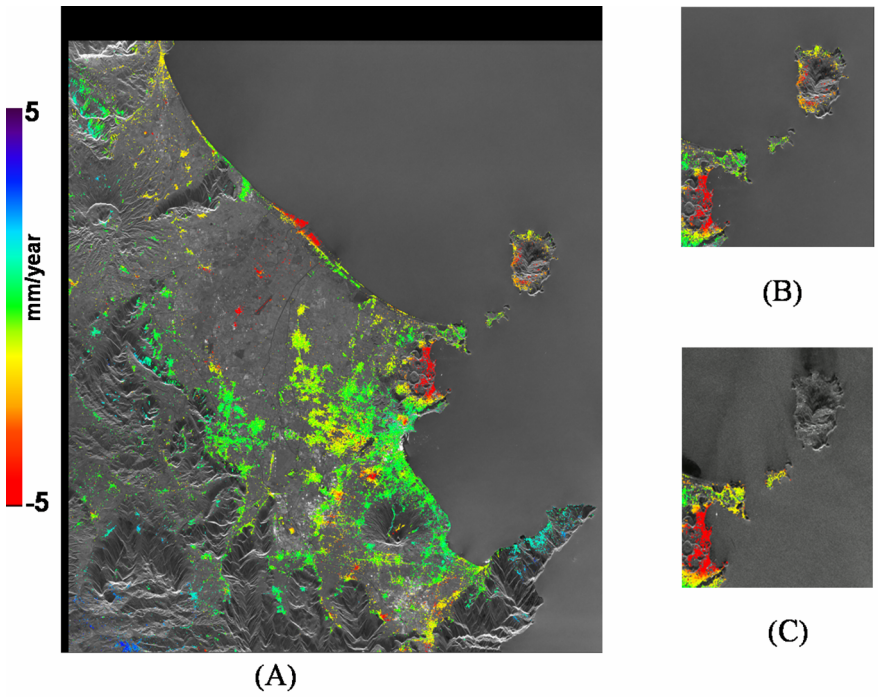

Figure 5. 9 Napoli Bay area interferometric products. (A) False color mean deformation velocity map of the illuminated area, superimposed to a multilook SAR image, obtained by applying the E-MCF phase unwrapping algorithm to a data-set composed both by ERS and ENVISAT SAR acquisitions. (B) The Ischia island portion of the velocity map and (C) the equivalent product obtained in application to the original MCF approach.

computed in the line of sight direction from the descending orbit, are shown. We can observe that, with respect to the case where the original MCF is applied (see Figure 5.9b), the application of the extended version of the MCF algorithm allows us to measure the deformation affecting the Ischia Island, located in the upper part of the mentioned figure, even if the chosen spatial reference node is located near the Napoli harbor.

5.4 Conclusion and further developments

In this chapter, some experimental products, carried out by using real SAR data-set, have been presented. These experiments have allowed us to investigate the potentiality and the limits of the proposed E-MCF phase unwrapping algorithm. In particular, we have investigated the possibility to

use additional differential interferograms to improve the stability and/or the correctness of our reconstructions; we observed this step represents a very crucial step to be well-accomplished, especially if the number of the additional interferograms is large enough. After that, we addressed the application of the proposed techniques in cases of particular interest (i.e., when the investigated area is affected by significantly fast deformation trends and/or when more than one subset is present or, in a more generalized way, when differential interferograms obtained with different operational modes are combined).

Note that, in particular, that the combination of multi-mode interferograms can be viewed as the natural development of the multi-sensor data integration and can be viewed as one of the possible improvement of the presented approaches.

Finally, the increase on the temporal coherence factor that this approach guarantees allows applying these techniques to also investigate the deformation temporal evolution relevant to large areas on the ground, as well as concerns the processing of whole multi-track interferometric SAR data. Therefore, the classical phase unwrapping approaches, which only exploits spatial constraints are characterized, as the distance from the reference point increase, by a gradually decrease of the correctness of the achieved solution, thus justifying the temporal coherence decrease. This circumstance, with reference to a multi-track case, would automatically impose that several and independent reference points should be selected, thus obtaining different solutions to be finally integrated. On the contrary, the possibility to improve the quality of our reconstruction, via the application of the proposed, spatial/temporal phase unwrapping algorithm, will allow processing the whole illuminated area.

Mission	Orbit	Day	Month	Year	$B_\perp$
ERS1	20701	30	6	1995	795,94
ERS1	22204	13	10	1995	-412,37
ERS2	4034	27	1	1996	-275,89
ERS1	24709	5	4	1996	-279,18
ERS2	5036	6	4	1996	-163,91
ERS2	7040	24	8	1996	191,84
ERS2	10046	22	3	1997	341,54
ERS2	11048	31	5	1997	146,51
ERS2	11549	5	7	1997	210,38
ERS2	12050	9	8	1997	370,93
ERS2	13052	18	10	1997	0,00
ERS2	13553	22	11	1997	299,04
ERS2	15557	11	4	1998	576,97
ERS2	16058	16	5	1998	399,30
ERS2	17060	25	7	1998	-286,06
ERS2	21068	1	5	1999	265,20
ERS2	22571	14	8	1999	-226,93
ERS2	23072	18	9	1999	-479,20
ERS2	24074	27	11	1999	864,81
ERS2	25076	5	2	2000	-606,22
ERS2	26078	15	4	2000	756,21
ERS2	27080	24	6	2000	-10,06
ERS2	28082	2	9	2000	-576,42
ERS2	29084	11	11	2000	686,25

(A)

Mission	Orbit	Day	Month	Year	$B_\perp$
ERS1	4003	21	4	1992	551,40
ERS1	4504	26	5	1992	-608,17
ERS1	7009	17	11	1992	-305,87
ERS1	8011	26	1	1993	-205,87
ERS1	9013	6	4	1993	663,10
ERS1	10015	15	6	1993	-328,78
ERS1	10516	20	7	1993	-298,11
ERS1	12019	2	11	1993	568,92
ERS1	19377	30	3	1995	-809,68
ERS1	20379	8	6	1995	-61,45
ERS2	1708	18	8	1995	102,16
ERS1	21882	21	9	1995	-249,26
ERS1	22383	26	10	1995	798,52
ERS2	2710	27	10	1995	868,99
ERS1	23385	4	1	1996	236,54
ERS2	4714	15	3	1996	309,57
ERS1	24888	18	4	1996	530,00
ERS2	5215	19	4	1996	440,16
ERS1	25389	23	5	1996	4,35
ERS2	6217	28	6	1996	66,24
ERS2	6718	2	8	1996	147,88
ERS2	7720	11	10	1996	-293,77
ERS2	8722	20	12	1996	-374,35
ERS2	9724	28	2	1997	0,00
ERS2	11728	18	7	1997	-83,97
ERS2	12229	22	8	1997	335,51
ERS2	12730	26	9	1997	-31,44
ERS2	13231	31	10	1997	-799,86
ERS2	13732	5	12	1997	242,56
ERS2	14233	9	1	1998	-144,71
ERS2	15235	20	3	1998	78,13
ERS2	16237	29	5	1998	35,08
ERS2	16738	3	7	1998	-594,99
ERS2	17239	7	8	1998	42,38
ERS2	18241	16	10	1998	-216,58
ERS2	19243	25	12	1998	-221,09
ERS2	20746	9	4	1999	522,59
ERS2	21748	18	6	1999	-241,11
ERS2	22249	23	7	1999	611,57
ERS2	23251	1	10	1999	371,04
ERS2	23752	5	11	1999	-241,53
ERS2	24754	14	1	2000	-785,46
ERS2	25255	18	2	2000	-413,33
ERS2	26758	2	6	2000	-96,03
ERS2	27760	11	8	2000	445,25
ERS2	28762	20	10	2000	92,43
ERS2	29263	24	11	2000	823,10
ERS2	29764	29	12	2000	-382,49

(B)

Table 5. 1 Umbria area SAR images acquired from ascending (A) and descending (B) orbits, respectively.

References

[1] C. A. Wiley: “Pulsed Doppler radar methods and apparatus”, U.S. Patent 3,196,436, filed in 1954;

[2] S. H. Pravdo, et al: "Seasat Synthetic Aperture Radar Data User's Manual," JPL publication 82-90, March 1, 1983;

[3] H. A. Zebker and R. M. Goldstein: “Topographic mapping from synthetic aperture radar observations”, J. Geophys. Res., 91, 4993, 1986;

[4] K. Gabriel, R. M. Goldstein and H. A. Zebker: “Mapping small elevation changes over large areas: Differential interferometry”, J. Geophys. Res., 94, 1989;

[5] J. W. Moore, "OSTA-1: The Space Shuttle's first scientific payload," Proceedings of 33rd IAF/IAC Congress, Paris, France, Sept. 27-Oct. 2, 1982;

[6] Pettengill, H. Gordon; Ford, G. Peter; Johnson, T. K. William; R. Raney, Keith, Soderblom, A. Laurence: “Radar performance and data products”, Science, vol. 252, April 12, 1991, p. 260-265;

[7] Special Issue on SIR-C/X-SAR, IEEE Transactions on Geoscience and Remote Sensing, Vol. 33, No. 4, July 1995;

[8] European Space Agency: “ERS SAR RAW: ERS-1/2 synthetic aperture radar (SAR) annotated raw product data”, http://earth1.esrin.esa.it:81/, 1998. Earthnet online;

[9] R. L. Jordan, E. R. Caro, Y. Kim, M. Kobrik, Y. Shen, F. V. Stuhr and M. U. Werner: “Shuttle radar topography mapper (SRTM) Microwave Sensing and Synthetic Aperture Radar”, Proc. SPIE, pp 412-422;

[10] H. Yoshihisa and O. Makoto: “Analysis of JERS-1 SAR imagery”, in International Geoscience and Remote Sensing Symposium, Tokyo, Japan, 18-21 August 1993, pages 1191-1193, 1993;

[11] http://envisat.esa.int/instruments/asar ;

[12] M. Shimada, A. Rosenqvist, M. Watanabe, T. Tadono: “Polarimetric and interferometric potential of the PALSAR/ALOS”, in Proc. POLinSAR, 2005;

[13] J. Closa, B. Rosich, A. Monti-Guarniery, “The ASAR Wide Swath Mode products”, in Proc. IGARSS 2003;

[14] G. Franceschetti and R. Lanari: “Synthetic Aperture Radar Processing”, CRC PRESS, New York, 1999;

[15] G. Franceschetti, R. Lanari and E. S. Marzouk: “Efficient and high precision space-variant processing of SAR data”, IEEE Trans. Aerosp. Electron. Syst., 31, 227, 1995;

[16] J. C. Curlander and R. McDonough: “Synthetic Aperture Radar – System and Signal Processing”, New York, Wiley;

[17] C. Elachi, “Spaceborne radar remote sensing: applications and techniques”, Institute of Electrical and Electronics Engineers, 1998;

[18] F. Ulaby, R. Moore and A. Fung: “Microwave remote sensing: active and passive, Vol.2:Radar remote sensing and surface scattering and mission theory”, Addison-Wesley, 1982;

[19] L. C. Graham: “Synthetic interferometer radar for topographic mapping”, Proc. IEEE, 62, 763, 1974;

[20] R. Bamler and P. Hartl: “Synthetic Aperture Radar interferometry”, Inverse Problems 14 (1998), R1-R54;

[21] Zebker and Villasenor, J. (1992): “Decorrelation in interferometric radar echoes”, IEEE Trans., 30, 950-959;

[22] Just D. and R. Balmer: “Phase statistics of interferograms with applications to synthetic aperture radar”, Appl. Optics, 33(20), 4361-4368, 1994;

[23] Lee, J. S. K. W. Hopple, S. A. Mango and R. Miller: “Intensity and Phase Statistics of Multilook Polarimetric Interferometric SAR Imagery”, IEEE Trans. On Geoscience and Remote Sensing., 32(5), 1017-1028,1994;

[24] R J A Tough, D. Blacknell and S. Quegan: “A statistical description of polarimetric and interferometric synthetic aperture radar”, Proceeedings of the Royal Society London A, 449:567-589, 1995;

[25] Ian R Joughin, Dale P WineBrenner and Donald B Percival: “Probability density functions for multilook polarimetric signatures”, IEEE Transactions on Geoscience and Remote Sensing, 32(3):562-574, May 1994;

[26] R. Bamler and D. Just: “Phase statistics and decorrelation in SAR interferograms”, in International Geoscience and Remote Sensing Symposium, Tokyo, Japan, 18-21 August 1993, pages 980-984, 1993;

[27] K. Sarabandi: ”Δk-radar equivalent of interferometric SAR's: a theoretical study for determination of vegetation height”, Trans. On Geoscience and Remote Sensing, vol. 35, n° 5, September 1997;

[28] F. Gatelli, A. M. Guarnieri, F. Parizzi, Pasquali P., C. Prati and F. Rocca: “The wavenumber shift in SAR interferometry”, Journal of Geophysical Research 94, B7 (july-10 1989), 9183-9191;

[29] D. Massonnet, M. Rossi, C. Carmona, F. Ardagna, G. Peltzer, K. Feigl and T. Rabaute; "The displacement field of the Landers earthquake mapped by radar interferometry", Nature, 364, 138-142, 1993;

[30] K. Gabriel, R. M. Goldstein and H. A. Zebker: “Mapping small elevation changes over large areas: Differential interferometry”, J. Geophys. Res., 94, 1989;

[31] N. Bleistein and R. A. Handelsman: “Asymptotic Expansion of Integrals”, Dover Pubblications, New York, 1986;

[32] G. Peltzer and P. A. Rosen: “Surface displacement of the 17 Eureka valley, California, earthquake observed by SAR interferometry”, Science, 268, pp. 1333-1336, 1995;

[33] E. Rignot: “Fast recession of a west Antarctic glacier”, Science, 281, pp. 549-551, 1998;

[34] M. Crosetto, B. Crippa, E. Biescas: “Early detection and in-depth analysis of deformation phenomena by radar interferometry”, Engineering Geology, 79(1-2), pp.81-91, 2005;

[35] A. Ferretti, C. Prati, F. Roccca: “Permanent scatterers in SAR interferometry”, IEEE Trans. On geoscience and remote sens., 38, 5 (2000), 2202-2212;

[36] R. Lanari, O. Mora, M. Manunta, J. J. Mallorqui, P. Berardino, E. Sansosti: “A Small Vaseline Approach for Investigating Deformations on Full Resolution Differential SAR Interferograms”, IEEE TRransaction on Geoscience and Remote Sensing, 42, 7, 2004;

[37] O. Mora, J. J. Mallorqui, Broquetas: “Linear and non linear terrain deformation maps from a reduced set of interferometric SAR images”, IEEE 41, pp. 2243-2253,2003;

[38] S. Usai: “A Least Squares Database Approach for SAR interferometric Data”, Transaction on Geoscience and Remote Sensing, 41, 4 pp. 753-760, 2003;

[39] P. Berardino, G. Fornaro, R. Lanari and E. Sansosti: “A new Algorithm for Surface Deformation Monitoring based on Small Baseline

Differential SAR Interferograms", IEEE Trans. Geosci. Remote Sens., 40, 11, 2002;

[40] R. Scharoo, P. Visser: "Precise orbit determination and gravity field improvement for the ERS satellites", Journal of Geophysical Research 103, C4 (1998), 8113-8127;

[41] N. Miranda, B. Rosich, C. Santella, and M. Grion: "Review of the impact of ERS-2 piloting modes on the SAR Doppler stability", in Proc. Fringe,Frascati, Italy, Dec. 2003, CD-ROM;

[42] C. Y. Chang and John C. Curlander: "Application of the Multiple PRF Technique to Resolve Doppler Centroid Estimation Ambiguity for Spaceborne SAR". IEEE Transactions on Geoscience and Remote Sensing, 30(5):941-949, Sept 1992;

[43] Soren, N. Madsen: "Estimating the Doppler Centroid of SAR Data", IEEE Transactions on Aerospace and Electronic Systems, 25(2):134-140, 1989.

[44] R. Hanssen: "Radar Interferometry", Kluwer Academic Publishers, 2001;

[45] R. M. Goldstein: "Atmospheric limitations to repeat-track radar interferometry", Geophysical Research Letter, 22, pp.2517-2520,1995;

[46] G. Fornaro and G. Franceschetti: "Image registration in Interferometric SAR Processing", IEE Proc.-Radar, Sonar, Navig., 142, 1995;

[47] E. Sansosti, P. Berardino, M. Manunta, F. Serafino and G. Fornaro: " Geometrical SAR Image Registration" in Geoscience and Remote Sensing, IEEE Transactions, Volume 44, Issue: 10, Part 2, pp 2861- 2870, 2006;

[48] P. A. Rosen, S. Hensley, E. Gurrola, F. Rogez, S. Chan and J. Martin: "SRTM C-band topographic data quality assessment and calibration activities", Proc. of IGARSS'01, 739-741, 2001;

[49] R. M. Goldstein and C. Werner: "Radar interferogram filtering for geophysical application", Geophysical Research Letters, vol. 25, pag. 4035-4038, 1998;

[50] W. H. Flannery, S. A. Teukolsky and W. T. Vetterling: "Singular Value Decomposition ", in Numerical recipes in C, Cambridge: Cambridge University Press, pp. 60-72, 1988;

[51] R. M. Goldstein, H. A. Zebker and C. L. Werner: "Satellite radar interferometry: two-dimensional phase unwrapping", Radio Sci., 23, 1988;

[52] D. C. Ghiglia and L. A. Romero: “Robust two-dimensional weighted and unweighted phase unwrapping that uses fast transform and iterative methods”, J. Opt. Soc. Am. A, 11, 1994;

[53] G. Fornaro, G. Franceschetti and R. Lanari: “Interferometric SAR Phase Unwrapping Using Green’s Formulation”, IEEE Trans. Geosci. Remote Sens., 34, 1996;

[54] D. C. Ghiglia and M. D. Pritt: “Two-Dimensional Phase Unwrapping: Theory, Algorithms and Software”, John Wiley and Sons New York, 1998;

[55] M. Costantini: “A novel phase unwrapping method based on network programming”, IEEE vol 36, 3 May 1998, pp 813-821;

[56] M. Costantini and P. Rosen: “A generalized phase unwrapping approach for sparse data”, In Proc. Int Geoscience and Remote Sensing Symposium (igarrs99), Hamburg, Germany, 28 June – 2 July 1999;

[57] G. Davidson and R. Bamler: “Multiresolution phase unwrapping for SAR interferometry”, IEEE vol 37., 1 (Jan 1999), 163-174;

[58] G. Schreirer: “SAR Geocoding-Data System“, Karlsruhe, Wichmann,1993;

[59] E. Sansosti: “A simple and exact solution for the interferometric and stereo SAR geolocation problem”, IEEE Trans. On Geoscience and Remote Sensing, volume 42, 8, pp 1625-1634, August 2004;

[60] P. Lundgren, F. Casu, M. Manzo, A. Pepe, P. Berardino, R. Lanari: “Gravity and magma induced spreading of Mount Etna” Geophys. Res. Lett., 31, 2004;

[61] F. Casu, M. Manzo and R. Lanari: “A quantitative assessment of the SBAS algorithm performance for surface deformation retrieval from DInSAR data”, Remote Sensing of Environment Journal, 102, pp. 195-210; 2006;

[62] A. Avallone, A. Zollo, P., Briole, C. Delacourt and F. Beauducel: “ Subsidence of Campi Flegrei (Italy) detected by SAR interferometry”, Geophys. Research Letters 26, 15, 2303-2306,1999;

[63] In press, R. Lanari, F. Casu, M. Manzo, G. Zeni, P. Berardino, M. Manunta, A. Pepe: “An overview of the Small Baseline Subset Algorithm: a DInSAR Technique for Surface Deformation Analysis”, Pure And Applied Geophysics (Pageoph);

[64] Borgia A., P. Tizzani, G. Solaro, M. Manzo, C. Casu, G. Luongo, A. Pepe, P. Berardino, G. Fornaro, E. Sansoti, G. P. Ricciardi, N. Fusi, G. Di Donna and R.Lanari: “Volcanic Spreading of Vesuvius, a new paradigm for interpreting its volcanic activity”, Geosphys. Reaearch Letters, 32, 2005;

[65] R. Lanari, P. Berardino, S. Borgström, C. D. Gaudio, P. D. Martino, G. Fornaro, S. Guarino, G. P. Ricciardi, E. Sansosti and P. Lundgren: "The use of IFSAR and classical geodetic techniques for caldera unrest episodes: Application to the Campi Flegrei uplift event of 2000," J. Volcanol. Geothermal Res., vol. 133, pp. 247–260, May 2003;

[66] R. Lanari, P. Lundgren, M. Manzo, and F. Casu, "Satellite radar interferometry time series analysis of surface deformation for Los Angeles, California", Geophys. Res. Lett., 31, 2004;

[67] M. Manzo, G. P. Ricciardi, F. Casu, G. Ventura, G. Zeni, S. Borgström, P. Berardino, C. Del Gaudio, R. Lanari: "Surface deformation analysis in the Ischia island (Italy) based on spaceborne radar interferometry", Journal of Volcanology and Geothermal Research, 151, pp 399-416, 2005;

[68] H. A. Zebker and Y. Lu "Phase Unwrapping Algorithms for radar interferometry: residue-cut, least-squares, and synthesis algorithm J. Opt Soc. Am A. 15, 586-598, 1998;

[69] B. R. Hunt: "Matrix Formulation of the Reconstruction of Phase Values from Phase Differences", Journal of the Optical Society of America, 69., pp. 393-399, 1999;

[70] G. Fornaro, G. Franceschetti, R. Lanari, E. Sansosti: "Robust phase-unwrapping techniques: a comparison", J. Opt. Soc. Am A., 13, 2355,1996;

[71] H. Takajo and T. Takahashi: "Least-squares phase estimation from the phase difference", J. Opt. Soc. Am. A 5, 1988;

[72] M. D. Pritt: "Phase Unwrapping by means of multigrif techniques for interferometric SAR", IEEE Transaction Geoscience and Remote Sensing, 34(3) 728-738, 1996;

[73] M. Costantini, F. Malvarosa, F. Minati, L. Pietranera, and G. Milillo, "A three-dimensional phase unwrapping algorithm for processing of multitemporal SAR interferometric measurements," in Proc. IGARSS, Toronto, ON, Canada, Jun. 2002, pp. 1741–1743;

[74] A. Pepe and R. Lanari, "A space-time minimum cost flow phase unwrapping algorithm for the generation of DInSAR deformation time-series," in Proc. IGARSS, Seoul, Korea, Jul. 2005, pp. 1979–1982;

[75] A. Ferretti, C. Prati and F. Rocca: "Non-linear Subsidence Rate Estimation Using Permanent Scatterers in Differential SAR Interferometry", IEEE Transaction on Geoscience and Remote Sensing, 38, 5., 2002;

[76] M. Arrigoni, C. Colesanti, A. Ferretti, D. Perissin, C. Prati, and F. Rocca: "Identification of the location phase screen of ERS-ENVISAT permanent scatterers", Fringe 2003 Conf., Frascati, Italy, Dec. 2003;

[77] R. Lanari, G. D. Natale, P. Berardino, E. Sansosti, G. P. Ricciardi, S.Borgstrom, P. Capuano, F. Pingue, and C. Troise; "Evidence for a peculiar style of ground deformation inferred at Vesuvius volcano," Geophys. Res. Lett., vol. 29, 2002;

[78] R. Lanari, G. Zeni, M. Manunta, S. Guarino, P. Berardino, and E. Sansosti: "An integrated SAR/GIS approach for investigating urban deformation phenomena: The city of Napoli (Italy) case study," Int. J. Remote Sens., vol. 25, pp. 2855–2862, July 2004;

[79] R. Lanari, O. Mora, M. Manunta, J. J. Mallorqui, P. Berardino, and E. Sansosti: "A small baseline approach for investigating deformations on full resolution differential sar interferograms," IEEE Trans. Geosci. Remote Sens., vol. 42, no. 7, pp. 1377–1386, Jul. 2004;

[80] A. Pepe and R. Lanari: "On the extension of the Minimum Cost Flow Algorithm for Phase Unwrapping of Multi-temporal Differential SAR Interferograms" IEEE Transactions on Geoscience and Remote Sensing, vol 44, 9, September 2006;

[81] P. Tosi, A. Tertulliani, V. De Rubeis and C. Gasparini: "Preliminary results of a macroseismic survey of the Colfiorito sequence (Central Italy)", Phys. Chem. of the Earth, 24, 6, 477-481, 1999;

[82] M. Manunta, G. Zeni, E. Sansosti, R. Lanari, F. Ardizzone, M. Cardinali, M. Galli, F. Guzzetti and P. Reichenbach: "Ground deformation analysis in the Umbria region (central Italy) carried out via the SBAS DinSAR approach", Geophysical Research Abstract. Vol. 8, 10026, 2006 - EGU 2006, Vienna, Austria, 02– 07 April 2006.

Acknowledgments

I wish to thank people who helped me during the doctoral studies period.
In particular, I am grateful to my tutor Prof. Ovidio M. Bucci for his support and to my colleagues from IREA-CNR of Naples.
Furthermore, my best thanks go to Riccardo Lanari from IREA-CNR who has encouraged and supported me during last five years.